Numerical analysis of the hemodynamic response to orthostatic stress

J.M.T. Keijsers

ISBN: yyy-yy-yyy-yyyy-y

The research described in this thesis was funded by a scholarship from the Helmholtz SpaceLife Sciences Research School (SpaceLife) which was funded by the Helmholtz Association and he German Aerospace Center (Deutsches Zentrum für Luft und Raumfahrt e.V., DLR).

Numerical analysis of the hemodynamic response to orthostatic stress

PROEFSCHRIFT

ter verkrijging van de graad van doctor aan de
Technische Universiteit Eindhoven, op gezag van de
rector magnificus prof.dr.ir. F.P.T. Baaijens, voor een
commissie aangewezen door het College voor
Promoties in het openbaar te verdedigen
op maandag 16 januari 2017 om 16.00 uur

door

Johanna Maria Theodora Keijsers
geboren te Roermond

Dit proefschrift is goedgekeurd door de promotoren en de samenstelling van de promotiecommissie is als volgt:

voorzitter:	prof.dr. P.A.J. Hilbers
1e promotor:	prof.dr.ir. F.N. van de Vosse
copromotoren:	dr.ir. C.A.D. Leguy (Deutsches Zentrum für Luft und Raumfahrt, Köln)
	dr.ir. W. Huberts (Universiteit Maastricht)
leden:	prof.dr. C.V.C. Bouten
	prof.dr.ir. E.J.E. Cottaar
	prof.dr. J. Rittweger (Universität zu Köln)
	assoz.-prof. priv.-doz. dr.med. N. Goswami, PhD (Medizinische Universität Graz)

Het onderzoek dat in dit proefschrift wordt bechreven is uitgevoerd in overeenstemming met de TU/e Gedragscode Wetenschapsbeoefening.

Contents

Abstract

The main function of the cardiovascular system is to transport blood to the tissue and thereby provide it with sufficient oxygen. The total blood flow and its distribution over the circulation can be regulated in response to a change in oxygen demand or to external stress factors. Orthostatic stress, i.e. gravitational stress in the upright position, induces a blood volume shift from the head towards the feet. This results in decreased cerebral perfusion, which increases oxidative stress, and increased transmural pressure in the lower extremity. To minimize these stresses a complex system of protection mechanisms is activated, which includes amongst others: (1) the presence of venous valves, ensuring unidirectional flow, (2) the muscle pump effect, which squeezes the embedded deep veins upon calf muscle contraction, and (3) the baroreflex, aiming to maintain systemic pressure by regulating heart rate, contractility and peripheral resistance. Many experimental studies confirmed the importance of the above mentioned mechanisms in compensating for the gravity-induced blood volume shift in the upright position. However, a causal dependency and thereby full mechanistic insight in the physiology is often missing.

In the past, mathematical models based on physical laws and physiological mechanisms have proven to increase the understanding of the cardiovascular (patho-)physiology. Therefore, in the current thesis a numerical approach is presented to gain more insight in the mechanisms compensating for the gravity-induced blood volume shift towards the lower body.

In the current PhD project, mathematical models have been developed in order to examine three major mechanisms reducing the gravity-induced blood volume shift:

the muscle pump effect, venous valves and regulation of vascular tone. To reveal their individual importance the included number of mechanisms is increased step-by-step. First, to capture the dynamics involved with the muscle pump effect, an existing 1D arterial pulse wave propagation model is extended to include venous collapsibility, venous valves and gravitational stress. The simulations reveal the importance of the venous valves for increasing effective venous return as well as shielding the hydrostatic pressure. Furthermore, adding the superficial venous system results in a fastening of venous refilling. However, the small increase in simulated arterial flow after muscle contraction in comparison to *in vivo*, implies that the model does not yet contain all relevant mechanisms. Second, a global sensitivity analysis of the venous valve dynamics under head up tilt is performed to gain insight in the importance of the various model parameters and their interactions. From this, it is concluded that improved assessment of venous radius and pressure drop at valve opening can reduce model uncertainty. Third, inclusion of a regulation model accounting for the metabolic, myogenic and baroreflex regulation, results in good agreement between the simulated and *in vivo* flow response. From the regulatory activation it is concluded that the metabolic activation induces the flow increase after muscle contraction and that myogenic and baroreflex activation result in a decreased baseline flow in the tilted position.

Finally, a full circulation model is presented including a new micro-circulation element to account for the blood volume and its distribution. This model can serve as a backbone for future models in which all physiological mechanisms activated upon orthostatic stress are integrated. Such a model allows examination of the global response of local phenomena and their mutual interaction.

In summary, the developed models provide an important step towards full understanding of the hemodynamic response to orthostatic stress. Furthermore, they provide many opportunities for further research into the physiological mechanisms protecting the cardiovascular system against the gravity-induced stresses.

Chapter 1

General introduction

1.1 Introduction

The main function of the heart is to pump the blood through the vascular system in order to supply the tissue with sufficient oxygen. The blood supply to the various tissues can be adapted upon a change in oxygen demand and in response to external stresses. Orthostatic stress, i.e. gravitational stress in the upright position, induces a blood volume shift from the head towards the feet. Without a proper regulatory response this will reduce cerebral perfusion and might even result in critical events, such as syncope. Mechanisms to minimize the blood volume shift are amongst others (1) the presence of venous valves, which insure unidirectional flow towards the heart, (2) calf muscle contraction, which increases venous return by squeezing the embedded veins, and (3) the baroreflex, which aims to maintain arterial pressure by adapting heart rate, heart contractility and vascular resistance. Many studies have tried to unravel the physiology of the mechanisms, which minimize blood volume shifts under orthostatic stress. However, what is still lacking is mechanistic insight. Mathematical models based on physical laws and physiological mechanisms have proven useful in understanding cardiovascular physiology. Therefore, the aim of this thesis is to develop a mathematical model to advance mechanistic understanding of the hemodynamic response to orthostatic stress.

This chapter briefly describes the cardiovascular system, its response to orthostatic stress, and the mechanisms, which fail in patients unable to withstand prolonged orthostatic stress. Subsequently, a short overview of experimental and numerical studies investigating the cardiovascular system and in particular the response to orthostatic stress is provided. This chapter concludes with the specific aims and outline of the thesis.

1.2 The cardiovascular system

The main function of the cardiovascular system is the delivery of oxygen to the organs. Therefore, it consists of two networks of vessels: the pulmonary circulation, which oxygenates the blood in the lungs, and the systemic circulation, which delivers the oxygen to the organs throughout the body. Both circulations are connected to each other by a pump: the heart. The heart is a muscular organ, which consists of four cavities: two atria, which collect the blood from one circulation, and two ventricles, which pump the blood into the other circulation. The left atrium receives the blood from the pulmonary circulation and is connected to the left ventricle by the mitral valve. Through the aortic valve the left ventricle pumps the blood into the systemic circulation. Blood from the systemic circulation returns to the heart in the right atrium, where it is pumped through the tricuspid valve into the right ventricle.

The right ventricle pumps it again back into the pulmonary circulation. Although both circulations have a different function, they consist of the same types of vessels: arteries, arterioles, capillaries, venules and veins. The ventricles pump the blood into the arteries, which have an elastic wall to withstand the high transmural pressures. While approaching the organs, the arteries branch many times to become arterioles. Due to the presence of smooth muscle cells in the arteriolar wall, blood flow and its distribution over the various organs can be regulated at this level of the circulation. At the level of the organs, arterioles bifurcate into capillaries. The vessel wall of capillaries consists of a single layer of endothelial cells on a basal membrane. The thin capillary wall and the strong level of branching enables a fast exchange of oxygen and other nutrients. The small diameter of the capillaries creates a large pressure drop over the micro-circulation and results in a low pressure in the venules. Due to their large compliance and capacity, the venules play a large role in volume distribution. Finally, the blood is collected in the larger veins and transported back to the heart. Venous valves are present in these vessels to ensure unidirectional flow.

1.3 Cardiovascular regulation under orthostatic stress

Sufficient oxygen delivery is vital for all tissue in the human body and therefore it is essential that the cardiovascular system can regulate blood flow upon a change in oxygen demand or in response to external stress factors. An important factor that triggers the cardiovascular regulation every day is gravity. Gravity gives weight to mass and in fluids this results in an increase in hydrostatic pressure due to the weight of the fluid column present above, as for example observed during scuba diving. Similarly in the upright position, hydrostatic pressure will increase below the level of the heart inducing the arteries and veins to dilate. In contrast, the cross-section of the vessels present above the heart level will reduce due to the decrease in hydrostatic pressure towards the head. Consequently, in the upright position gravity will induce a blood volume shift from the head towards the feet. The gravitational stress in the upright position is called orthostatic stress.

To minimize the fluid shift due to orthostatic stress, the cardiovascular system has several compensating characteristics and mechanisms. Firstly, the vessel stiffness increases with increasing distance from the heart, meaning the dilation will be less under the same pressure change. Furthermore, the compliant venous system contains venous valves. This not only ensures unidirectional flow, but can transiently decrease distal venous pressure when it shields the vein distal to the valve from the hydrostatic column present above. A mechanism that actively reduces the gravity-induced blood volume shift is the muscle pump effect. Considering the calf muscles, a muscle contraction will collapse the embedded deep veins, which will increase ve-

nous return. During the subsequent muscle relaxation venous refilling will increase muscle blood flow, aided by the increased perfusion pressure due to the pressure shielding of the venous valves. Another regulation mechanism, which reduces blood volume shifts is the baroreflex. Using stretch sensors in the vessel wall of the aortic arch and the carotid artery, this mechanism senses a change in arterial pressure. By adapting heart rate, heart contractility, peripheral resistance and venous unstressed volume, the baroreflex aims to keep the arterial blood pressure at the same level.

1.4 Orthostatic intolerance

If cardiovascular regulation is not sufficient, an upright position may result in reduced cerebral perfusion, causing dizziness or even critical events, such as syncope. This pathology is called orthostatic intolerance and is observed in astronauts after space-flight, in patients with spinal cord injury and is associated with aging. Orthostatic intolerance is observed in about 25% of returning astronauts due to the adaptation of their cardiovascular system to the micro-gravity environment (Williams et al., 2009). An important adaptation is the reduction of the total blood volume due to increased renal secretion. In space, renal secretion increases in response to the increased pressure in the upper body, due to the fluid shift from the legs towards the head in the micro-gravity environment (Buckey et al., 1996). This fluid shift occurs, because gravity is not pulling the blood towards the legs anymore. Back on earth, the reduced blood volume results in decreased venous return, which is even further decreased by the impaired muscle pump. The latter is a result of decreased muscle mass, due to decreased muscle activity. Furthermore, impaired baroreflex function is another factor decreasing the orthostatic tolerance (Fritsch et al., 1992). The mechanisms of orthostatic intolerance in patients with spinal cord injury show similarities to those observed in astronauts (Scott et al., 2011). Firstly, an altered salt and water balance results in a reduced total blood volume. Due to a lack of muscle activity venous return will not increase and cardiac output will be reduced (Claydon et al., 2006). Although parasympathetic control is mostly unaffected, the dysfunction of the sympathetic nervous system results in a decreased vasoconstrictive response (Claydon et al., 2006). Prevalence of orthostatic intolerance increases with successive age (Rutan et al., 1992). This can be due to several factors including supine hypertension, age-related changes in baroreflex function, increased vessel stiffness, but also decreased blood volume and chronic venous disease leading to decreased muscle pump efficiency (Freeman et al., 2011).

1.5 Experimental studies

To investigate orthostatic intolerance and the mechanisms which act to tolerate gravity, several types of experiments can be performed.

One of the simplest examples, which has provided a lot of insight, is the head up tilt (HUT) test. During HUT the subject is positioned supine on a tilt table which can be rotated, either mechanically or electrically, to a certain angle. Because the subject is tilted passively the muscle pump effect is assumed to be negligible during this procedure. The tilt angle defines the amount of gravitational acceleration applied by $a = g \sin \alpha$ (with g the gravitational acceleration and α the tilt angle) and is often limited to $70°$ ($a = 94\% g$) in order to minimize calf muscle contraction.

A second approach to study the hemodynamic response to blood volume shifts is lower body negative pressure (LBNP). In these experiments the lower extremity up to the iliac crest is positioned in a sarcophagus, in which pressure can be decreased (up to 50 mmHg) to induce a volume shift towards the lower extremity. Compared to a HUT test, LBNP avoids any vestibular response as subject position is constant and capillary filtration follows a different gradient because the hydrostatic pressure component is negligible. Furthermore, LBNP is also applied as a countermeasure in space to simulate blood volume shifts in the upright position on earth.

To investigate the limits of orthostatic tolerance a human centrifuge can be used (Clément and Pavy-Le Traon, 2004). The centrifugal acceleration applied to the subject depends on the rotational speed ω and the radius r via $a = \omega^2 r$. Therefore, when positioned in a short-arm ($r \approx 3$ m) centrifuge a gradient of gravitational load is applied to the subject, whereas an approximately uniform load is applied in a long-arm centrifuge ($r \approx 15$ m).

Specifically focussing on astronauts, their deconditioning can be mimicked in a bed rest study. During a bed rest study a subject remains in the supine position for a period varying from several hours up to two months. In order to induce the headward fluid shift as observed in astronauts in space, the bed is place in a $6°$ head down tilt position. To investigate changes in orthostatic tolerance caused by the deconditioning, experiments like head up tilt or LBNP are performed at several time points before and after the bed rest.

These experiments all commonly monitor hemodynamic parameters such as heart rate, mean arterial blood pressure, peripheral resistance and blood flow are. Furthermore, venous valve dynamics can be assessed using ultrasound.

1.6 Numerical studies

Many experimental studies have aimed to examine cardiovascular physiology under orthostatic stress. Although many questions have been answered, a detailed understanding of the mechanisms and their interaction is still lacking. Another approach to investigate the hemodynamic response to orthostatic stress is the use of mathematical models based on physical laws and physiological mechanisms. Because these models are built on current knowledge of the cardiovascular physiology, they allow us to challenge current hypotheses. The fact that physiological mechanisms and parameters can easily be individually changed, provides more detailed insight than experimental studies. One can, for example distinguish the influence of various regulation mechanisms by turning them on and off individually. On the other hand, combining experimental and numerical studies can be beneficial for both, because experimental studies can provide certain model parameters and mathematical models can be used to test experimental hypotheses. Finally, in contrast to numerical studies, experimental studies include the investigation of subjects, who are often patients suffering from multiple diseases. This can make it hard to distinguish between effects of the disease under investigation and effects of other diseases.

Mathematical models with different levels of detail can be used to describe the hemodynamics of the cardiovascular system. Two and three-dimensional models are often used to simulate the hemodynamics in complex geometries such as aneurism (Raghavan et al., 2000) and around heart valves (Sotiropoulos et al., 2016). The benefit of these models are that they can give detailed information on the local flow field or wall shear stress, but often have high computational cost and many unknown boundary conditions to be defined. Zero-dimensional models can give general predictions based on lumping the capacitive, inertive and resistive characteristics of a vessel or groups of vessels into a single element. One-dimensional pulse wave propagation models can predict pressure and flow wave propagation in large vessels based on the one-dimensional equations of mass conservation and momentum balance. Although these reduced order (i.e. 0D and 1D) models lack three-dimensional information, they provide a strong tool to model the full circulation with reduced computational costs. In the last decade, reduced order models have been used to increase the understanding of cardiovascular (patho-)physiology (Boileau et al., 2015; Shi et al., 2011; van de Vosse and Stergiopulos, 2011), and have been validated with *in vivo* data (Olufsen et al., 2006; Reymond et al., 2009) or even developed further for patient-specific modeling as a support for clinical decision making (Caroli et al., 2013; Marchandise et al., 2009).

Numerical studies focussing on the short-term (< 5 min) hemodynamic response to orthostatic stress are few and are mostly performed using lumped parameter models of the full circulation (Melchior et al., 1992; Sharp et al., 2013). Additional reg-

ulation models of the arterial and cardiopulmonary baroreflex are often added to regulate heart rate, contractility, peripheral resistance and venous unstressed volume. Heldt et al. (2002) validated their model with *in vivo* data of the heart rate, stroke volume and mean arterial pressure, while simulating both head up tilt and LBNP. Furthermore, a case study was presented on how the model could be used to simulate post-flight orthostatic intolerance in astronauts. Lim et al. (2013) developed a lumped parameter model to investigate the impact of cardiac failure on the hemodynamic response to head up tilt. Olufsen et al. (2005) developed a model to simulate the transition from sitting to standing while including both autonomic and cerebral auto-regulation. The simulated arterial blood pressure and cerebral flow were validated with *in vivo* measurements.

Whereas lumped parameter models are often used to study the baroreflex response under head up tilt, pulse wave propagation models are more appropriate for the investigation of the muscle pump effect. Furthermore, in contrast to 0D models, pulse wave propagation models enable implementation of a continuous gravitational stress in the momentum balance. Although a large number of studies present 1D pulse wave propagation models of arterial hemodynamics, venous hemodynamics and the influence of gravity are less frequently investigated with this type of model. The most important difference between the arterial and venous pulse wave propagation model is the constitutive law. Where the arterial wall can be approximated by a linear relation, the veins are prone to collapse under negative transmural pressure due to increasing extravascular pressure under muscle contraction or gravitational stress. To account for this non-linear pressure area relation, Shapiro (1977) derived a law for collapsible tubes. In the eighties, many analytical studies investigated the choking and supercritical flow in collapsible tubes (Cancelli and Pedley, 1985; McClurken et al., 1981). Furthermore, inclusion of the influence of axial and longitudinal tension (McClurken et al., 1981) and the shape of the collapsing cross-section was investigated (Flaherty et al., 1972; Kresch and Noordergraaf, 1972). Detailed numerical studies focussing on the venous hemodynamics are scarce and focuss mostly on numerical stability (Brook and Pedley, 2002; Brook et al., 1999) and aim to capture venous collapse (Fullana et al., 2003).

Veins can be idealised as collapsible tubes and their hemodynamic response can be modelled based on the work of Shapiro (1977). Although the main focus was to solve numerical instability problems, Marchandise and Flaud (2010) presented one of the first attempts to simulate the muscle pump effect. The main achievement was the simulation of the emptying of the vein. Whilst Marchandise and Flaud (2010) did not include any venous valves, Fullana and Zaleski (2008) developed a model of the lower extremity including valves to simulate the local pressure and flow response to a muscle contraction. The numerical studies of the venous 1D pulse wave propa-

gation discussed so far only include a small part of the circulation. Recently, the 1D pulse wave propagation models of the full circulation presented by Müller and Toro (2014) and Mynard and Smolich (2015) have received a lot of attention. Both include most of the large systemic veins using a 1D pulse wave propagation model. However, as their interest is the cerebral circulation and wave propagation respectively, they both did not include the effect of gravity.

To capture venous hemodynamics correctly, it is important to model the influence of the venous valves in preventing back-flow and providing pressure shielding. In reduced order models venous valves, if included at all, are often represented by a simple diode. But even studies which include some venous valves do not present the resulting changes in valve state during their simulations (Fullana and Zaleski, 2008; Müller and Toro, 2014). The simple diode representation only defines a fully open or closed state and does not allow investigation of the dynamics of the valves themselves. Considering heart valves, more detailed models exist: Korakianitis and Shi (2006) presented a heart valve model defining the valve opening state based on a force balance on the valve leaflets and Mynard et al. (2012) defined the valve opening state as a function of the pressure drop over the valve. A more detailed venous valve model, like that presented for heart valves, would allow studying of venous valve regurgitation (Mynard et al., 2012) and prolapse (Pant et al., 2015). This would be beneficial for the investigation of chronic venous disease.

A final important aspect when modeling the response to orthostatic stress, is the local regulation of vascular tone. Although this local regulation is based on the same mechanisms for each tissue, in numerical studies it is mostly applied to investigate cerebral auto-regulation (Olufsen et al., 2002; Spronck et al., 2012; Ursino, 1988). Simakov et al. (2013) applied an auto-regulation model to study the response to calf muscle contraction, but this model ignored the metabolic activation.

Once all the relevant physical and physiological processes are included within any model, it should be validated by comparing the simulated results with *in vivo* measurements. Furthermore, it is important to characterise model sensitivity, by knowing how the variance of the numerous model parameters affect the output variance. This can be achieved by means of a sensitivity analysis. Many studies perform a local sensitivity analysis, but a more thorough global approach is necessary if one wants to investigate the interaction between the model parameters as well. A gold standard method for a global sensitivity analysis is the Monte Carlo method (Saltelli et al., 2008), which includes many model evaluations to derive the output variance and how it can be attributed to the various input parameters. However, an increasing number of model evaluations is necessary once the number of input parameters increases. A sensitivity analysis is essential when developing mathematical models for support in clinical decision making, but these applications are not well suited

to high computational costs. Therefore, recent studies have applied faster methods for sensitivity analysis to cardiovascular mathematical models (Eck et al., 2016). An example is the polynomial chaos expansion method, which derives a metamodel to determine the output variance and allows direct analytical derivation of the influence of the input parameters (Huberts et al., 2014). This method is even further optimized by Donders et al. (2015), who introduced a two-step approach to reduce the number of analysed input parameters in the PCE. Furthermore, Quicken et al. (2016) applied the adaptive sparse polynomial chaos expansion to cardiovascular mathematical models, which adaptively builds the metamodel only including the significant interactions.

1.7 Aim and thesis outline

Many experimental studies have been performed to identify the causes of orthostatic intolerance and investigate the mechanisms involved in orthostatic tolerance for healthy individuals. Although this has increased insight into the underlying physiology, still many questions remain. In contrast, in the numerical field relatively few studies have included the influence of orthostatic stress. Whereas most of the existing models including gravity focuss on the baroreflex response under head up tilt, relatively few aim to investigate the muscle pump effect and the venous circulation. The existing venous models are therefore still in an early stage of development. Therefore,

the aim of this thesis is to develop a mathematical model to examine the hemodynamic response to orthostatic stress, while focussing on the venous system and the impact of the activation of the surrounding muscles

This thesis is outlined as follows. In Chapter 2 an existing arterial 1D pulse wave propagation model will be extended to account for gravity and venous collapse. The developed model will be applied to the local calf circulation to examine the muscle pump effect, while focussing on the influence of venous valves, hydrostatic pressure and the superficial venous system. Chapter 3 focusses on the dynamics of the venous valve. For this a venous valve model is implemented in a single calf vein and venous valve dynamics are examined under head up tilt. The importance of the variance in the model parameters on the variance in the valve dynamics is investigated using a sensitivity analysis. In Chapter 4, the local calf model presented in Chapter 2 is extended to include regulation of vascular tone, in order to examine the importance of the myogenic, metabolic and baroreflex regulation. Furthermore, the simulated flow response will be validated with an *in vivo* response to a muscle contraction. Finally, a sensitivity analysis will be performed to investigate the impact of the model parameters on the variance of the output. In Chapter 5 a 1D pulse wave

propagation model of the full circulation is presented including a new element for the micro-circulation. The latter accounts for the blood volume distribution over the whole body and thereby allows to examine the blood volume shift under orthostatic stress. The thesis is concluded with a general discussion of the presented results and recommendations are provided for further improvement of the developed models and possible future applications.

Chapter 2

Muscle Pump

This chapter is based on: A 1D pulse wave propagation model of the hemodynamics of calf muscle pump function, **J.M.T. Keijsers**, C.A.D. Leguy, W. Huberts, A.J. Narracott, J. Rittweger and F.N. Vosse, *International Journal of Numerical Methods in Biomedical Engineering* **31**(7):e02714, 2015.

ABSTRACT
The calf muscle pump is a mechanism which increases venous return and thereby compensates for the fluid shift towards the lower body during standing. During a muscle contraction the embedded deep veins collapse and venous return increases. In the subsequent relaxation phase, muscle perfusion increases due to increased perfusion pressure, as the proximal venous valves temporarily reduce the distal venous pressure (shielding). The superficial and deep veins are connected via perforators, which contain valves allowing flow in the superficial-to-deep direction. The aim of this study is to investigate and quantify the physiological mechanisms of the calf muscle pump, including the effect of venous valves, hydrostatic pressure and the superficial venous system. Using a one-dimensional pulse wave propagation model, a muscle contraction is simulated by increasing the extravascular pressure in the deep venous segments. The hemodynamics are studied in three different configurations: a single artery-vein configuration with and without valves and a more detailed configuration including a superficial vein. Proximal venous valves increase effective venous return by 53% by preventing reflux. Furthermore, the proximal valves shielding function increases perfusion following contraction. Finally, the superficial system aids in maintaining the perfusion during the contraction phase and reduces the refilling time by 37%.

2.1 Introduction

Orthostatic intolerance is observed in astronauts after spaceflight (Buckey et al., 1996), in patients with spinal cord injury (Claydon et al., 2006), in de-conditioned subjects, e.g. after bed rest (Butler et al., 1991), and is strongly associated with aging (Rutan et al., 1992). In the upright position orthostatic intolerance may result in critical events such as syncope. Because of their high compliance and high storage capacity, veins are believed to play a major role in blood volume shifts from the upper towards the lower body which is associated with orthostatic intolerance (Freeman et al., 2002). In healthy subjects, this fluid shift is compensated for by amongst others maintaining venous return, whereas venous return is impaired in patients with orthostatic intolerance. Venous return can be restored by muscle contraction in the lower limb, which promotes emptying of the venous system. Therefore, improved understanding of the muscle pump effect on lower limb hemodynamics is important to better comprehend the sources of orthostatic intolerance.

The muscle pump is a mechanism that promotes venous return via muscle contraction (Figure 2.1). During muscle contraction, the extravascular pressure increases and exceeds the intravascular pressure resulting in the collapse and emptying of the embedded deep veins (Laughlin, 1987; Nådland et al., 2009; Rowell, 1993). Unidirectional flow is guaranteed by the presence of distal venous valves. During muscle relaxation, the transmural pressure in the deep veins drops and the deep veins refill from the micro-circulation, resulting in distal valve opening and proximal valve closure, preventing reflux (Laughlin, 1987). In the upright position the refilling time is expected to decrease due to increased perfusion pressure, as closure of the proximal venous valves reduces the distal venous pressure (shielding) (Pollack and Wood, 1949). It is hypothesized that superficial veins, connected to the deep veins by perforating veins, might further promote the efficiency of the muscle pump. Additional valves in the perforating veins allow flow only in superficial-to-deep direction (Meissner, 2005) and, as a consequence, promote venous return during contraction and venous filling during the relaxation phase. The collapsibility of the veins and the dynamics of the venous valves, that direct the blood towards the heart and shield hydrostatic pressure, are believed to be the main physiological factors in the muscle pump effect (Rowell, 1993).

In this study, venous hemodynamics during muscle contraction and relaxation are investigated using a mathematical modeling approach that enables simultaneous analysis of venous collapse and valve dynamics. Furthermore, it allows study of the influence of independent parameter variation. A one-dimensional pulse wave propagation model is used, which has been well-established to examine and predict arterial hemodynamics (Bode et al., 2012; Leguy et al., 2010; Reymond et al., 2009; van de Vosse and Stergiopulos, 2011), but has only been applied in few studies

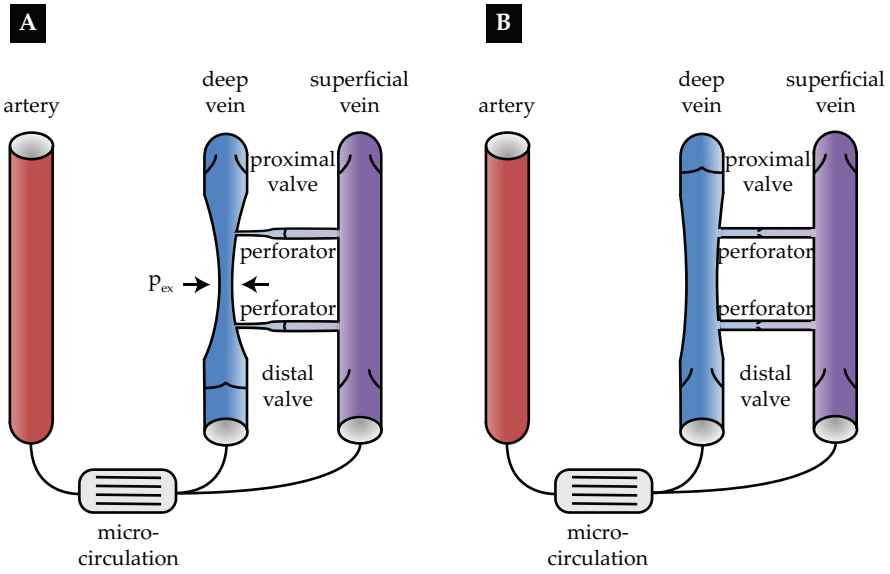

Figure 2.1: Schematic representation of the muscle pump effect during the **A** contraction and **B** relaxation phase. During contraction, the deep vein collapses due to the extravascular pressure p_{ex} exceeds the intravascular pressure. Venous return is increased, whereas back-flow and flow to the superficial system is blocked by the distal and perforator valves. During the relaxation, the deep vein is refilled from both the artery and the superficial vein, while the perforator valves open and the proximal valve is closed to prevent back-flow.

to model venous hemodynamics (Brook et al., 1999; Müller and Toro, 2014). Modeling venous hemodynamics is challenging because, in contrast to arteries, vessel collapsibility and venous valves are important for many applications. Furthermore, more anatomical variation is present in the venous system, e.g. the deep and superficial veins. Most models of venous hemodynamics account for the venous collapsed state under negative transmural pressure by interpreting the collapsible tube law as a non-linear cross-sectional area-pressure (A,p) relation (Fung, 1997; Pedley, 2008; Shapiro, 1977). In addition to collapsibility, changes in hydrostatic pressure between supine and upright position are also important when considering fluid volume shifts and therefore cannot be ignored as is common in arterial models. Gravity has been included in lumped-parameter models using an additional pressure source (Snyder and Rideout, 1969) and can straightforwardly be included in the momentum equation of 1D pulse wave propagation models (Marchandise and Flaud, 2010), resulting in a continuous gravity field. The inclusion of venous valves within such models allows the transient shielding of hydrostatic pressure to be simulated (Zervides et al., 2008) and their action to prevent back-flow. Valves are often represented by a perfect diode in circulatory models (Bovendeerd et al., 2006), whereas more detailed models include gradual opening and closing behaviour based on the transvalvular pressure drop (Mynard et al., 2012) or force balance on the valve leaflets (Korakianitis and Shi, 2006).

Numerical studies of the muscle pump have been reported by Marchandise and Flaud (2010) and Fullana and Zaleski (2008). Marchandise and Flaud (2010) simulated the contraction phase of the muscle pump considering changes in cross-sectional area and wave speed of a collapsing tube, which were validated against *in vitro* measurements. A normal and pathological case were simulated by inclusion and exclusion of a venous valve in the distal boundary conditions. Fullana and Zaleski (2008) performed a computational study of the muscle pump including a more extensive anatomy of the venous system and although they did include valves, they did not examine resulting valve dynamics. Although these studies have been able to model specific venous physiology, an analysis of venous valve dynamics combined with an increased perfusion pressure and the communication of deep and superficial venous systems during a muscle contraction has, to our knowledge, not yet been undertaken.

Therefore, the aim of this study is to investigate the physiological mechanisms of the calf muscle pump and its effect on venous return in the upright position using a modeling approach. The 1D pulse wave propagation model of Kroon et al. (2012) is extended to include venous properties: a collapsible tube law is implemented to account for the non-linear A,p-relation, gravity is included in the momentum equation to account for the hydrostatic pressure and venous valves are included to prevent

back-flow. We will show how the model can be used to explain the different physiological mechanisms of muscle pump function, including the effect of (1) venous valves, (2) hydrostatic pressure and (3) the deep and superficial venous system. In three configurations with different level of detail, muscle contraction and relaxation will be simulated by applying changes in extravascular pressure to study the valve dynamics and the hemodynamics.

2.2 Methods

To study calf muscle pump function, a numerical model of the arteries and veins in the calf was built. The calf muscle is perfused mainly by three arteries: peroneal, anterior tibial, and posterior tibial, which are each associated with two veins (Meissner, 2005). Apart from these vessels, all embedded in the calf muscle, a superficial system, of which the great and small saphenous vein are the largest vessels, supplies the skin with blood (Meissner, 2005). The superficial veins are connected to the deep venous system by a varying number of perforating veins, which contain venous valves that open to allow flow towards the deep venous system (Meissner, 2005). The model used in this study contains all of these types of vessels. However, to reduce the complexity of the system, but retain all essential elements, a generic approach is chosen and one vessel of each type was included. Also for the inclusion of venous valves a generic approach is chosen, by including a single proximal and distal valve for each deep and superficial vein and one valve in each perforating vein.

Three anatomical configurations are considered in this study (Figure 2.2); from the simplest valveless single artery-vein configuration, via the inclusion of valves, to the most complex arrangement which includes the superficial and perforating veins. By comparing the different configurations the importance of venous valves, hydrostatic pressure and the superficial system is studied. Simulation of hemodynamics was undertaken in both the supine and upright positions, where the gravity vector is aligned with the vessel axis in the upright position. The model formulation includes both 1D and 0D components for which the governing equations are provided in Sections 2.2.1 to 2.2.7 and the numerical formulation is provided in Section 2.2.8. The geometrical parameters used for each region of the model were taken from the literature (Müller and Toro, 2014) and are provided in Table 2.1, with the numbering of each anatomical segment given in Figure 2.2. The constant parameters used for the governing equations presented in Sections 2.2.1 to 2.2.7 are given in Table 2.2.

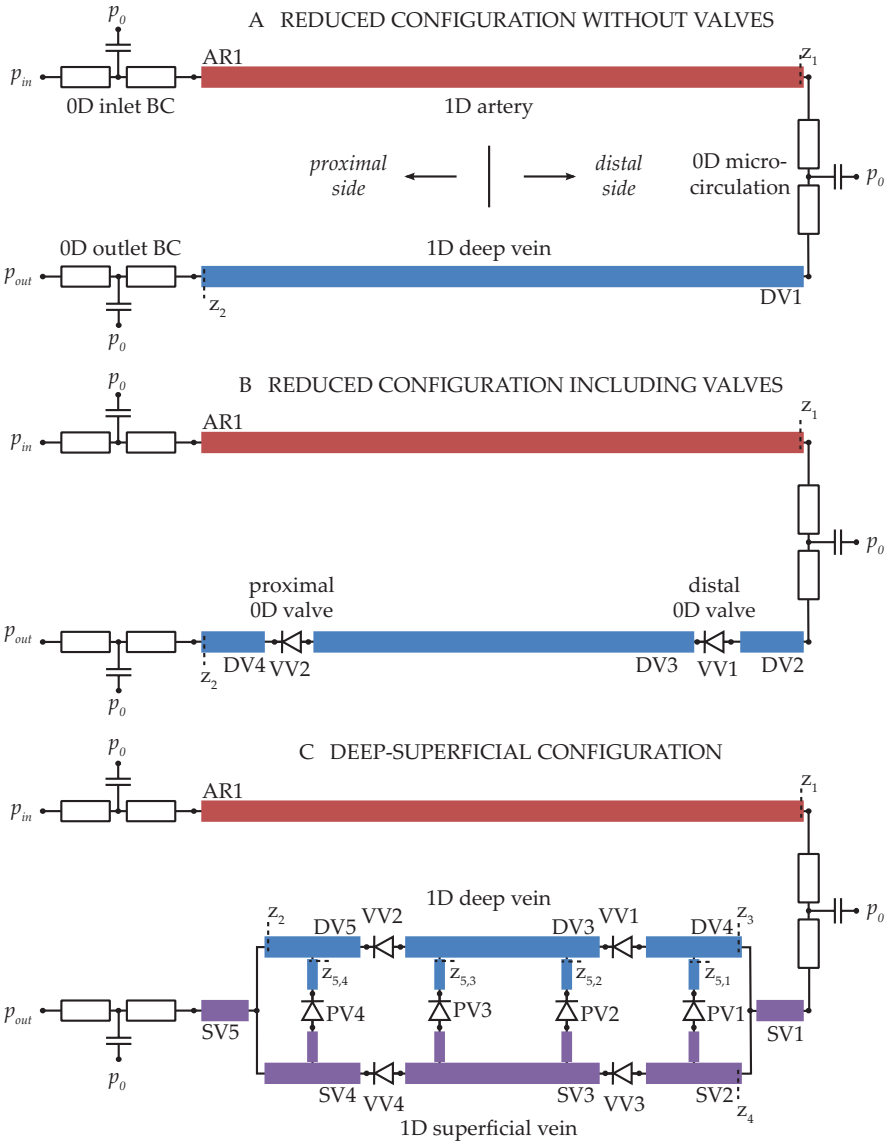

Figure 2.2: Three different model configurations: **A** reduced configuration without valves **B** reduced configuration including valves **C** deep-superficial configuration. All three configurations consist of different elements: 1D arteries (AR) and deep (DV) and superficial veins (SV), 0D venous valves (VV), micro-circulation and in- and outflow boundary conditions (BC). The length and radius of the 1D elements are not to scale (geometrical parameters of all 1D segments can be observed in Table 2.1). The z-positions indicate the locations where the flows are determined as explained in Section 2.2.8.

Table 2.1: Geometrical parameters of the different vessels (Müller and Toro, 2014) as depicted in Figure 2.2. The four perforating veins contain of a valve (PV#-V), a deep (PV#-D) and a superficial (PV#-S) vein of which the parameters are noted separately.

Vessel	Numbering (Figure 2.2)	Radius [mm]	Length [cm]	Configuration (Figure 2.2)
artery	AR1	2.5	34	A,B,C
deep vein	DV1	1.5	34	A
	DV2	1.5	4	B
	DV3	1.5	24	B,C
	DV4	1.5	4	B
	DV5	1.5	2	C
	DV6	1.5	2	C
superficial vein	SV1	3.5	2	C
	SV2	1.5	2	C
	SV3	1.5	24	C
	SV4	1.5	2	C
	SV5	3.5	2	C
venous valves	VV1	1.5	1	B,C
	VV2	1.5	1	B,C
	VV3	1.5	1	C
	VV4	1.5	1	C
perforating vein	PV#-S	0.5	1	C
	PV#-V	0.5	1	C
	PV#-D	0.5	1	C

Table 2.2: Constant model parameters

Symbol	Value	Unit	Description
ρ	1050	kg m^{-3}	Blood mass density (Westerhof et al., 1969)
g	9.81	m s^{-1}	Gravitational acceleration
ν	0.5	-	Poisson's ratio (Westerhof et al., 1969)
E	1.6	MPa	Arterial Young's modulus (Westerhof et al., 1969)
$p_{\text{ref,art}}$	13	kPa	Arterial reference pressure (Bessems et al., 2007)
b	10	-	Constant Shapiro's tube law (Shapiro, 1977)
c	$-\frac{3}{2}$	-	Constant Shapiro's tube law (Shapiro, 1977)
A_0^+	1.37	-	Fitting constant
p_a^+	-2.53	-	Fitting constant
p_b^+	3.02	-	Fitting constant
B	0.108	-	Fitting constant
A_0^-	1.28	-	Fitting constant
p_a^-	-1.49	-	Fitting constant
p_b^-	2.03	-	Fitting constant
γ	4	-	Fitting constant
η	4.05	mPa s	Dynamic blood viscosity (Letcher et al., 1981)
Δp	12	kPa	Pressure drop over micro-circulation (Hall, 2010)
τ_{RC}	2	s	RC-time (Bessems et al., 2007)
p_{max}	20	kPa	Maximal extravascular pressure (Rowell, 1993)
p_{in}	13.4	kPa	Inlet pressure boundary condition
p_{out}	667	Pa	Outlet pressure boundary condition
p_0	0	Pa	Extravascular pressure in windkessel elements

2.2.1 1D Pulse wave propagation: arteries and veins

The relation between pressure and flow in the large arteries and veins are based on the one-dimensional equations of mass and momentum balance (Hughes and Lubliner, 1973; van de Vosse and Stergiopulos, 2011):

$$C\frac{\partial p_{\text{tr}}}{\partial t} + \frac{\partial q}{\partial z} = 0, \tag{2.1}$$

$$\frac{\partial q}{\partial t} + \frac{\partial A\overline{v_z^2}}{\partial z} + \frac{A}{\rho}\frac{\partial p}{\partial z} = \frac{2\pi a}{\rho}\tau_{\text{w}} + Ag_{\text{z}}, \tag{2.2}$$

where C is the compliance per unit length, p_{tr} is the transmural pressure, t is the time, q is the flow and z is the axial coordinate. Additionally, in the momentum balance equation $A = A(p_{\text{tr}})$ is the cross-sectional area, $\overline{v}_{\text{z}}$ is the velocity in z-direction averaged over the cross-sectional area, p is the intravascular pressure, $a = \sqrt{A/\pi}$ is the radius and ρ is the density of the blood. The wall shear stress is given by τ_{w} and $g_{\text{z}} = \mathbf{g} \cdot \mathbf{e_z}$ is the contribution of gravitational acceleration in the z-direction, where $\mathbf{g}$ is the gravity vector. The wall shear stress and non-linear convection term are estimated using the approximated velocity profile of Bessems et al. (2007). The gravity term is included in the derivation of the velocity profile. The resulting wall shear stress and non-linear convection term are:

$$\tau_w = -\frac{2\eta}{1-\zeta_{\text{c}}}\frac{q}{A} + \frac{a}{4}(1-\zeta_{\text{c}})\left\{\frac{\partial p}{\partial z} - \rho g_{\text{z}}\right\} \quad \text{and} \quad A\overline{v_{\text{z}}^2} \approx \delta_1\frac{q^2}{A}, \tag{2.3}$$

where η is the dynamic viscosity, ζ_{c} is the dimensionless core thickness and δ_1 a function of ζ_{c}. To solve the above equations a constitutive law relating cross-sectional area and pressure is needed for both arteries and veins.

2.2.2 Constitutive law for arteries

To capture the mechanical behaviour of the arterial wall, the system of equations is completed with a linear A,p-relation for the arteries:

$$A = A_{\text{ref,art}} + C(p_{\text{tr}} - p_{\text{ref,art}}), \tag{2.4}$$

where $A_{\text{ref,art}}$ is the cross-sectional area at reference pressure $p_{\text{ref,art}}$ and C is the linearized compliance per unit length around reference pressure $p_{\text{ref,art}}$. The compliance is determined using thin-walled-cylinder theory for a linear isotropic elastic material:

$$C = \left.\frac{\partial A}{\partial p_{\text{tr}}}\right|_{p_{\text{tr}}=p_{\text{ref,art}}} = \frac{2\pi(1-\nu^2)a_0^3}{hE}, \tag{2.5}$$

where $a_0 = \sqrt{A_{\text{ref,art}}/\pi}$ is the reference radius, ν is the Poisson's ratio, $h \approx a_0/10$ is the vessel wall-thickness (Westerhof et al., 1969) and E is the Young's modulus.

2.2.3 Constitutive law for veins

As the internal venous pressure is very low, the influence of the extravascular pressure on the mechanical behaviour of the venous cross-sectional area is significant and even negative transmural pressure can be reached, resulting in venous collapse. As the mechanical behaviour of the venous wall is non-linear in this transmural pressure range the proposed relation for the arteries can no longer be used. Therefore, Shapiro (1977) derived the following relation to capture the collapse of the veins based on *in vitro* measurements.

$$p_{\text{tr}} = K_{\text{p}}((A/A_{\text{ref,ven}})^b - (A/A_{\text{ref,ven}})^c), \tag{2.6}$$

where K_{p} is the bending stiffness, and b and c are constants that determine the shape of the tube law. To obtain a relation that captures the behaviour described by Equation 2.6, but cast in an A,p-relation, Equation 2.6 is approximated by the following expression, which has a continuous first order derivative.

$$A = A_{\text{ref,ven}} \left\{ h(p^*) f^+(p^*) + (1 - h(p^*)) f^-(p^*) \right\}, \tag{2.7}$$

where $A_{\text{ref,ven}}$ is the reference cross-sectional area at zero transmural pressure and $p^* = p_{\text{tr}}/K_{\text{p}}$ is the dimensionless pressure. The functions f^+ and f^- are fits of the positive and negative pressure part of the original tube law of Shapiro (1977) and $h(p^*)$ is a scaling function.

$$f^+(p^*) = \frac{A_0^+}{\pi} \left(\tan^{-1} \left(\frac{p^* - p_a^+}{p_b^+} \right) + \frac{\pi}{2} \right), \tag{2.8}$$

$$f^-(p^*) = B + \frac{A_0^-}{\pi} \left(\tan^{-1} \left(\frac{p^* - p_a^-}{p_b^-} \right) + \frac{\pi}{2} \right), \tag{2.9}$$

$$\text{and} \qquad h(p^*) = \frac{1}{\pi} \left(\tan^{-1} \left(\frac{\gamma p^*}{\pi} \right) + \frac{\pi}{2} \right), \tag{2.10}$$

where B, A_0^-, p_a^-, p_b^-, A_0^+, p_a^+, p_b^+ and γ are fitting constants determining the shape of the A,p-relation. Venous compliance is calculated as the derivative of A with respect to p_{tr}. Superficial veins differ from deep veins as they are less influenced by a muscle contraction, which is included in the model by applying p_{ex} only to the deep veins. Figure 2.3 shows a comparison between this approximation and the Shapiro tube law.

2.2.4 0D Venous valves

The different states of the venous valves result in changes in resistance to flow. This is included in the model using a diode with an extra inertial term to represent the

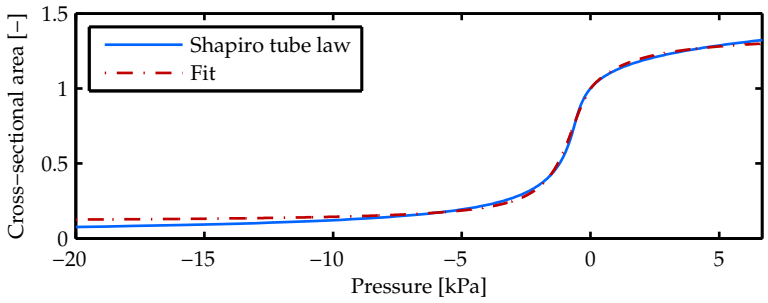

Figure 2.3: A,p-relation according to Shapiro tube law: Equation(2.6) (-) and the fit: Equation (2.7) (-·).

inertia of the blood. The pressure-flow relation within the valve region is defined as follows:

$$\Delta p = L\frac{\partial q}{\partial t} + Rq, \tag{2.11}$$

where L is the inertance and R is the resistance, defined to be equal to a Poisseuille resistance in open state and very large in closed state.

$$L = \frac{\rho l_{\text{eff}}}{A_0} \quad \text{and} \quad R = \frac{8\pi\eta l_{\text{eff}}}{A_{\text{eff}}^2} \tag{2.12}$$

where the effective cross-sectional area A_{eff} is

$$A_{\text{eff}} = \begin{cases} A_0 & \text{if the valve is open} \\ 1 \cdot 10^{-6} A_0 & \text{if the valve is closed} \end{cases}, \tag{2.13}$$

where $l_{\text{eff}} = 5a_0$ is an effective length, representing the geometrical region in which the inertial forces are dominant due to the presence of the valve, and cross-sectional area A_0 is taken equal to the reference cross-sectional area of the connecting venous elements. Opening occurs on a positive transmural pressure difference and the closure on negative flow.

2.2.5 0D Micro-circulation

To capture the pressure drop and the storage capacity of the micro-circulation a windkessel element consisting of two resistances $R_{\text{wk,i}}$ $(i = 1, 2)$ and a compliance C_{wk} connected to the extravascular pressure p_0 is used, described by

$$\Delta p_R = R_{\text{wk,i}} q, \qquad \frac{\partial p_{\text{tr}}}{\partial t} = \frac{1}{C_{\text{wk}}} q, \tag{2.14}$$

where the first resistance $R_{\text{wk,1}}$ is set equal to the characteristic wave impedance of the connecting arterial element given by

$$R_{\text{wk,1}} = \sqrt{\frac{\rho}{A_0 C}}. \tag{2.15}$$

The total resistance is defined by the ratio of the pressure drop over the micro-circulation Δp divided by the mean baseline flow $\overline{q}$

$$R_{\text{wk,tot}} = R_{\text{wk,1}} + R_{\text{wk,2}} = \frac{\Delta p}{\overline{q}}. \tag{2.16}$$

Baseline flow is defined as $\frac{1}{6}$ of a population averaged femoral artery flow of 2.78 mL/s (Leguy et al., 2013), because only one of the six deep veins is included in the geometry. When the superficial system is included, $\frac{1}{3}$ of the femoral artery flow is used in order to maintain the same baseline flow in the deep vein. Finally, the compliance of the micro-circulation is computed based on a representative value of the time constant τ_{RC}, defining the decay of the pressure wave in diastole (van de Vosse and Stergiopulos, 2011)

$$\tau_{\text{RC}} = R_{\text{wk,2}} C_{\text{wk}}. \tag{2.17}$$

The extravascular pressure of the micro-circulation is set to p_0.

2.2.6 0D Boundary conditions

The arterial inlet and venous outlet are both connected to windkessel elements with the same form as that of the micro-circulation. To avoid reflections of the higher order harmonics the resistance connected to the 1D element is calculated using Equation (2.15), the second resistance is set equal to the first one and the compliance is again calculated using Equation (2.17). It is noted that the windkessel elements are not included to represent the vascular tree attached to the reduced circulation and therefore the true value of the second resistance is of minor importance. The extravascular pressure of the inlet and outlet boundary condition is set to p_0. Inlet and outlet boundary conditions are set to a constant pressure p_{in} and p_{out} respectively, to simulate the pressure gradient between the arterial and venous circulation.

2.2.7 Muscular extravascular pressure

The extravascular pressure generated during the muscle contraction is applied to the deep venous elements and not to the artery and superficial vein, as the embedded artery is assumed to be less influenced due to its high intravascular pressure. Furthermore, the influence of muscle contraction on the superficial vein is assumed to

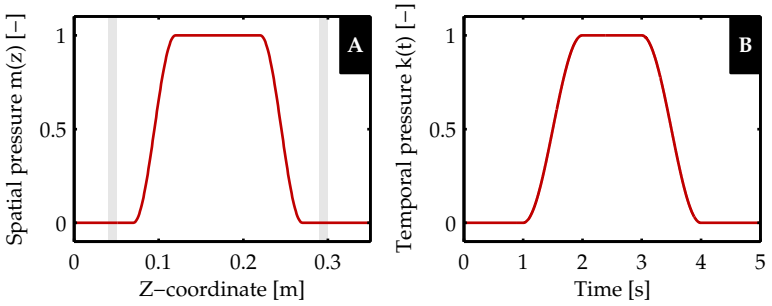

Figure 2.4: Extravascular pressure of the deep veins is increased to simulate a muscle contraction. Plot **A** and **B** show the spatial $m(z)$ and temporal $k(t)$ course of extravascular pressure as applied to the deep venous elements respectively (see Appendix A for the full equations of $m(z)$ and $k(t)$). The grey area's in the spatial plot indicate the location of the venous valves.

be negligible compared to the influence on the deep vein, due to the location of the superficial vein in the skin. The prescribed extravascular pressure is assumed to be

$$p_{\text{ex,ven}} = p_{\text{max}} k(t) m(z), \tag{2.18}$$

where p_{max} is the maximal value of extravascular pressure, $k(t)$ the temporal course of the extravascular pressure and $m(z)$ the spatial course of the extravascular pressure. The spatial and temporal variation in extravascular pressure are shown in Figure 2.4 and the full equations of $k(t)$ and $m(z)$ are given in Appendix A.

2.2.8 Numerical implementation and post-processing

The governing equations described in Section 2.2.1 to 2.2.7 were solved numerically using the finite element package SEPRAN (Ingenieursbureau SEPRA, Leidschendam, The Netherlands) with the reduced complexity method as described by Kroon et al. (2012). A second order backward difference scheme was used for time discretization with timestep $dt = 1$ ms. The trapezium rule was used for spatial integration with $dz = 10$ mm for arterial and superficial venous elements and $dz = 1$ mm for deep venous elements, as the spatial transmural pressure gradient can be much higher in the deep venous elements due to the prescribed muscle contraction. Pre- and postprocessing was done using MATLAB R2012b (MathWorks, Natick, MA).

To compare the muscle pump function in the different configurations several parameters were defined. First, the additional volume that refills the deep vein from the micro-circulation during the relaxation, called perfusion volume V_{PE}, was calculated as a measure of increase in perfusion. The increase in venous return during the contraction phase is captured in the additional volume that leaves the deep vein,

called venous return V_{VR}. Finally, the reflux volume V_{RE} was calculated as a measure for the volume that refills the veins from the proximal side of the vein, decreasing the effective venous return. V_{PE}, V_{VR} and V_{RE} were calculated using the following relations

$$V_{\text{PE}} = \int_{t=t_0}^{t_{\text{end}}} (q_{\text{art}} - q_{\text{art,bl}})dt \qquad \text{for } q_{\text{art}} > q_{\text{art,bl}}, \tag{2.19}$$

$$V_{\text{VR}} = \int_{t=t_0}^{t_{\text{end}}} (q_{\text{ven}} - q_{\text{ven,bl}})dt \qquad \text{for } q_{\text{ven}} > q_{\text{ven,bl}}, \tag{2.20}$$

$$V_{\text{RE}} = -\int_{t=t_0}^{t_{\text{end}}} (q_{\text{ven}})dt \qquad \text{for } q_{\text{ven}} < 0, \tag{2.21}$$

where q_{art} is the arterial flow into the micro-circulation (at position z_1 in Figure 2.2), $q_{\text{art,bl}}$ is the arterial flow just before the onset of the contraction ($t = 1\ s$), q_{ven} is the venous flow at the end of the deep vein (at position z_2 in Figure 2.2) and $q_{\text{ven,bl}}$ is the venous flow just before the onset of the contraction ($t = 1$ s). Furthermore, to determine the time needed for the deep vein to refill during the relaxation, an estimate for the refilling time t_{fill} was determined from the start of relaxation ($t = 3$ s) until the volume of the deep vein reached 95% of the baseline volume. Finally, to measure the decrease in arterial inflow due to contraction, the change in arterial inflow Δq_{art} was calculated relative to the arterial baseline flow $q_{\text{art,bl}}$. As the computational domain only covered a small part of the calf circulation, relative changes of the previously defined parameters were used to provide an indication of the magnitude of changes between different configurations. Additionally deep and superficial venous inflow were determined at location z_3 and z_4 respectively (Figure 2.2). The perforating inflow was calculated as the sum of the flows at locations z_5.

2.2.9 Simulations and analysis

To demonstrate that the model is able to capture the different aspects of the muscle pump effect the following comparisons were made

- Venous collapsibility: Collapse was demonstrated using a reduced geometry without valves in the supine position as in Figure 2.2A.
- Effect of venous valves: To demonstrate that the venous valves prevent backflow in both the contraction and relaxation phase, a muscle contraction was simulated in a reduced configuration with and without valves (see Figure 2.2B and A respectively), both configurations in the supine position.
- Effect of hydrostatic pressure: The reduced configuration including valves was simulated in the supine and upright positions to examine the influence of hydrostatic pressure (see Figure 2.2B).

- Effect of superficial system: The complex venous system was compared to the reduced geometry in the upright position (see Figure 2.2C and B respectively) to investigate the influence of the superficial system on the valve dynamics and the hemodynamics.

2.3 Results

The hemodynamics during a muscle contraction are reported using the different model configurations shown in Figure 2.2. The results are reported in four sections which examine the course of the deep venous collapse, the effect of venous valves, the effect of hydrostatic pressure and the importance of the superficial system respectively.

2.3.1 Venous collapsibility

The time and spatial course of venous collapse during a muscle contraction is studied in the configuration without venous valves (see Figure 2.2A). The temporal and spatial plots of cross-sectional area of the deep vein at several axial positions and time points respectively are shown in Figure 2.5. For clarity, the temporal plots (Figure 2.5C,E) are split into the distal and proximal region and the spatial plots (Figure 2.5D,F) are split into time points during contraction and relaxation.

During the contraction phase in the temporal plot ($1\ \text{s} \leq t \leq 2\ \text{s}$, Figure 2.5C,E) it can be observed that the collapse starts at the proximal side, as the blue and black curve in the proximal plot show a higher gradient than the green and orange curve in the distal plot. Furthermore, the uncollapsed proximal and distal part of the vein increases in cross-sectional area during the contraction phase, which is best observed in Figure 2.5D while comparing all curves to the black curve (before contraction). In the subsequent relaxation phase the vein refills from the distal side.

2.3.2 Effect of venous valves

The influence of venous valves on venous hemodynamics during muscle pump activation was assessed by comparing the configuration without venous valves to the one with venous valves (Figure 2.2A and B respectively). The results from the two simulations are compared in Figure 2.6, which reports the extravascular pressure and the state of the proximal (VV2) and distal (VV1) valves (Figure 2.6A), the arterial inflow (Figure 2.6B), venous outflow (Figure 2.6C) and venous volume (Figure 2.6D). Grey regions in Figure 2.6B and C indicate the extra volume due to perfusion

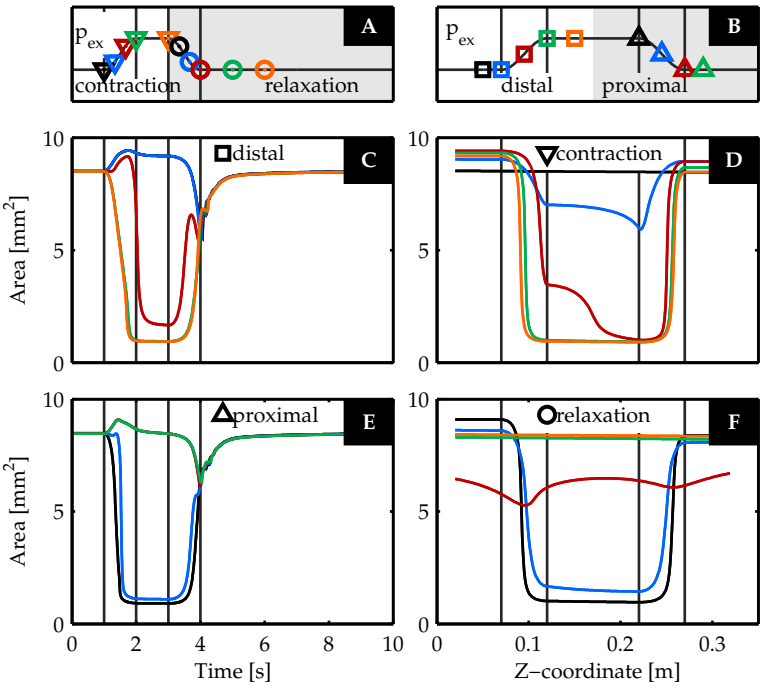

Figure 2.5: Venous cross-sectional area in the reduced configuration without valves (see Figure 2.2A) over time (**C**,**E**) and over the z-coordinate (**D**,**F**) with the corresponding extravascular pressure on top (**B** and **A** respectively). The temporal plots are divided in the distal (C) and proximal (E) course of cross-sectional area. The spatial plot are divided in contraction (D) and relaxation (F) plots. The different lines represent different spatial and temporal points, which correspond to the following symbols in the diagonal plots (A,B) of the extravascular pressure: temporal plots of the distal (C, □ in B) and proximal (E, △ in B) part of the deep vein, and spatial plots of the contraction (D, ▽ in A) and relaxation (F, ○ in A) phase.

Table 2.3: Venous return (V_{VR}), perfusion (V_{PE}) and reflux volumes (V_{RE}), refilling time t_{fill} and the relative decrease in arterial inflow during the muscle contraction Δq_{art} as indicated in Figure 2.6, 2.7 and 2.9 and explained in Equation (2.20), (2.19) and (2.21)

	V_{VR} [mL]	V_{PE} [mL]	V_{RE} [mL]	t_{fill} [s]	Δq_{art} [%]
No valves, supine (Figure 2.2A)	0.87	0.10	0.46	1.69	106
Valves, supine (Figure 2.2B)	0.88	0.17	0.00	2.62	97
Valves, upright (Figure 2.2B)	0.92	0.26	0.00	2.45	97
Complex venous system (Figure 2.2C)	0.85	0.16	0.00	1.54	6

V_{PE}, venous return V_{VR} and reflux V_{RE} for which the numerical values are reported in Table 2.3.

During the initial phase of the muscle contraction ($1\ s \leq t \leq 1.5\ s$) increased venous outflow is observed in Figure 2.6C. In the second part of the contraction (1.5 s $\leq t \leq 2$ s), the flow decreases and stabilizes under constant extravascular pressure (2 s $\leq t \leq 3$ s). The extra volume venous return V_{VR} is only slightly increased after the inclusion of venous valves. Along with increased venous outflow, a decrease in arterial inflow of 97% is observed during the contraction in the case where valves are included. When no valves are present, arterial flow decreases below zero to -6% of baseline arterial flow, resulting in back-flow. In Figure 2.6A the distal valve (VV1) is observed to close during part of the contraction.

In the subsequent relaxation phase ($t > 3$ s) arterial flow increases, resulting in an extra perfusion volume V_{PE} of 0.17 mL and 0.10 mL with and without valves respectively. The proximal valve (VV2) closes and the venous flow reduces to zero when valves are included, resulting in a zero reflux volume V_{RE}. Without valves negative venous outflow results in a reflux volume V_{RE} of $0.46\ mL$ that refills the vein from the proximal side. Figure 2.6D compares the volume of the deep vein over time in both cases and reveals a faster refilling if no valves are included, quantified by measurement of the refilling time without valves, $t_{fill} = 1.69$ s, and with valves, $t_{fill} = 2.62$ s (Table 2.3).

2.3.3 Effect of hydrostatic pressure

The effect of hydrostatic pressure was studied by comparing the hemodynamics in the supine and upright positions, with valves included in both cases (Figure 2.2B). The results from the two simulations are compared in Figure 2.7, which reports the extravascular pressure and the state of the proximal (VV2) and distal (VV1) valves (Figure 2.7A), the arterial inflow (Figure 2.7B), venous outflow (Figure 2.7C) and perfusion pressure (Figure 2.7D). Grey regions of Figure 2.7B and C indicate the extra volume due to perfusion V_{PE} and venous return V_{VR} for which numerical values are

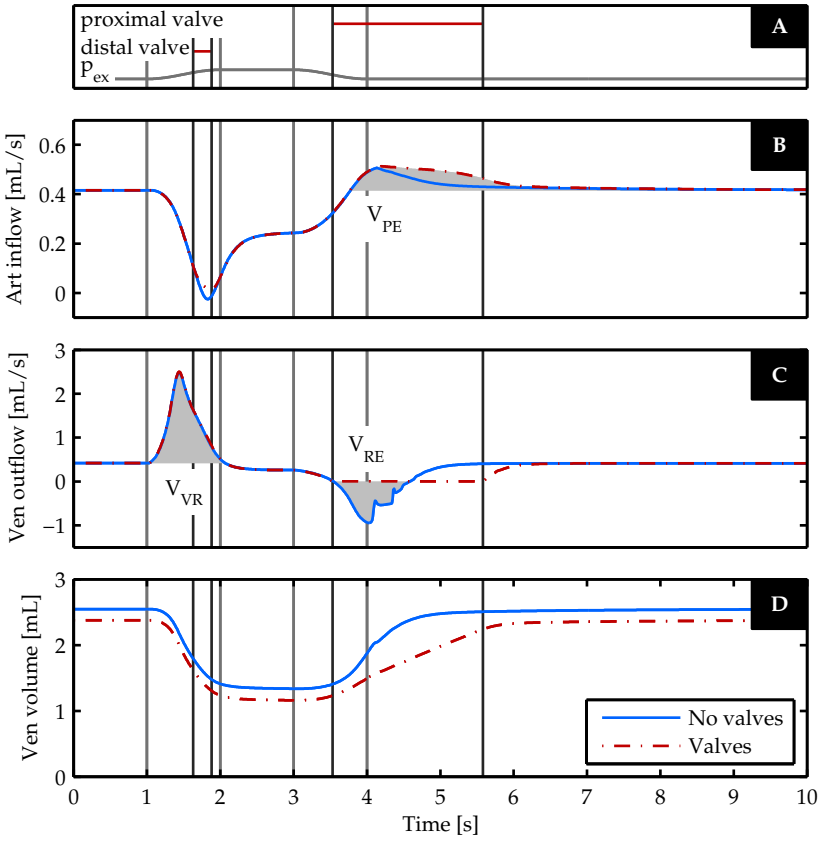

Figure 2.6: The muscle pump effect is shown in the reduced geometry in the case valves are excluded (blue) and included (red) (see Figure 2.2A and B). In plot **A** the course of the extravascular pressure and the state of the proximal (VV2) and distal (VV1) valve are shown, where the closed state is denoted with a solid line. Plot **B** and **C** show the arterial inflow and venous outflow respectively. The grey areas indicate the extra perfusion (V_{PE}), venous return (V_{VR}) and reflux volume (V_{RE}) of which the values can be found in Table 2.3. Plot **D** shows the volume inside the deep vein.

reported in Table 2.3.

During the contraction phase (1 s $\leq t \leq 2$ s) similar flow patterns are observed in supine and upright position, with a small increase of 0.04 mL in the venous return volume V_{VR} in the upright position. In the subsequent relaxation phase ($t > 3$ s), the arterio-venous perfusion pressure (Figure 2.7D) is elevated, while the proximal valve (VV2) is closed, with a maximal difference of 2.3 kPa. This increased perfusion pressure is accompanied with an increase in arterial inflow and a 0.09 mL increase in perfusion volume V_{PE}. The venous refilling process is slightly faster in the upright position as it reaches a 95% refilling in 2.45 s instead of 2.62 s (see Table 2.3).

Figure 2.8 shows the spatial variation of internal venous pressure and cross-sectional area at different time points during the relaxation phase in upright position. The pressure gradient over the whole length of the vein is observed to be equal to $-\rho g$ at $t = 6.0$ s.

2.3.4 Effect of superficial system

The influence of the superficial venous system was studied by comparing the hemodynamics in a reduced and deep-superficial configuration (including one superficial and four perforating veins). Both models included valves and were simulated in upright position (Figure 2.2B and C respectively). The results from the two simulations are compared in Figure 2.9, which reports the extravascular pressure and the state of the proximal (VV2) and distal (VV1) valves (Figure 2.9A), the arterial inflow (Figure 2.9B), deep venous outflow (Figure 2.9C) and total venous volume (Figure 2.9D). Grey regions of Figure 2.9B and C indicate the extra volume due to perfusion V_{PE} and venous return V_{VR} for which numerical values are reported in Table 2.3.

During the contraction phase (1 s $\leq t \leq 2$ s) arterial inflow remained high when the superficial system was included ($\Delta q_{\text{art}} = 6\%$) compared with a large reduction when only the deep system was included ($\Delta q_{\text{art}} = 97\%$) (Figure 2.9 and Table 2.3). The venous return during the relaxation phase is slightly reduced with $V_{\text{VR}} = 0.85$ mL in the deep-superficial configuration and $V_{\text{VR}} = 0.92$ mL in the reduced configuration. In the subsequent relaxation phase a faster refilling is observed in the more detailed configuration, quantified by measurement of the refilling time in the reduced configuration, $t_{\text{fill}} = 2.45$ s, and including the superficial system, $t_{\text{fill}} = 1.54$ s (Figure 2.9D and Table 2.3). The perfusion volume in the deep-superficial configuration is decreased by 0.10 mL compared to the reduced configuration.

Figure 2.10 shows detailed venous dynamics for the deep-superficial configuration, reporting the state of one perforating valve and the extravascular pressure (Figure

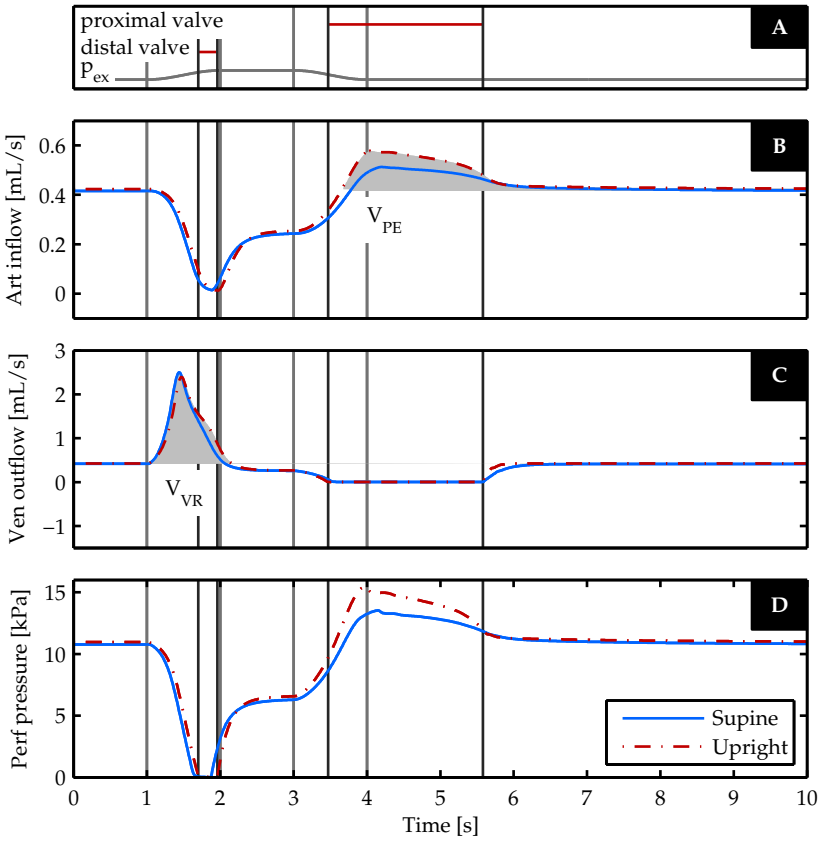

Figure 2.7: The muscle pump effect is shown in the reduced configuration including valves (see Figure 2.2B) in the supine (blue) and upright (red) positions. In plot **A** the course of the extravascular pressure and the state of the proximal (VV2) and distal (VV1) valve are shown, the closed state is denoted with a solid line. Plot **B** and **C** show the arterial inflow and venous outflow respectively. The grey areas indicate the extra perfusion (V_{PE}) and venous return (V_{VR}) of which the values can be found in Table 2.3. Plot **D** shows the perfusion pressure.

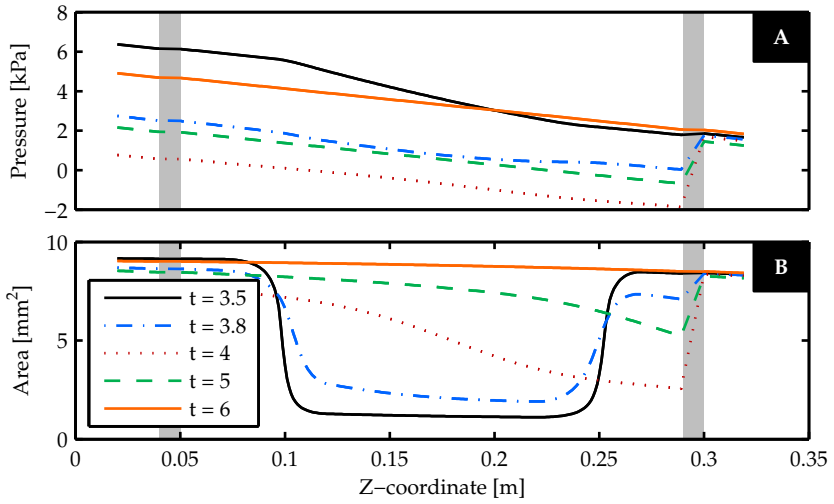

Figure 2.8: Spatial pressure and cross-sectional area at different point in time during the relaxation in upright position (Figure 2.2B). The grey area's represent the venous valves.

2.10A), the deep venous inflow (Figure 2.10B), superficial venous inflow (Figure 2.10C) and total perforating venous inflow (Figure 2.10D).

During the contraction phase ($1\text{ s} \leq t \leq 2\text{ s}$) deep venous inflow decreases and superficial inflow increases. In the subsequent relaxation phase ($t \geq 3$ s) superficial inflow decreases, deep inflow increases and perforator inflow increases. The perforating valve is closed during the whole contraction phase ($1\text{ s} \leq t \leq 3$ s) and alters state continuously after the relaxation ($4\text{ s} \leq t \leq 6$ s).

2.4 Discussion

This study examined the main mechanisms of the muscle pump effect using a 1D pulse wave propagation model that includes venous collapsibility, gravity and venous valves. Different configurations of the model were used to investigate the effect of venous valves, hydrostatic pressure and the superficial venous system on the valve dynamics and hemodynamics during calf muscle contraction. The results presented in Section 2.3 show the details of the hemodynamics observed within each of the model configurations. The following discussion compares these results with other publications which report specific features of the venous behaviour along with opportunities for further refinement of the modeling approach.

In the current study muscle contraction was simulated by increasing extravascular

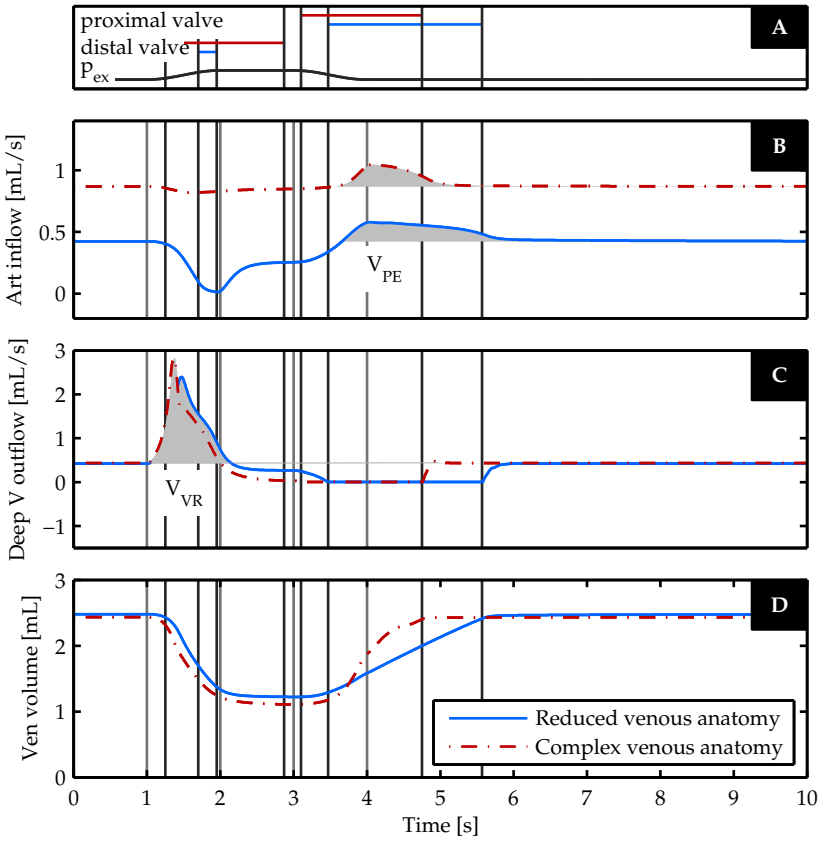

Figure 2.9: The muscle pump effect is shown with the absence and presence of the superficial venous system (see Figure 2.2B and C). In plot **A** the course of the extravascular pressure and the state of the proximal (VV2) and distal (VV1) valve are shown, the closed state is denoted with a solid line. Plot **B** and **C** show the arterial inflow and venous outflow respectively. The grey areas indicate the extra perfusion (V_{PE}), venous return (V_{VR}) and reflux volume (V_{RE}) of which the values can be found in Table 2.3. Plot **D** shows the volume inside the deep vein.

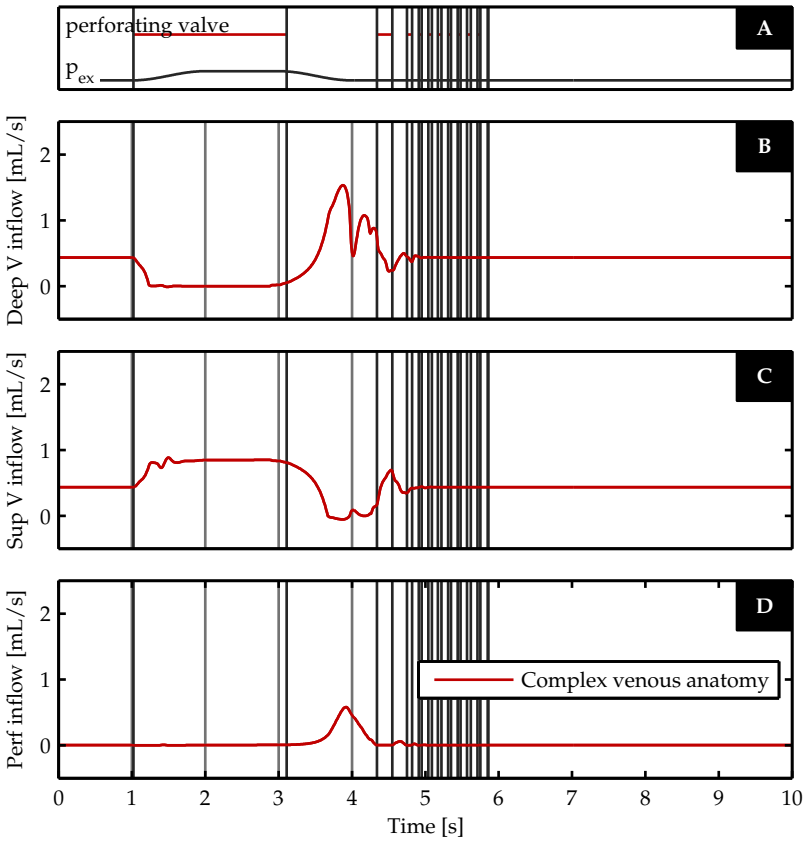

Figure 2.10: The muscle pump effect is shown with the absence and presence of the superficial venous system (see Figure 2.2B and C). In plot **A** the course of the extravascular pressure and the state of the proximal and distal valve are shown, where the closed state is denoted with a solid line. Plot **B**, **C** and **D** show the deep venous, superficial and total perforating venous inflow respectively.

pressure on the deep veins, resulting in a collapse developing from the proximal towards the distal side of the vein. This behaviour is in agreement with the fast collapse near the outlet of the tube observed in the simulations and *in vitro* experiments of Marchandise and Flaud (2010), which can physically be explained by the lower hydrostatic pressure at the proximal end. Collapse results in an increased venous outflow with a peak value of five times the baseline flow. These results are in line with the sevenfold flow augmentation observed numerically and *in vivo* by Fullana and Zaleski (2008) in the common femoral vein. The results presented in Section 2.3 support the *in vivo* observations of Crisóstomo et al. (2014) that venous flow velocity augmentation is not significantly different between patients with venous valve insufficiency and healthy subjects. This can be considered by comparing results between the models with and without valves, where the absence of valves represents the extreme case of valve incompetence, which is often a feature of chronic venous disease. The increased arterial flow observed during the refilling shows the same behaviour as observed by Fullana et al. (2003): initial rapid increase, quasi-steady filling resulting in an almost linear decay in flow, and a final stage, where the flow goes back to its baseline value. The spatial and temporal course of collapse are in line with previous studies.

The main effects of including venous valves were observed in the relaxation phase. Without valves the refilling of the vein occurred from both the distal and proximal side. Refilling from the proximal side resulted in a reflux volume of 0.46 mL, 53% of the extra venous return volume generated during the muscle contraction. The consequence of single-sided refilling, when valves are included, is an associated increase in both refilling time t_{fill} and perfusion volume V_{PE}. We found in this study that the proximal valve is essential to the efficiency of the muscle pump, whilst the distal valve does not significantly impede arterial back-flow, as the high resistance of the micro-circulation prevents this, both with and without valves.

Including hydrostatic pressure in upright position increased the arterial inflow during the relaxation phase, as a result of the increased perfusion pressure. Although one might logically relate the increased perfusion pressure to hydrostatic pressure shielding by the proximal valve, the observed increase of perfusion pressure of 2.3 kPa cannot be accounted for by the hydrostatic pressure of the 5 cm segment of vein proximal to the valve (0.5 kPa). Studying the spatial pressure distribution in the vein (Figure 2.8) reveals a pressure drop over the closed proximal valve higher than the contribution of the hydrostatic column alone. This phenomenon was also reported by Zervides et al. (2008) in a numerical study and observed *in vitro* by Raju et al. (1998). This pressure drop is associated with fluid redistribution from the proximal to distal section due to gravitational loading, lowering the pressure below the proximal valve and thereby increasing the pressure drop over the valve. For the

internal deep venous pressure this means that it keeps decreasing until the end of the relaxation due to the low filling and the removal of the extravascular pressure. While filling progresses the deep venous pressure increases until the proximal valve opens. Furthermore, the spatial pressure plot shows a pressure gradient along the vein, that is larger than the hydrostatic pressure gradient in the initial phase of the refilling ($t < 4$ s), which is caused by the resistance of the collapsed area. A similar phenomenon is described by Young and Tsai (1973a,b) while studying the pressure drop over a stenosis. Our study suggests that the total pressure drop along the deep vein is determined by the state of refilling and the resistance of the collapsed area.

The most important effect of including the superficial venous system can be seen in changes in the arterial flow during the muscle contraction. In the configurations with only a deep venous system a decrease in arterial inflow of 97% was observed during the muscle contraction, whereas arterial flow was only reduced by 6% when the superficial system was included in the model. The division of arterial flow between the deep and superficial vein (Figure 2.10) changes significantly during muscle contraction with the deep venous inflow decreasing to zero and a large increase in superficial venous flow. This can be explained by the increased resistance of the deep vein as it collapses, with the superficial vein remaining circular with low resistance. In the subsequent relaxation phase, the flow in the superficial vein is observed to approach zero, whereas the deep venous inflow receives most of the arterial flow, due to the lower pressure in the deep vein. Although the perfusion volume decreases while including the superficial system, the refilling time is 37% shorter. The alteration of open and closed state of the perforating valve in the late relaxation phase seems a numerical artifact, but might also be explained physiologically. During the late relaxation the deep and superficial vein have a similar filling and therefore a similar pressure, which means the pressure difference between deep and superficial easily changes sign and therefore easily opens or closes the valve. Furthermore, it has to be noticed that these fast alterations in valve state have no influence on the general flow dynamics. Summarizing, the superficial system is found to be of importance for maintaining calf perfusion during the contraction phase and decreasing the refilling time in the relaxation phase.

The collapse course of the deep vein is determined by its A,p-relation, which is currently based on the work of Shapiro (1977) and the bending stiffness of Müller and Toro (2014). Using *ex vivo* or *in vivo* pressure and cross-sectional area measurements, as done by Bassez et al. (2001), could provide a more realistic relationship resulting in a more accurate prediction of the volume shifts. However, we expect that effects of an experimentally determined tube law would not be significant for the qualitative study of the muscle pump. The course of the collapse could also be improved while using a more realistic course of extravascular pressure, which is now included as a

smooth sinus function in order to have a clear distinction between the contraction and relaxation phase. An electromyogram (EMG) of a muscle contraction could be used to provide a more realistic course of the extravascular pressure (Maton et al., 2006). Apart from the pressure originating from the muscles, the arteries, running in parallel with the veins, are also known to slightly compress the veins, which experience the arterial pulsatility as an extravascular pressure (Fox, 2001). However, this pressure is expected to be much lower than the extravascular pressure originating from the muscle contraction.

A second important part of the model are the valve elements, which are currently modeled as a resistance and an inertance, and open with a positive pressure gradient and close with negative flow. More advanced models could be used to capture the detailed physiology of venous valve dynamics (Korakianitis and Shi, 2006). Including a continuous valve cross-sectional area would allow slow opening and closing and enable modeling of valve regurgitation (Mynard et al., 2012). The distal valve was shown to be of minor importance in impeding arterial back-flow due to the high resistance of the micro-circulation. However, it has to be noticed that the current configuration is a simplified representation of the calf vasculature. Inclusion of a parallel branch representing the foot vasculature, could increase the importance of the distal valve by blocking back-flow toward the foot during the contraction. Furthermore, in this study only a small number of valves were included to demonstrate the effect of valves at the proximal and distal position. Anatomical data (Meissner, 2005) suggests a higher number of valves in the calf veins. The inclusion of extra venous valves may result in an increased perfusion pressure if a full model of the circulation is considered, whereas this effect is expected to be small when only the calf is modeled.

The current model used a constant pressure boundary condition on both the arterial and venous side, thereby neglecting the arterial and venous pulsatility. Preliminary model results showed that the inclusion of a pulsatile arterial boundary condition did not propagate significant pulsatility to the venous system and did not alter the mean flow dynamics. As venous pulsatility is very variable due to the large influence of breathing and right atrium contraction (Abu-Yousef et al., 1997; Chavhan et al., 2008), a pulsatile venous boundary was not implemented. Therefore, development of a closed loop model is necessary to investigate the influence of pulsatility on the muscle pump effect.

Although a maximal 1.5 fold increase in arterial flow is observed in the relaxation phase, it is much smaller than the up to 7 fold increase observed *in vivo* after a four-second contraction of the calf muscle by Leguy et al. (2013). However, the increase in arterial inflow during the first five seconds is known to be a combination of the muscle pump and rapid vasodilation (Tschakovsky et al., 1996), of which the latter is

currently not included. Extending the model with regulation of the micro-circulation could help in better predicting the arterial flow during the relaxation phase. Previous modeling studies have successfully included local cerebral auto-regulation (Olufsen et al., 2005; Spronck et al., 2012) including myogenic, metabolic, neurogenic and endothelial regulation mechanisms, which could be adapted to simulate changes in calf vascular tone.

The muscle pump effect is not the only mechanism of importance for studying the fluid shift on orthostatic stress. Considering the importance of other regulatory mechanisms such as the baroreflex and the effect of venous return on cardiac output during tilt (Rowell, 1993), requires a more global circulatory model. Olufsen et al. (2005) developed a closed loop model to study the effect of tilt on hemodynamics, while including global autonomic and cerebral auto-regulation. Furthermore, Heldt et al. (2002) studied the effect of tilt and lower body negative pressure (LBNP) using a closed loop lumped parameter model including the arterial and cardiopulmonary baroreflex. However, both models use a lumped parameter approach with a limited number of compartments. These models do not take into account pressure and flow wave propagation phenomena or collapsibility of the veins as reported in this paper. In future research, we aim to develop a global, closed loop 1D pulse wave propagation model of the total circulation, including regulation mechanisms such as the baroreflex and local auto-regulation, to gain further insight into the mechanisms responsible for reducing fluid shifts during tilting.

A further advantage of a closed-loop model is that it allows the influence of the full hydrostatic column to be considered. To demonstrate the influence of this effect in the current model (reduced configuration with and without valves in the upright position) a $\rho g h$ term (with $h = 1.0$ m) was added to the pressure at the inlet and outlet (p_{in} and p_{out} respectively). The results of these simulations, shown in Figure 2.11 and Table 2.4, further highlights the importance of the venous valves as the reflux volume V_{RE} increased to 67% of the venous return volume V_{VR} (Figure 2.11 and Table 2.4). The abrupt increase of venous outflow at the end of the relaxation phase is most probably caused by the fact that, in this pressure regime, a small increase in cross-sectional area is accompanied by a large increase in pressure. Furthermore, a higher perfusion was observed in the relaxation phase, while the perfusion pressure increased.

Apart from studying the muscle pump effect, the current model has potential application to specific clinical conditions. Inclusion of leaking valves could inform understanding of the effect of valve insufficiency on venous hemodynamics. Furthermore, cuff compression is used to promote venous return in particular conditions, the model could be used to study different compression patterns to improve cuff efficiency, as suggested by Simakov et al. (2013). A series of contractions is expected

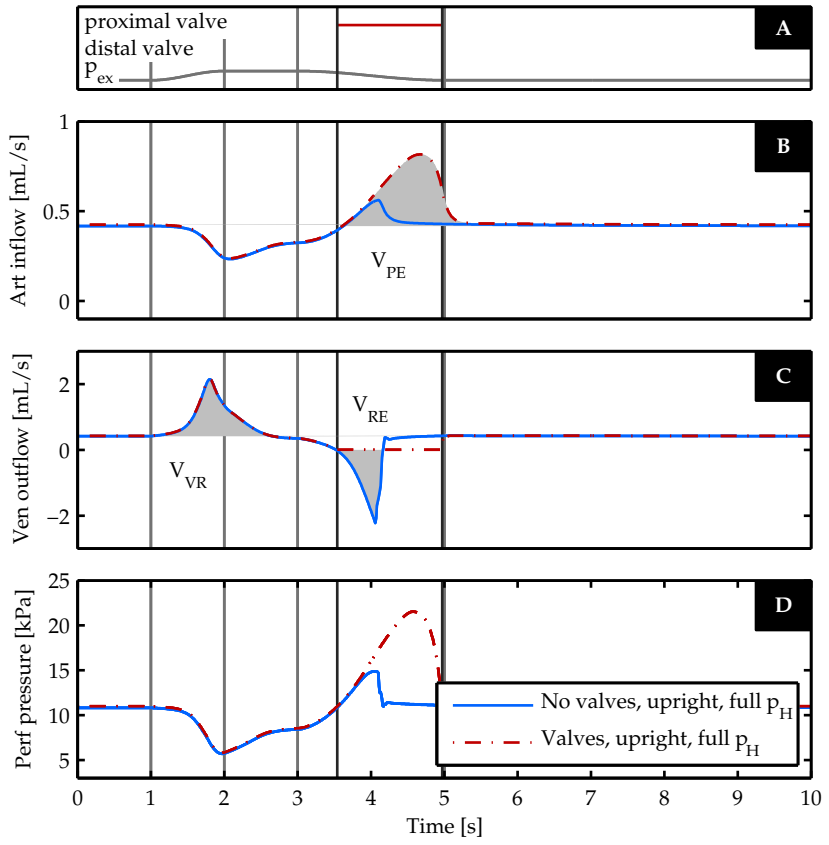

Figure 2.11: The muscle pump effect is shown in the reduced geometry in case valves are ex- (blue) and included (red) with the full hydrostatic column on the boundary conditions (see Figure 2.2A and B). In plot **A** the course of the extravascular pressure and the state of the proximal and distal valve are shown, where the closed state is denoted with a solid line. Plot **B** and **C** show the arterial inflow and venous outflow respectively. The grey areas indicate the extra perfusion (V_{PE}), venous return (V_{VR}) and reflux volume (V_{RE}) of which the values can be found in Table 2.3. Plot **D** shows the perfusion pressure.

Table 2.4: Venous return (V_{VR}), perfusion (V_{PE}) and reflux volumes (V_{RE}), refilling time t_{fill} and the relative decrease in arterial inflow during the muscle contraction Δq_{art} as indicated in Figure 2.11 and explained in Equation (2.20), (2.19) and (2.21)

	V_{VR} [mL]	V_{PE} [mL]	V_{RE} [mL]	t_{fill} [s]	Δq_{art} [%]
No valves, upright, full p_H (Figure 2.2A)	0.87	0.08	0.58	1.10	44
Valves, upright, full p_H (Figure 2.2B)	0.86	0.35	0.00	1.77	44

to result in lower filling of the veins, as a second contraction can start before the vein is fully refilled. This lower filling of the veins results in a lower pressure in the vein, maintaining a higher perfusion pressure. Secondly, this lower venous pressure also results in a smaller pressure difference with the surrounding tissue and therefore less edema is expected. Modeling a series of contractions, therefore necessitates inclusion of filtration mechanisms and local auto-regulation.

2.5 Conclusion

A 1D pulse wave propagation model has been developed which allows the study of lower limb hemodynamics during muscle pump activation. The model is able to predict the increase in venous return during muscle contraction. As the proximal valves close during the relaxation phase reflux is prevented, which without valves resulted in a loss of 53% of effective venous return. Furthermore, the shielding function of the valves increased the perfusion in the relaxation phase. Finally, inclusion of the superficial venous system demonstrates the role of the superficial veins in maintaining arterial inflow during muscle contraction and decreasing refilling time by 37% during relaxation.

Chapter 3

Venous Valves

This chapter is based on: Global sensitivity analysis of a model for venous valve dynamics, **J.M.T. Keijsers**, C.A.D. Leguy, W. Huberts, A.J. Narracott, J. Rittweger and F.N. Vosse, *Journal of Biomechanics*, 2016.

ABSTRACT
Chronic venous disease is defined as dysfunction of the venous system caused by incompetent venous valves with or without a proximal venous obstruction. Assessing the severity of the disease is challenging, since venous function is determined by various interacting hemodynamic factors. Mathematical models can relate these factors using physical laws and can thereby aid understanding of venous (patho-)physiology. To eventually use a mathematical model to support clinical decision making, first the model sensitivity needs to be determined. Therefore, the aim of this study is to assess the sensitivity of the venous valve model outputs to the relevant input parameters. Using a 1D pulse wave propagation model of the tibial vein including a venous valve, valve dynamics under head up tilt are simulated. A variance-based sensitivity analysis is performed based on generalized polynomial chaos expansion. Taking a global approach, individual parameter importance on the valve dynamics as well as importance of their interactions is determined. For the output related to opening state of the valve, the opening/closing pressure drop ($dp_{\text{valve},0}$) is found to be the most important parameter. The venous radius ($r_{\text{vein},0}$) is related to venous filling volume and is consequently most important for the output describing venous filling time. Finally, it is concluded that improved assessment of $r_{\text{vein},0}$ and $dp_{\text{valve},0}$ is most rewarding when simulating valve dynamics, as this results in the largest reduction in output uncertainty. In practice, this could be achieved using ultrasound imaging of the veins and fluid structure interaction simulations to characterize detailed valve dynamics, respectively.

3.1 Introduction

Chronic venous disease is defined as dysfunction of the venous system caused by incompetent venous valves either with or without a proximal venous obstruction (international consensus committee on chronic venous disease (Porter et al., 1995)). As a result of venous valve incompetence, the muscle pump efficiency is significantly reduced, which has a negative effect on venous return, especially in upright position (Laughlin, 1987). Additionally, chronic venous disease results in increased venous pressure and blood accumulation in the leg (Bergan et al., 2006). Venous hypertension, in turn, may contribute to the development of varicose veins (affecting one third of the Western population (Evans et al., 1999)) and in the long term to skin changes including pigmentation, venous eczema and even venous ulcers (chronic venous insufficiency) (Eberhardt and Raffetto, 2005).

For diagnosis of chronic venous disease Doppler ultrasound or phlebography (venous X-ray with contrast-agents) are often used to assess the location of leaking valves and varicose veins (Coleridge-Smith et al., 2006; Eberhardt and Raffetto, 2005; Nicolaides, 2000). Although these methods can adequately detect local defects, they cannot determine the hemodynamic consequences of the disease, such as increased venous pressure and muscle pump inefficiency. Therefore, global measures such as venous pressure or venous calf volume (using air plethysmography (Criado et al., 1998; Eberhardt and Raffetto, 2005)) should be examined after calf muscle contractions or under head up tilt (i.e. going from supine to upright position without putting weight on the limb being measured). With these methods global diagnostic parameters, related to either venous refilling speed following tilt or ejection fraction after muscle contraction, can be assessed (Katz et al., 1991); e.g. venous filling index ($VFI = \frac{\Delta V}{\Delta t}\big|_{90\%\text{refilling}}$), which is measured after tilt. However, measuring venous pressure is invasive and air plethysmography is not available in every vascular laboratory.

An alternative approach to assess the global severity of chronic venous disease is the use of mathematical models based on physical laws and physiological mechanisms. These models can quantitatively predict hemodynamic parameters, that are important for the development of chronic venous disease and are difficult to measure. In the last decade, reduced order models of arterial hemodynamics have developed to a stage where they not only aid understanding cardiovascular (patho-)physiology (Boileau et al., 2015; Shi et al., 2011; van de Vosse and Stergiopulos, 2011), but are also being validated to support clinical decision making (Caroli et al., 2013; Marchandise et al., 2009). For the venous system relatively few reduced order models have been developed to examine hemodynamics (Müller and Toro, 2014; Mynard and Smolich, 2015), regulation (Simakov et al., 2013) and valve dynamics (Chapter 2), but these do include sufficient detail to capture generic venous function and the interplay be-

tween the various valves and veins. Although these models are suitable for assessment of the hemodynamic significance of chronic venous disease, they have not yet been applied in this context. Most models used to represent venous valve dynamics are generally only able to represent the open and closed state (diode) (Fullana and Zaleski, 2008; Müller and Toro, 2014; Zervides et al., 2008), whereas reduced order heart valve models provide more detail (Werner et al., 2002; Zacek and Krause, 1996). More sophisticated reduced-order valve models have been developed by Korakianitis and Shi (2006), who included valve leaflet motion based on a force balance and Mynard et al. (2012), who related valve opening state to the pressure drop over the valve. The latter model was extended by Pant et al. (2015) to include valve regurgitation due to valve prolapse. These versatile valve models are also preferred for the venous system as they can model regurgitation in leaking valves and allow more detailed studies of venous valve dynamics, such as capturing venous valve dynamics under head up tilt. Unfortunately, these models require the introduction of more model parameters, which may increase the resulting uncertainty of the model output.

To eventually use such models to support clinical decision making, it is essential to assess the influence of the input parameters on the model output, which can be addressed through a sensitivity analysis. Using a global method both the importance of individual parameters and their interactions can be assessed (Eck et al., 2016). Furthermore, knowing which parameters are most important, allows for refinement of clinical measurement protocols when using these models to support clinical decision making. Additionally, parameters that are difficult to measure can be assessed by using fluid structure interaction simulations.

The aim of this study is to investigate the sensitivity of a mathematical model of a tibial vein simulating venous valve dynamics under head up tilt. Our previously presented venous model (Chapter2) is extended with the versatile valve model of Mynard et al. (2012). The influence of venous filling and valve input parameters on the valve dynamics in a healthy subject is assessed via a sensitivity analysis based on generalized polynomial chaos expansion (gPCE). Finally, it is investigated whether more detailed fluid structure interaction simulations are necessary to inform the reduced order model.

3.2 Methods

To examine the dynamics of a healthy venous valve under head up tilt, a pulse wave propagation model of a vein including a single valve was developed (Figure 3.1). The pulse wave propagation model enables a continuous distribution of gravity, allows an easy extension of the model configuration to a larger domain and includes

non-linear effects.

3.2.1 Model

The governing model equations are described in this section. This includes the 1D venous pulse wave propagation model, the 0D venous valve model and the boundary conditions. The baseline values of the model parameters can be found in Table 3.1.

Table 3.1: Model parameters: Baseline value and description are given. Furthermore, for the parameter included in the sensitivity analysis, the uncertainty range is given in the last column.

Symbol	Value	Unit	Description	Range
l_{dist}	10	cm	Length distal part 1D vein	-
l_{prox}	20	cm	Length proximal part 1D vein	-
p_{ex}	0	Pa	Extravascular pressure	
g	9.81	m s^{-2}	Gravitational acceleration on earth	-
$A_{\text{eff,min}}$	$1 \cdot 10^{-20}$	m^2	Minimal effective cross-sectional area	-
α_{rot}	$0 - \pi/2$	rad	Tilting angle (supine to upright)	-
p_0	0	Pa	Extravascular pressure in windkessel element	-
$p_{\text{wk,in}}$	12.0	kPa	Constant inlet pressure	-
$p_{\text{wk,out}}$	700	Pa	Constant outlet pressure	-
η	$4.5 \cdot 10^{-3}$	Pa	Dynamic blood viscosity: Typical viscosity used in 1D hemodynamics models is taken as a reference with an uncertainty of 20% (Boileau et al., 2015).	$[3.6, 5.4] \cdot 10^{-3}$
β_l	1.0	-	Effective length venous valve ratio ($\beta_l = \frac{l_{\text{eff}}}{r_{\text{vein,0}}}$): Ratio of the effective length of the venous valve relative to the radius of the connecting vein (Mynard and Smolich, 2015)	$[0.5, 2.0]$
ρ	1050	kg/m^3	The arterial blood density has a value between the 1045 and 1055 kg/m^3 and venous blood density is on average 0.1 kg/m^3 less than arterial blood density (Kenner, 1989).	$[1040, 1060]$
β_A	0.65	-	Effective valve cross-sectional area ratio $\beta_A = \frac{A_{\text{eff,max}}}{A_{\text{vein,0}}}$: Ratio of valve cross-sectional area to the cross-sectional area of the connecting vein. The valve is observed to create a stenosis in the fully open state (Lurie et al., 2003; McCaughan et al., 1984).	$[0.4, 1.0]$
K_{vo}	0.3	$\text{Pa}^{-1}\,\text{s}^{-1}$	Valve opening constant: The full range of values reported by Mynard and Smolich (2015) is covered.	$[0.2, 0.4]$

Table 3.1 – continued from previous page

Symbol	Value	Unit	Description	Range
K_{vc}	0.3	$\text{Pa}^{-1}\,\text{s}^{-1}$	Valve closing constant: The full range of values reported by Mynard and Smolich (2015) is covered.	$[0.2, 0.4]$
$dp_{\text{valve},0}$	0	Pa	Opening/closing pressure drop over the valve ($dp_{\text{valve},0} = p_{\text{dist}} - p_{\text{prox}}$) (Figure 3.2C): Pressure drop over the valve above and below which valve opening and closing are initiated, respectively. This pressure drop is assumed to be close to zero (Mynard et al., 2012).	$[-10, 10]$
q_{bl}	0.45	mL/s	Baseline flow: The flow is defined to represent the flow in the tibial vein with an uncertainty of 10% (Saltin et al., 1998).	$[0.405, 0.495]$
K_p	425	Pa	Venous bending stiffness: The bending stiffness is defined to represent the mechanical characteristics of the tibial vein with an uncertainty of 20% (Müller and Toro, 2014).	$[340, 510]$
$r_{\text{vein},0}$	1.50	mm	Radius of the 1D vein: The radius is defined as the radius of the tibial vein with an uncertainty of 20% (Müller and Toro, 2014).	$[1.20, 1.80]$
τ_{RC}	2.0	s	Time constant defining the decay of the pressure wave in diastole: Most of the compliance is included in the WK-element (Westerhof and Elzinga, 1991). Uncertainty is set to 20%.	$[1.6, 2.4]$

1D Venous pulse wave propagation

The hemodynamics in the large veins are captured using the one-dimensional equations for mass and momentum balance. In this formulation, blood is assumed to be an incompressible, Newtonian fluid. This gives:

$$C\frac{\partial p_{tr}}{\partial t} + \frac{\partial q}{\partial z} = 0, \tag{3.1}$$

$$\frac{\partial q}{\partial t} + \frac{\partial A\overline{v_z^2}}{\partial z} + \frac{A}{\rho}\frac{\partial p}{\partial z} = \frac{2\pi a}{\rho}\tau_w + Ag_z, \tag{3.2}$$

where C, compliance per unit length, is a function of transmural pressure $p_{\text{tr}} = p - p_{\text{ex}}$, where p and p_{ex} are the intra- and extravascular pressure respectively, q is flow, t is time and z is the axial coordinate. Furthermore, A is the cross-sectional area, $\overline{v}_z$ is the mean velocity in the axial direction, ρ is the blood density, $a = \sqrt{A/\pi}$ is the equivalent radius for equal area, τ_w is the wall shear stress and $g_z = g\,\mathbf{e_g}\cdot\mathbf{e_z}$ is the contribution of gravitational acceleration in the axial direction. Additionally, g is the gravitational acceleration on earth, $\mathbf{e_g}$ is the unit vector in the direction of gravity

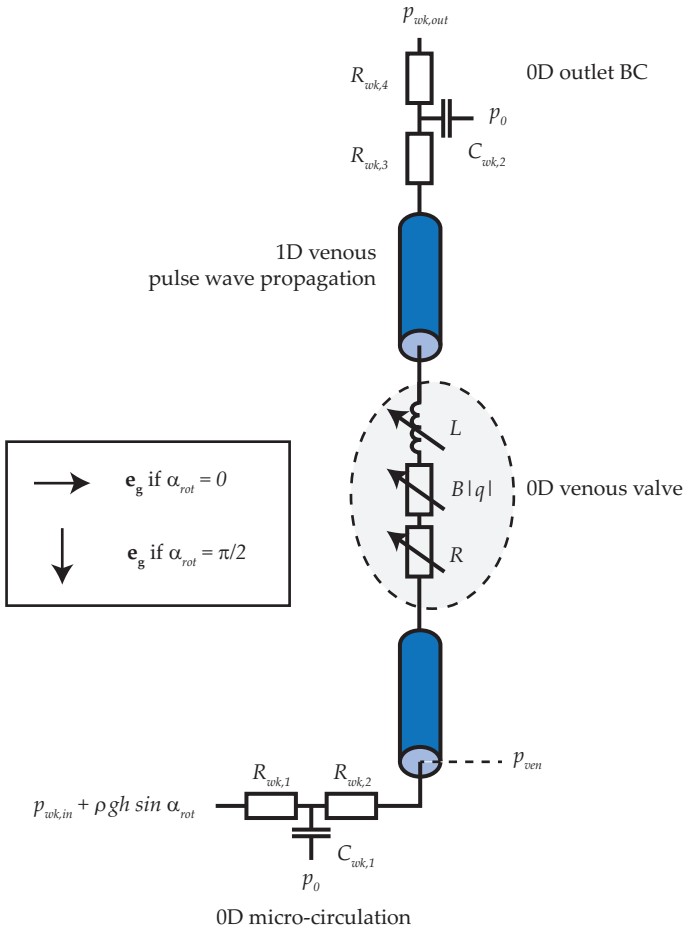

Figure 3.1: Model configuration consisting of a 0D venous valve, 1D venous pulse wave propagation elements, a 0D micro-circulation and a 0D outlet boundary condition (BC). Furthermore, the gravity vector $\mathbf{e_g}$ is shown together with the rotation angle in both supine and tilted position. The 1D vein is split into a distal ($l_{\text{dist}} = 10\ cm$) and a proximal ($l_{\text{prox}} = 20\ cm$) part by a 0D valve (zero length). p_{ven} indicates the location of distal venous pressure as reported in the Results Section in Figure 3.3E.

and $\mathbf{e_z}$ is the unit vector in the axial direction along the vessel.

To obtain an estimate of the wall shear stress τ_w and the advection term $\frac{\partial A\overline{v_z^2}}{\partial z}$ the approximate velocity profile of Bessems et al. (2007) is used. The pressure gradient and gravitational forces are assumed to be in balance with viscous forces in the unsteady boundary layer (Stokes layer) close to the vessel wall, whereas inertia forces are assumed to dominate in the central core (for a detailed description see Bessems et al. (2007)).

To describe venous collapse under low transmural pressure, due to e.g. increasing extravascular pressure or gravitational stress, the non-linear constitutive law of Shapiro (1977) is approximated with a fit as derived in Chapter 2.2.3 (Figure 2.3). The venous compliance per unit length C is calculated as the derivative of the cross-sectional area to the transmural pressure.

0D Venous valve

The pressure-flow relation of a dynamic venous valve is included through a fully lumped model (i.e. the valve element has no length and spatial parameters are only included for dimensionality) as described by Mynard et al. (2012). Additionally, the viscous losses are included in the pressure flow relation

$$\Delta p = Rq + Bq|q| + L\frac{\partial q}{\partial t}, \tag{3.3}$$

where Rq represent the viscous losses, $Bq|q|$ the losses related to the convective acceleration and dynamic pressure, and $L\frac{\partial q}{\partial t}$ the unsteady inertia losses. The associated Poisseuille resistance R, Bernouilli resistance B and inertia L are defined by:

$$R = \frac{8\pi\eta l_{\text{eff}}}{A_{\text{eff}}^2}, \qquad B = \frac{\rho}{2A_{\text{eff}}^2} \qquad \text{and} \qquad L = \frac{\rho l_{\text{eff}}}{A_{\text{eff}}}, \tag{3.4}$$

where A_{eff} is the effective cross-sectional area, ρ is the blood density and $l_{\text{eff}} = \beta_l r_{\text{vein,0}}$ is the effective valve length expressed as a multiple β_l of the reference radius of the connecting vein $r_{\text{vein,0}}$. To represent different states of the valve opening the effective cross-sectional area is defined as a function of valve state ζ via the following relation

$$A_{\text{eff}} = (A_{\text{eff,max}} - A_{\text{eff,min}})\,\zeta + A_{\text{eff,min}}, \tag{3.5}$$

where $A_{\text{eff,min}}$ and $A_{\text{eff,max}}$ are the minimal and maximal valve effective cross-sectional area respectively ($A_{\text{eff,max}} >> A_{\text{eff,min}}$). $A_{\text{eff,max}} = \beta_A A_{\text{vein,0}}$ is expressed as a multiple β_A of the reference cross-sectional area of the connecting vein $A_{\text{vein,0}}$. To model a dynamic valve, the valve state is defined to vary between zero and one (closed: $\zeta = 0$, open: $\zeta = 1$). The value of ζ is determined by the differential equations for

valve opening and closing respectively

$$\frac{d\zeta}{dt} = \begin{cases} (1-\zeta)\, K_{\text{vo}}\, (\Delta p - dp_{\text{valve,0}})\,, & \text{for } \Delta p > dp_{\text{valve,0}} \\ \zeta K_{\text{vc}}\, (\Delta p - dp_{\text{valve,0}})\,, & \text{for } \Delta p < dp_{\text{valve,0}} \end{cases}, \tag{3.6}$$

where K_{vo} and K_{vc} are parameters determining the opening and closing speed of the valves. Furthermore, $dp_{\text{valve,0}}$ is the pressure gradient above and below which opening and closing is initiated respectively.

Boundary conditions

Both the inlet and outlet of the modeled vein are connected to a three-element windkessel model, representing the micro-circulation at the inlet and included to reduce reflections at the outlet (Figure 3.1). Each windkessel model consists of two resistances $R_{wk,i}$ $(i = 1, 2, 3, 4)$ in series and one volume compliance $C_{wk,j}$ $(j = 1, 2)$ connected to a constant extravascular pressure p_0

$$\Delta p_R = R_{wk,i} q \qquad \text{and} \qquad \frac{\partial p_{tr}}{\partial t} = \frac{1}{C_{wk}} q. \tag{3.7}$$

For the windkessel element at the inlet the second resistance is defined to match the characteristic impedance Z_{vein} of the connecting 1D vein

$$R_{\text{wk,1}} = Z_{\text{vein}} = \sqrt{\frac{\rho}{A_{\text{vein,0}} C_{\text{vein,0}}}}. \tag{3.8}$$

The first resistance is related to the total windkessel resistance $R_{\text{wk,tot}}$, which is set to match the baseline flow q_{bl}

$$R_{\text{wk,tot}} = R_{\text{wk,1}} + R_{\text{wk,2}} = \frac{\Delta p}{q_{\text{bl}}}, \tag{3.9}$$

where Δp is the gradient between inlet pressure $p_{\text{wk,in}}$ and the distal venous pressure under supine baseline conditions. The latter is derived as the outlet pressure p_{out} plus the baseline flow q_{bl} times the resistance of the 1D vein and outlet windkessel element. Next, the compliance is derived from a time constant τ_{RC}

$$C_{\text{wk,1}} = \frac{\tau_{\text{RC}}}{R_{\text{wk,2}}}. \tag{3.10}$$

For the windkessel element at the outlet, both resistances are defined to be equal to the characteristic impedance Z_{vein} of the connecting vein

$$R_{\text{wk,3}} = R_{\text{wk,4}} = Z_{\text{vein}} = \sqrt{\frac{\rho}{A_{\text{vein,0}} C_{\text{vein,0}}}}. \tag{3.11}$$

The outlet compliance $C_{\text{wk,2}}$ is derived from the time constant τ_{RC} using Equation 3.10.

In the current model pressure is prescribed as a boundary condition and flow is only indirectly prescribed by defining the resistance of the micro-circulation. The outlet pressure p_{out} is defined to have a constant value and the inlet pressure is defined as p_{in} a constant value plus the hydrostatic column of the 1D part.

$$p_{\text{in}} = p_{\text{wk,in}} + \rho g h \sin \alpha_{\text{rot}} \qquad \text{and} \qquad p_{\text{out}} = p_{\text{wk,out}}, \tag{3.12}$$

where $p_{\text{wk,in}}$ is the average arterial pressure, h is the total length of the 1D vein, α_{rot} is the rotation angle determining the posture and $p_{\text{wk,out}}$ is a constant pressure at the outlet.

Numerical implementation

The equations detailed above were implemented in the finite element package SEPRAN (Ingenieursbureau SEPRA, Leidschendam, the Netherlands) based on the computational method described by Kroon et al. (2012). Spatial discretization was implemented using the trapezium rule with element size $dz = 10$ mm. Time discretization was performed using the second-order backward difference scheme with timestep $dt = 10$ ms. Both dz and dt were chosen such that the numerical solution was independent of the selected values and still computationally efficient. Further pre- and postprocessing was done using MATLAB R2012b (MathWorks, Natick, MA, USA).

3.2.2 Head up tilt simulation

A head up tilt was simulated to study the opening and closing of the valve under gravitational stress. To simulate a smooth head up tilt from supine ($\alpha_{\text{rot}} = 0$) to upright ($\alpha_{\text{rot}} = \frac{\pi}{2}$) the tilt angle α_{rot} was defined with the following relation (Figure 3.3A):

$$\alpha_{\text{rot}} = \begin{cases} 0, & \text{if } t < t_0 \\ \frac{\pi}{4}\left(1 - \cos(\pi(t - t_0)/\tau_{\text{rot}})\right), & \text{if } t_0 < t < t_0 + \tau_{\text{rot}} \\ \frac{\pi}{2}, & \text{if } t > t_0 + \tau_{\text{rot}}. \end{cases} \tag{3.13}$$

where t_0 is the time at which the tilt starts and τ_{rot} is the time over which the tilt is applied. The latter is set to 2.5 s to correspond with *in vivo* experiments (Jellema et al., 1999).

3.2.3 Sensitivity analysis

To determine the importance of the model parameters, first the output variance resulting from the input uncertainty was quantified. Using a sensitivity analysis, the

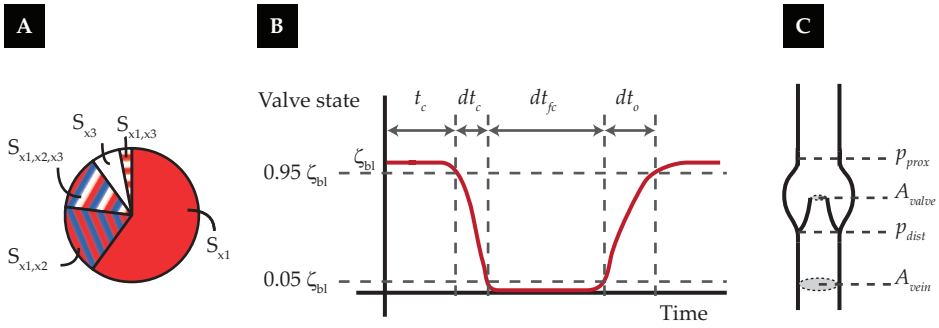

Figure 3.2: Sensitivity analysis: **A** Schematic visualisation of the distribution of the output variance over the input parameters: x_1, x_2 and x_3. S_i = main index, S_{ij} = second order effect, S_{ijk} = third order effect. **B** Output parameters of interest schematically visualized in a plot of the valve state ζ over time. **C** Parameters related to the input parameters used in the sensitivity analysis, visualized in a segment of a vein including a valve.

total variance of each output was then allocated to the individual parameters and their interactions, as schematically visualized in Figure 3.2A. The influence of an individual parameter is captured by the main sensitivity index S_i, and can be interpreted as the reduction in output variance if this input parameter would have been set to its true value. Higher order effects (S_{ij}, S_{ijk}, ...) include the contribution between interactions of two or more input parameters (Eck et al., 2016).

Output of interest

The following parameters, which describe valve dynamics, are defined as output of interest (Figure 3.2B):

- ζ_{bl}, baseline valve state (not necessarily equal to 1.0).
- t_{c}, time point valve closure starts: the first time point after tilt when the valve state decreases below $0.95\zeta_{\text{bl}}$.
- dt_{c}, valve closing time: the time taken to go from 0.95 to $0.05\zeta_{\text{bl}}$.
- dt_{fc}, valve fully closed time: the interval between the time the valve state first decreases below $0.05\zeta_{\text{bl}}$ until it increases above $0.05\zeta_{\text{bl}}$.
- dt_{o}, valve opening time: the time taken to go from 0.05 to $0.95\zeta_{\text{bl}}$.

General polynomial chaos expansion

To derive the total variance and the sensitivity indices in a computationally efficient manner, the generalized polynomial chaos expansion (gPCE-R) method is used (Huberts et al., 2014). This includes the derivation of a meta-model consisting of orthogonal polynomials with output-specific coefficients, which are obtained by a least-squares regression (-R). The sensitivity indices can be derived from the meta-model analytically. To obtain a good regression for the chosen meta-model, the model must be evaluated a sufficient number of times. In this study, the meta-model consists of orthogonal polynomials up to the fourth order and 2730 model evaluations ($CPU \approx 15$ h) are used for regression.

Input parameters

The sensitivity of the model with regard to the valve dynamics is examined under variation of the 11 input parameters related to venous valve dynamics and venous refilling. These parameters are listed in Table 3.1, which provides the baseline value and the range used for the sensitivity analysis.

3.3 Results

3.3.1 Venous valve dynamics

The valve dynamics and venous hemodynamics were examined while simulating a head up tilt (Figure 3.3A) in a 1D venous model with a single 0D valve. With all input parameters fixed at their baseline value, the resulting valve state ζ, valve pressure drop Δp_{valve}, valve flow q_{valve}, venous pressure and total volume are shown in Figure 3.3B, C, D, E and F respectively. Shortly after tilt is initiated, the valve flow decreases (Figure 3.3D) and the valve closes (Figure 3.3B). This is followed by a decrease in pressure difference across the valve (Figure 3.3C). The venous pressure and total volume increase linearly ($VFI = \frac{\Delta V}{\Delta t}\big|_{90\%\text{ refilling}} = 0.5$ mL/s Figure 3.3E and F respectively) until the pressure drop over the valve approaches zero, the valve starts to open and the flow increases again at $t \approx 15.7$ s (Figure 3.3C, B and D respectively).

3.3.2 Convergence analysis

To assess the quality of the metamodel the descriptive error ϵ_{R^2}, a measure for the residual variance as a fraction of total variance and based on the coefficient of determination R^2, and the predictive error ϵ_{Q^2}, a measure for the predicted residual variance as a fraction of total variance and based on the validation coefficient Q^2,

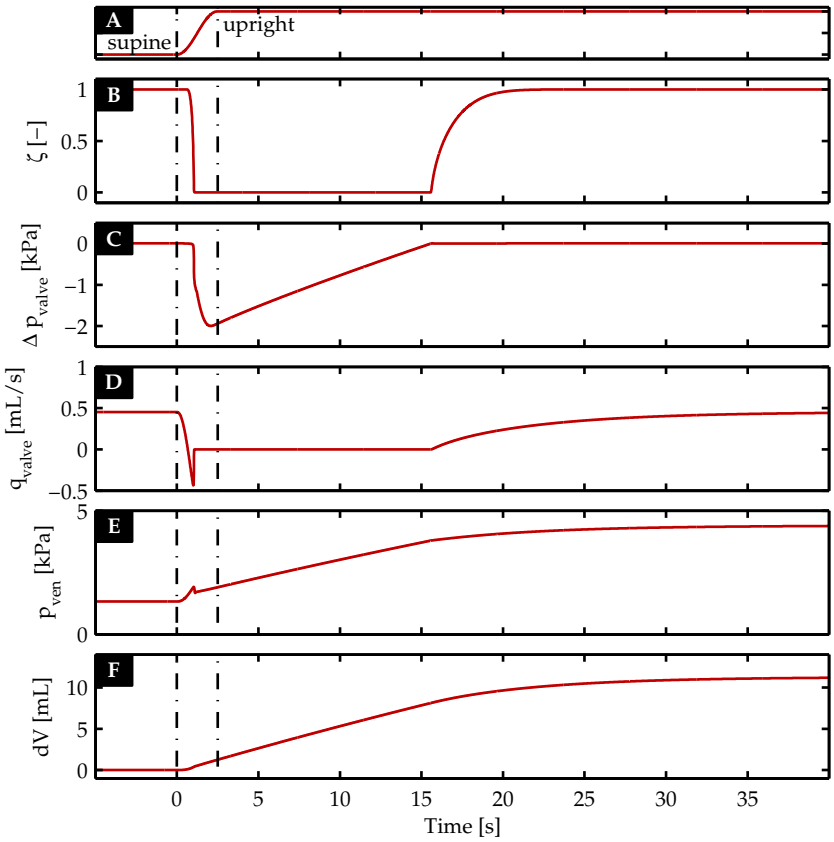

Figure 3.3: Valve dynamics and hemodynamics under head up tilt for baseline input parameters (Table 3.1 - Input parameters). In plot **A** the time course of the tilt is shown. The beginning and end of the tilt are indicated with a dashed line in each plot. Plot **B**, **C** and **D** show the state ζ, pressure drop Δp_{valve} and flow q_{valve} of the valve respectively. Distal venous pressure p_{ven} (as indicated in Figure 3.1) and change in total volume (the sum of the 0D micro-circulation and the 1D vein) are shown in plot **E** and **F** respectively.

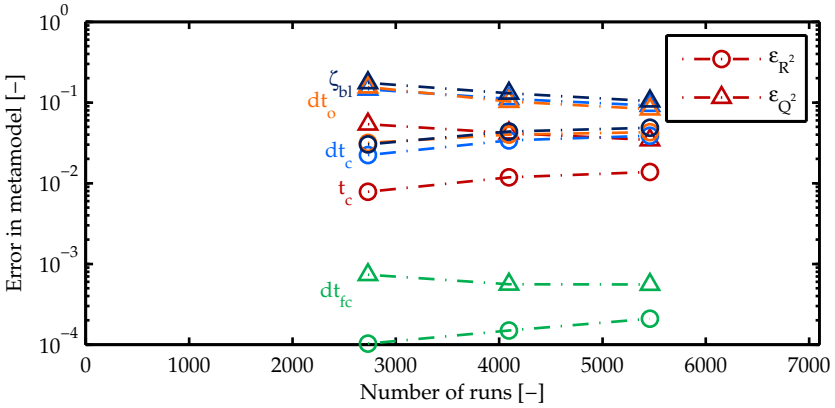

Figure 3.4: The quality of the metamodel for each output parameter. The descriptive error ϵ_{R^2} (o) and the predictive error ϵ_{Q^2} ($\triangle$) are plotted for increasing number of simulations. The colors represent the different output parameters: t_c, dt_c, dt_fc, dt_o and ζ_bl.

were calculated for an increasing number of simulations (Donders et al., 2015) (o and $\triangle$ in Figure 3.4 respectively). The different output parameters are depicted with different colors. Both the descriptive and predictive errors remain stable for increasing number of simulations.

3.3.3 Sensitivity analysis

The contribution of the valve and refilling related input parameters to the variance in valve timings was assessed using a sensitivity analysis. The resulting main (S_i) and interaction (S_{ij}, S_{ijk}, S_{ijkl}) sensitivity indices are presented in pie charts in Figure 3.5. The input parameters which, individually or while interacting with other parameters, contribute more than 1% to the output variance are presented with their corresponding color, whereas the sum of the remaining sensitivity indices is shown as the gray area. The values of the sensitivity indices presented in Figure 3.5 are summarized in Table 3.2. For t_c, dt_c, dt_o and to a lesser extent ζ_bl the pressure drop for valve opening and closing $dp_\mathrm{valve,0}$ is the input parameter which contributes the most to the output variance (in Figure 3.5A,B,D and E respectively). The venous radius $r_\mathrm{vein,0}$ is the most important parameter for the variance of dt_fc (Figure 3.5C). The interaction of various parameters contributes to the variance of t_c, dt_c, dt_o and especially ζ_bl (Figure 3.5B). The interactions of $dp_\mathrm{valve,0}$ with β_A and/or $r_\mathrm{vein,0}$ are shown to be important for ζ_bl (Figure 3.5E).

The average values of the output parameters plus their standard deviations are shown in Figure 3.6 depicting the absolute and relative values in plot A and B, re-

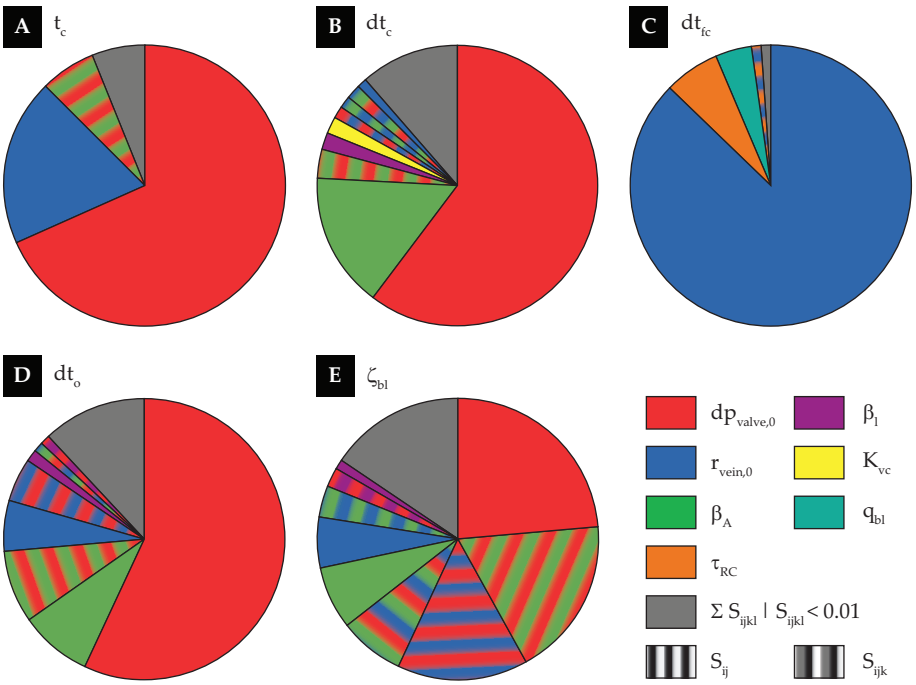

Figure 3.5: Contribution of the input parameters to the variance in the output parameters: **A** t_c, **B** dt_c, **C** dt_{fc}, **D** dt_o and **E** ζ_{bl}. The colors represent the various input parameters contributing more than one percent to the output variance. Second and third order interactions (S_{ij} and S_{ijk}) are presented with a combination of the colors. The gray area represents the sum of the sensitivity indices which individually contribute less than one percent. The size of the sensitivity index decreases clockwise starting at noon position. The values of the sensitivity indices can be found in Table 3.2.

Table 3.2: Contribution of the input parameters to the variance in the output parameters: t_c, dt_c, dt_{fc}, dt_o and ζ_{bl}. Only the sensitivity indices that contribute more than one percent are reported in the table. Coloring corresponds to the coloring used for the pie-charts in Figure 3.5

	t_c	dt_c	dt_{fc}	dt_o	ζ_{bl}
$dp_{valve,0}$ (■)	0.683	0.601	< 0.01	0.572	0.237
$r_{vein,0}$ (■)	0.194	0.012	0.874	0.058	0.060
β_A (■)	< 0.01	0.154	< 0.01	0.084	0.072
τ_{RC} (■)	< 0.01	< 0.01	0.063	< 0.01	< 0.01
β_l (■)	< 0.01	0.020	< 0.01	0.013	0.0011
K_{vc} (■)	< 0.01	0.018	< 0.01	< 0.01	< 0.01
q_{bl} (■)	< 0.01	< 0.01	0.044	< 0.01	< 0.01
$dp_{valve,0}$, $r_{vein,0}$ (■■)	< 0.01	0.015	< 0.01	0.051	0.150
$dp_{valve,0}$, β_A (■■)	0.063	0.039	< 0.01	0.082	0.183
$dp_{valve,0}$, β_l (■■)	< 0.01	< 0.01	< 0.01	0.012	0.023
$r_{vein,0}$, β_A (■■)	< 0.01	0.015	< 0.01	< 0.01	0.035
$r_{vein,0}$, τ_{RC} (■■)	< 0.01	< 0.01	0.011	< 0.01	< 0.01
$dp_{valve,0}$, $r_{vein,0}$, β_A (■■■)	< 0.01	0.015	< 0.01	0.012	0.075
rest (■)	0.060	0.112	0.008	0.118	0.154

spectively. Here, the relative value is calculated using: $y_{rel} = \frac{y_i - y_{mean}}{y_{mean}}$. A large standard deviation is found for dt_{fc} and dt_o. Although the absolute standard deviation is small, the relative standard deviation is large for t_c and dt_c.

The relation between the input parameters with the highest main sensitivity index ($dp_{valve,0}$ and $r_{vein,0}$) and the output parameters is presented in Figure 3.7. The output and input parameters are shown by row and column respectively. Furthermore, the gray scale is related to the magnitude of the main sensitivity index S_i (see colorbar). The time of closing t_c decreases with an increasing pressure drop for valve opening and closing $dp_{valve,0}$ (Figure 3.7A), whereas the time needed for the valve to open and close increases with $dp_{valve,0}$ (Figure 3.7C,G). The $r_{vein,0}$ parameter shows a strong linear relation with dt_{fc} (99% of S_i is attributed to the first order polynomial) (Figure 3.7F). The remaining plots (Figure 3.7B, D, E, H, I and J) show a lower correlation and have a lower sensitivity index.

3.4 Discussion

In this study the venous valve dynamics in a healthy subject under head up tilt was investigated using a mathematical model of a single vein geometry including a single versatile valve. To assess the influence of the various filling and valve input parameters on valve dynamics, a sensitivity analysis was performed.

A head up tilt was simulated by rotating a single vein relative to the gravity vector

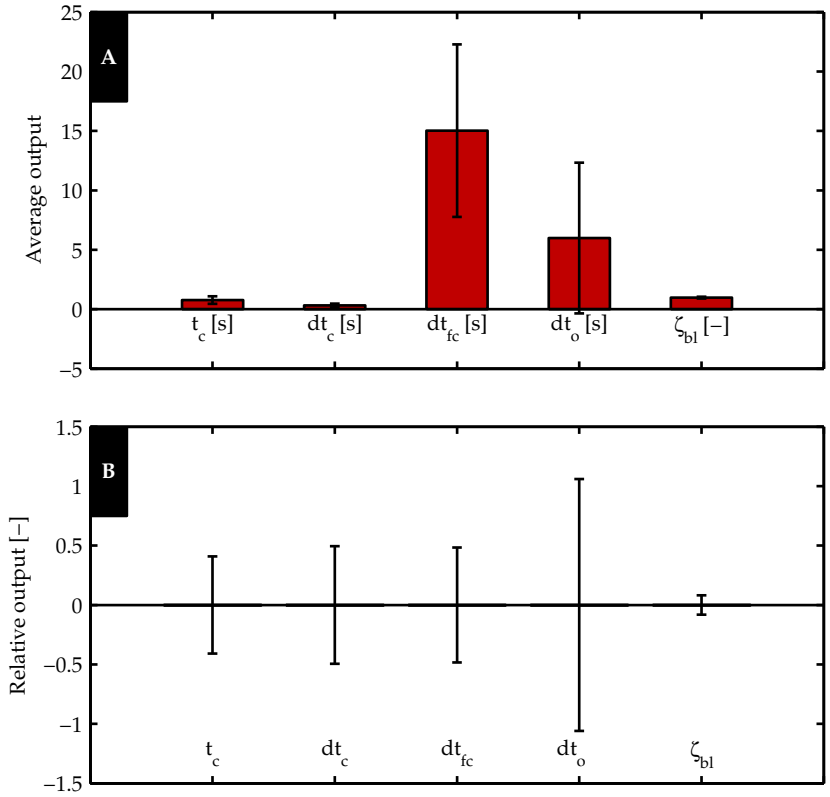

Figure 3.6: Average and standard deviation of the output parameters: **A** absolute and **B** relative value.

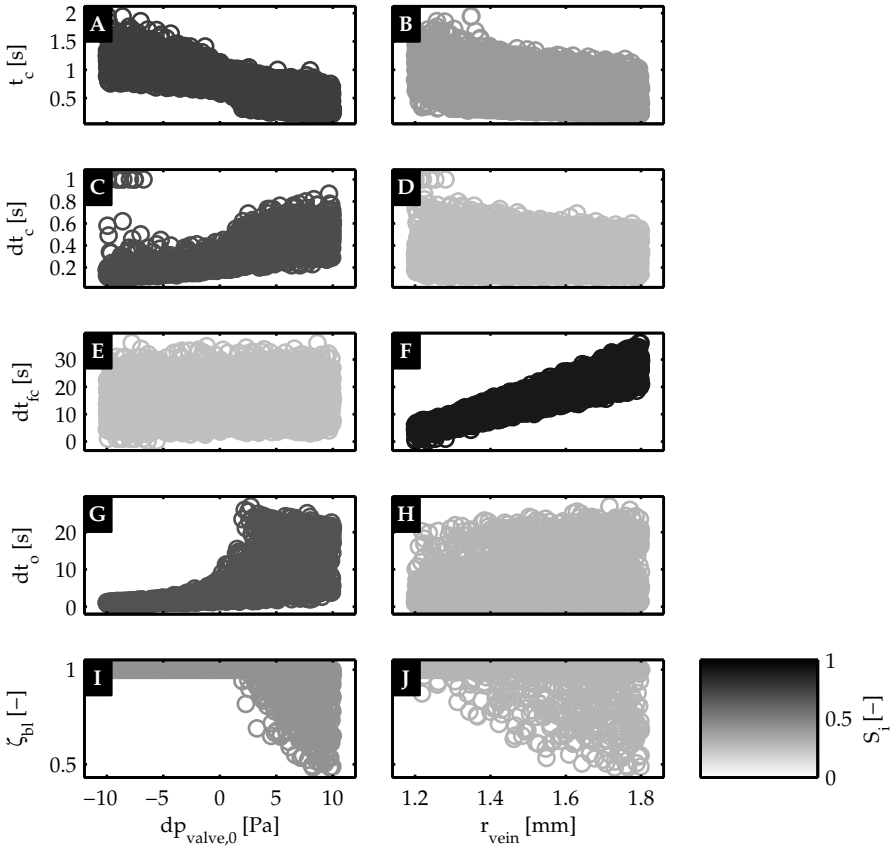

Figure 3.7: The relation between the two dominating input parameters ($dp_{\text{valve},0}$ (left) and $r_{\text{vein},0}$ (right)) and all the output parameters is presented with scatter plots, where each circle represents a single simulation. The output parameters are shown by row and the input parameters by column; the first row presents the relation between output t_{c} and input $dp_{\text{valve},0}$ on the left (**A**), and input $r_{\text{vein},0}$ on the right (**B**). The rest of the output parameters are presented similarly in the subsequent rows. The gray scale represents the main sensitivity index S_i, with darker gray for the higher values as indicated with the colorbar. The values of the main sensitivity indices can be found in the first two rows of Table 3.2.

(using baseline parameters). Shortly after tilt initiates, a decrease in valve flow was observed and even some backflow for 0.4 s. This corresponds to the non-pathological range ($dt_{\text{reflux}} < 0.5$ s) according to the definition of venous reflux in the deep calf veins by Labropoulos et al. (2003). Once tilting was initiated the vein and microcirculation started to fill to approach the hydrostatic pressure. The observed linear-plateau pressure and volume pattern is in accordance with *in vivo* measurements after muscle contractions (Nicolaides and Zukowski, 1986), where the veins are also refilled. As only a small part of the vasculature is included the hydrostatic pressure is smaller than the 12 kPa measured *in vivo*, but does match the physically expected $\rho g h = 3.1$ kPa. This small increase in venous pressure (from 1.3 to 4.4 kPa) induces only a small increase in 1D volume (1.3% of total) (see Figure 2.3). Venous filling index (VFI), a measure of venous filling speed, is equal to 0.5 mL/s, which is in the region of VFI for healthy subjects ($VFI < 2.0\ mL/s$) (Eberhardt and Raffetto, 2005). In short, this implies that the observed pressure and volume pattern and derived global hemodynamics parameters are in accordance with the literature.

The sensitivity analysis showed that $dp_{\text{valve,0}}$, $r_{\text{vein,0}}$ and β_A are the most influential parameters with more than 80% of the variance of all output parameters arising from the sum of the individual and interactive contributions of these three parameters, i.e. $S_i + S_{ij} + S_{ijk}$. The valve opening pressure $dp_{\text{valve,0}}$ is closely related to the opening and closing of the valve and therefore the observed importance of this parameter on output parameters related to valve state (t_{c}, dt_{c}, dt_{o} and ζ_{bl}) is also expected. The venous reference radius $r_{\text{vein,0}}$ is related to venous filling volume and is consequently the most important parameter for the output describing venous filling time dt_{fc}. Finally, β_A is related to the valve resistance in the open state and is therefore important for the valve dynamic output parameters (dt_{c}, dt_{o} and ζ_{bl}). All other parameters only have a minor contribution to the output variance and can therefore be fixed within their uncertainty range. In order to use the model for clinical decision making, the output variance should be decreased. For this, ultrasound could be used to assess β_A (Lurie et al., 2003) and $r_{\text{vein,0}}$ (Moneta et al., 1988) and further research using fluid-structure interaction simulations could decrease the uncertainty range of $dp_{\text{valve,0}}$ (Narracott et al., 2015). Improved assessment of $r_{\text{vein,0}}$ and $dp_{\text{valve,0}}$ would be most rewarding as the standard deviation of dt_{fc} and dt_{o} respectively is the largest. When the output parameters are considered in the context of chronic venous disease estimates of $r_{\text{vein,0}}$ should be improved as dt_{fc} provides a metric of venous filling time, which is related to venous function.

The sensitivity indices were derived using the generalized polynomial chaos expansion method. The quality of the metamodel was assessed by the descriptive and predictive error (Donders et al., 2015). While deriving the metamodel for an increasing number of simulations, a slight increase in the descriptive error of the model (ϵ_{R^2}),

and an increase in predictive power (decrease in ϵ_{Q^2}) was found. The convergence analysis demonstrated that only 5% of the output variance could not be captured by the metamodel (ϵ_{R^2} in Figure 3.4). Thereby, showing that the gPCE methods provides significant accuracy for this application.

The current paper describes the feasibility of applying the versatile valve model and the venous 1D pulse wave propagation model in supporting diagnosis of chronic venous disease. Further development should allow for modeling of pathological valve regurgitation, which Mynard et al. (2012) suggested to implement by an increase in minimal cross-sectional area A_{min} resulting in a valve model that remains partially open. Valve prolapse could be included by defining a negative valve state, as suggested by Pant et al. (2015). Furthermore, as chronic venous disease affects the global function of the venous calf circulation, the full venous calf geometry should be incorporated to include interactions between the many valves and the complex venous anatomy, which is possible using the 1D pulse wave propagation model as proposed in Chapter 2. Additionally, as venous refilling is achieved when the full hydrostatic pressure is established, the proximal veins returning to the heart should also be included. A full circulation model would also allow examination of the influence of venous pulsatility, originating from the thorax and abdomen, on the venous valves. Finally, the model should be validated with fluid-structure interaction simulations or *in vivo* measured hemodynamics parameters such as the venous filling index after tilt or ejection fraction after muscle contraction (Criado et al., 1998; Eberhardt and Raffetto, 2005).

3.5 Conclusion

A venous 1D pulse wave propagation model including a versatile valve model is presented and a sensitivity analysis has been performed on the model while capturing venous valve dynamics in a healthy subject under head up tilt. It has been shown that venous radius $r_{\text{vein},0}$ and valve opening/closing pressure $dp_{\text{valve},0}$ are the dominant parameters, which determine the variance in valve dynamics. Decreasing the uncertainty in these parameters to improve the model output accuracy could be achieved by improving clinical assessment via ultrasound or informed by more detailed mathematical models using fluid structure interaction. This would support eventual implementation of the model in clinical practice to aid clinical decision making.

Chapter 4

Regulation of vascular tone

A manuscript based on this chapter is being prepared.

ABSTRACT

At the onset of exercise blood flow to the muscle tissue increases to match to the oxygen demand. The increase in blood flow is regulated by the changes in perfusion pressure and peripheral resistance, due to the muscle pump effect and regulation of vascular tone respectively. However, the importance and individual functioning of both mechanisms remains unclear. Whereas, in a previous study we investigated the muscle pump effect in detail, the aim of this study is to examine the regulation of vascular tone and determine the importance of the myogenic, metabolic and baroreflex regulation during the different phases of muscle contraction. Therefore, our mathematical model of the calf circulation was extended with a regulation model to simulate changes in vascular tone depending on myogenic, metabolic and baroreflex regulation. After successfully fitting the myogenic and metabolic gain to match the *in vivo* flow response in the supine position, a good prediction of the flow in the tilted position was found. Firstly, it could be concluded that the metabolic activation caused the flow increase shortly after muscle contraction. Secondly, the change in baseline flow was a result of myogenic and baroreflex activation. Using a two-step sensitivity analysis (Morris screening plus a subsequent polynomial chaos expansion), the myogenic gain was identified as most important parameter for the variance in the flow increase after muscle contraction. Finally, the four most important parameters, identified by the sensitivity analysis, were varied randomly. This still resulted in a good fit of the *in vivo* response.

4.1 Introduction

At the onset of exercise, the blood flow within muscle in the lower limb increases significantly to meet the metabolic demand for oxygen and remove waste products. The amount of muscle blood flow depends on the arterio-venous pressure drop and the peripheral resistance. In the lower limb in particular, the arterio-venous pressure drop and the peripheral resistance are influenced by mechanical effects during a muscle contraction and relaxation (the muscle pump effect) and the vasodilatory state of the arterioles respectively. However, the exact contribution of these two mechanisms to the blood flow increment at the onset of exercise is still a matter of debate (Tschakovsky and Sheriff, 2004). Three hypotheses are currently described in literature: the first states that flow augmentation is primarily caused by the muscle pump effect, the second claims that regulation of peripheral resistance is the major determinant. The third hypothesis considers both mechanisms to be important.

As a result of calf muscle activation, the muscle pump effect increases venous return by collapsing the deep veins embedded within the muscle. Furthermore, backflow towards the arterial system and into the superficial venous system is prevented by closure of the distal and perforating venous valves respectively (Figure 2.1A) (Rowell, 1993). Arterial inflow rises during subsequent muscle relaxation as the perfusion pressure is increased due to the pressure shielding of the closed proximal valve (Figure 2.1B) (Rowell, 1993). Furthermore, the opening of the distal and perforating valves (Meissner, 2005) allows venous refilling from both the arterial and superficial venous system. In summary, the muscle pump effect increases blood flow through an increase in arterio-venous pressure drop.

In a previous study (Chapter 2), we examined the role of venous valves, hydrostatic pressure and the superficial veins during the muscle pump using a mathematical model. Although the model was able to simulate the increased venous return during muscle contraction and the elevated arterial flow during muscle relaxation, the predicted flow augmentation was low compared to the increase in arterial flow increase measured during *in vivo* calf muscle contractions (Nådland et al., 2009). Based on the debate in literature (Nådland et al., 2009; Tschakovsky et al., 1996), it was proposed that vasodilation could be the missing component in the model. Furthermore, the simulated arterial baseline flow in the tilted position was equal to the baseline flow in the supine position, which was in strong contrast with the 50% decay observed *in vivo* (Nådland et al., 2009). These postural changes can be attributed to changes in peripheral resistance due to myogenic vasoconstriction and a global increase in peripheral resistance (Nådland et al., 2009). Therefore, in this study our previous model is extended to include regulation of vascular tone.

Regulation of vascular tone in skeletal muscle tissue is not based on a single mech-

anism, but involves the interaction between the local myogenic, local metabolic and global baroreflex regulation (Joyner and Casey, 2015). Myogenic regulation protects the capillaries against high pressures by vasoconstriction as transmural pressure increases (Boron and Boulpaep, 2003). The metabolic mechanism induces vasodilation when the amount of metabolites accumulates, thereby regulating the oxygen delivery and removal of waste products (Boron and Boulpaep, 2003; Joyner and Casey, 2015). Finally, the baroreflex initiates vasoconstriction when central pressure detected by the baroreceptors in the aortic arch and the carotid artery decreases. In addition, the baroreflex affects heart rate, cardiac contractility and venous unstressed volume (Boron and Boulpaep, 2003; Rowell, 1993). A combined regulation model including all three components is thus required to describe the resulting vascular tone. As all three mechanisms respond to different parameters and with different time delays, this suggests each should be modelled as a separate component. The definition of specific parameters for each mechanism, allows us to examine the relative activation of the three mechanisms during muscle contraction and relaxation.

Previous numerical studies of regulation of vascular tone have focussed on cerebral auto-regulation or the baroreflex. Ursino (1988) developed a model for cerebral autoregulation including a neurogenic and endothelial response in addition to the myogenic and metabolic mechanism. This model was used to investigate the relation between cerebral blood volume and intracranial pressure changes (Ursino and Giammarco, 1991) and applied to examine cerebral regulation under squat exercise and visual stimulation (Spronck et al., 2012). Models of the baroreflex have been applied to study various physiological responses, e.g. the interaction between the baroreflex and a pulsating heart model (Ursino, 1998), heart rate variability (Ursino and Magosso, 2003), fetal welfare during labor (van der Hout-van der Jagt et al., 2013) and heart rate regulation under orthostatic stress (Olufsen et al., 2006). However, to our knowledge, no model exists that combines myogenic, metabolic and baroreflex regulation to simulate the vascular tone response to a skeletal muscle contraction.

The aim of this study was to determine the importance of the myogenic, metabolic and baroreflex regulation during the different phases of muscle contraction. Therefore, the 1D arterio-venous model as described in Chapter 2 was extended with a regulation model for the vascular tone, which includes both the myogenic and metabolic effects described by Spronck et al. (2012), combined with the baroreflex model of Ursino (1998) to include all three mechanisms. In an initial explorative analysis, the intuitively most important model parameters representing the gain of the myogenic and metabolic mechanism were fitted to match the measured *in vivo* flow response to a muscle contraction in the supine position. Secondly, the same parameters were used to predict the response to a muscle contraction in the tilted position. Finally, a sensitivity analysis was performed to quantify which parameters are most

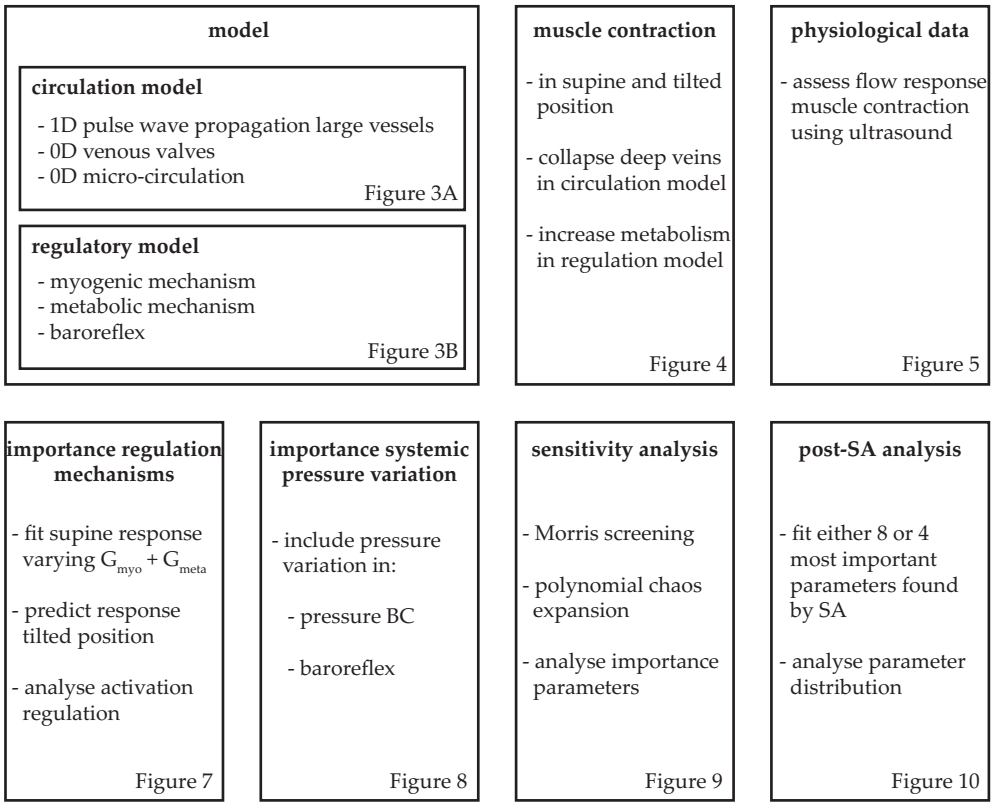

Figure 4.1: Schematic overview of the methods as described in this study including: circulatory and regulation model, simulation of a muscle contraction, physiological data, and the four analyses performed. For each part the main points are given together with the corresponding figures.

important for the variance in the flow response. For the sensitivity analysis the two step approach as described by Donders et al. (2015) was used. This approach consists of an initial Morris screening and a subsequent generalized polynomial chaos expansion (gPCE). We conclude with an analysis varying the most important parameters, identified by the sensitivity analysis, to fit the *in vivo* response.

4.2 Methods

In this section the methods are described and a schematic overview can be observed in Figure 4.1.

4.2.1 Model

To study the hemodynamic and local regulatory response to muscle contraction in the lower limb a simplified model of the calf circulation was constructed (Figure 4.2). The model includes an artery, supplying the muscle tissue with oxygen, a deep vein, embedded in the muscle tissue, and a superficial vein, between the skin and the muscle. To model regulation of vascular tone the mean response of the arterioles is included into a single model variable which represents the regulatory state. This state is based on the myogenic, metabolic and baroreflex regulation (Figure 4.2B). Changes in peripheral resistance are induced by relating the resistance to the regulation state. The following section describes the physiological background and governing equations of the various model components.

1D Pulse wave propagation: arteries and veins

The hemodynamics in the large arteries and veins is captured using the 1D equations for mass and momentum balance, with blood assumed to be an incompressible Newtonian fluid. The resulting equations read:

$$C\frac{\partial p_{\text{tr}}}{\partial t} + \frac{\partial q}{\partial z} = 0, \tag{4.1}$$

$$\frac{\partial q}{\partial t} + \frac{\partial A\overline{v_z^2}}{\partial z} + \frac{A}{\rho}\frac{\partial p}{\partial z} = \frac{2\pi a}{\rho}\tau_w + Ag_z, \tag{4.2}$$

where C is the compliance per unit length, $p_{\text{tr}} = p - p_{\text{ex}}$ is the transmural pressure, p and p_{ex} are the intra- and extravascular pressure respectively, q is the flow, t is the time and z is the axial coordinate. Furthermore, A is the cross-sectional area, $\overline{v}_z$ is the velocity in axial direction averaged over the cross-sectional area, ρ is blood fluid density, $a = \sqrt{A/\pi}$ is the radius and τ_w is the wall shear stress. Additionally, $g_z = g\,\mathbf{e_g}\cdot\mathbf{e_z}$ is the contribution of the gravitational acceleration in the axial direction, g is the magnitude of the gravitational acceleration on earth, $\mathbf{e_g}$ is the unit vector in the direction of gravity and $\mathbf{e_z}$ is the unit vector in axial direction.

To obtain an estimation of the wall shear stress τ_w and the advection term $\frac{\partial A\overline{v_z^2}}{\partial z}$ the approximate velocity profile is used (see Bessems et al. (2007) for more details). Here, the pressure gradient and the gravitational forces are assumed to be in balance with viscous forces in the boundary layer close to the vessel wall. In the central core inertia forces are assumed to be in balance with the pressure gradient and the gravitational forces. Finally, a constitutive law relating cross-sectional area and pressure, is defined for both arteries and veins.

As the arterial cross-sectional area variations during the cardiac cycle are small under normal conditions, the mechanical characteristics of the arterial wall are modeled

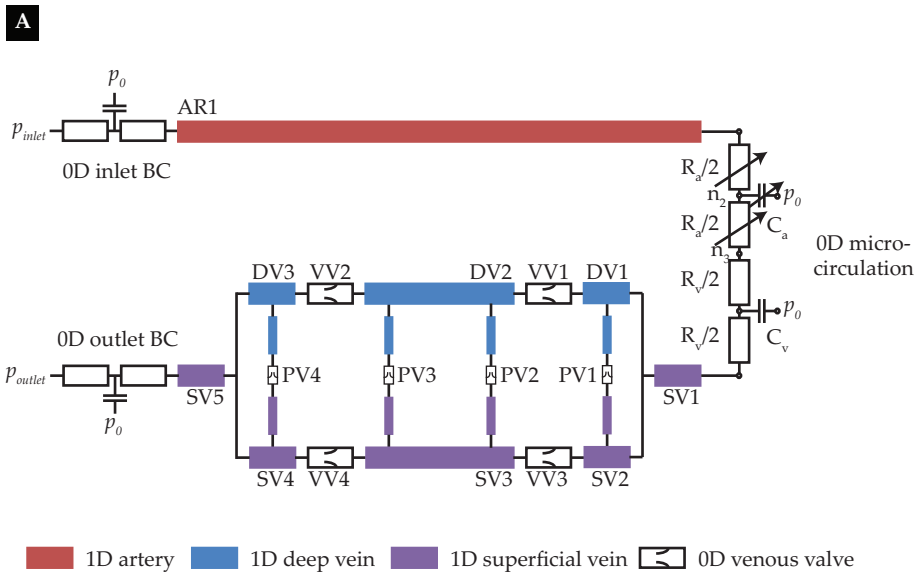

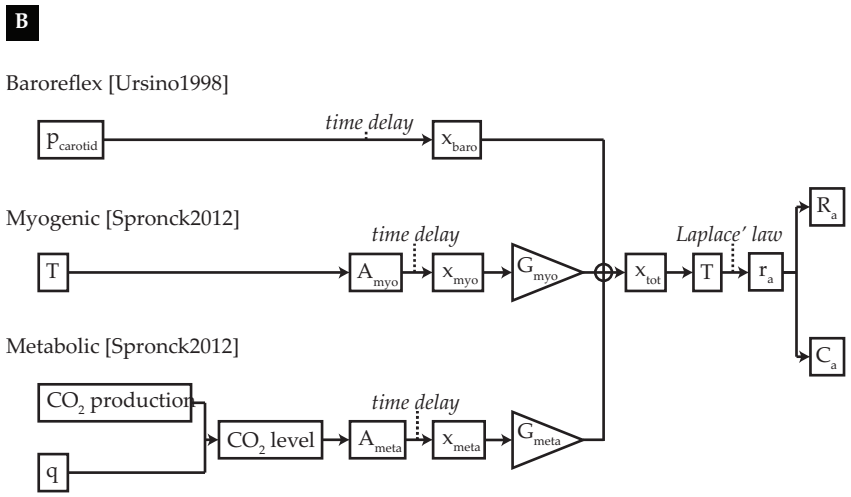

Figure 4.2: Model. **A** Model configuration of the calf circulation including: 1D artery (AR), a 1D deep (DV) and superficial (SV) vein, 0D venous valves (VV), a 0D micro-circulation, an a 0D inlet and outlet boundary condition (BC). The length and radius of the 1D elements are not to scale (geometrical parameters of all 1D segments can be found in Table 4.1) **B** Schematic overview of the regulation model including baroreflex, myogenic and metabolic regulation

with the following linear A, p relation

$$A = A_{\text{ref,A}} + C(p_{\text{tr}} - p_{\text{ref,A}}), \tag{4.3}$$

where $A_{\text{ref,A}}$ is the reference cross-sectional area at reference pressure $p_{\text{ref,A}}$ and C the linearized compliance per unit length at reference pressure $p_{\text{ref,A}}$. The compliance is determined using thin-walled-cylinder theory for a linear isotropic elastic material:

$$C = \frac{\partial A}{\partial p_{\text{tr}}}\bigg|_{p_{\text{tr}}=p_{\text{ref,A}}} = \frac{2\pi(1-\nu^2)r_{\text{ref,A}}^3}{hE}\ , \tag{4.4}$$

where ν is the Poisson's ratio, $r_{\text{ref,A}} = \sqrt{A_{\text{ref,A}}/\pi}$ is the reference radius, $h \approx r_{\text{ref,A}}/10$ is the vessel wall-thickness (Westerhof et al., 1969) and E is the Young's modulus.

Because veins are prone to collapse under low transmural pressures due to e.g. increasing extravascular pressure during muscle contraction or gravitational stress, a nonlinear pressure area relationship needs to be considered. Therefore, Shapiro (1977) derived a tube law capturing the venous collapse with an p, A-relation. In order to solve the full system of equations for pressure a fit of the tube law is used as derived in Chapter 2.

$$A = A_{\text{ref,V}}\left\{h(p^*)f^+(p^*) + (1-h(p^*))f^-(p^*)\right\}, \tag{4.5}$$

where $A_{\text{ref,V}}$ is the reference cross-sectional area at zero transmural pressure, $p^* = p_{\text{tr}}/K_p$ is the dimensionless pressure and K_p is the bending stiffness. The functions f^+ and f^- are fits of the positive and negative pressure part of the original tube law of Shapiro and $h(p^*)$ is a scaling function.

$$f^+(p^*) = \frac{A_0^+}{\pi}\left(\tan^{-1}\left(\frac{p^*-p_a^+}{p_b^+}\right)+\frac{\pi}{2}\right), \tag{4.6}$$

$$f^-(p^*) = B + \frac{A_0^-}{\pi}\left(\tan^{-1}\left(\frac{p^*-p_a^-}{p_b^-}\right)+\frac{\pi}{2}\right), \tag{4.7}$$

$$\text{and} \qquad h(p^*) = \frac{1}{\pi}\left(\tan^{-1}\left(\frac{\gamma p^*}{\pi}\right)+\frac{\pi}{2}\right), \tag{4.8}$$

where B, A_0^-, p_a^-, p_b^-, A_0^+, p_a^+, p_b^+ and γ are fitting constants determining the shape of the A,p-relation. Venous compliance is calculated as the derivative of cross-sectional area with respect to the transmural pressure.

0D Venous valves

The pressure-flow relation of a venous valve is included using the versatile valve model of Mynard et al. (2012). As the flow through venous valves is much lower

Table 4.1: Geometrical parameters of the various 1D vessels Müller and Toro (2014) as depicted in Figure 4.2. The four perforating veins consist of a deep (PV#-D) and a superficial (PV#-S) vein of which the parameters are noted separately.

Vessel	Numbering (Figure 4.2)	Radius [mm]	Length [cm]
artery	AR1	2.5	34
deep vein	DV1	1.5	2
	DV2	1.5	26
	DV3	1.5	2
superficial vein	SV1	3.5	2
	SV2	1.5	2
	SV3	1.5	26
	SV4	1.5	2
	SV5	3.5	2
perforating vein	PV#-S	0.5	1.5
	PV#-D	0.5	1.5

compared to heart valves, the linear viscous forces are included, as in Chapter 3.

$$\Delta p = Rq + Bq|q| + L\frac{\partial q}{\partial t}, \tag{4.9}$$

where the Poiseuille resistance R, Bernouilli resistance B and the inertance L are defined by

$$R = \frac{8\pi\eta l_{\text{eff}}}{A_{\text{eff}}^2}, \qquad B = \frac{\rho}{2A_{\text{eff}}^2} \qquad \text{and} \qquad L = \frac{\rho l_{\text{eff}}}{A_{\text{eff}}}, \tag{4.10}$$

where A_{eff} is the effective cross-sectional area, η is the dynamic blood viscosity, and $l_{\text{eff}} = \beta_l \cdot r_{\text{ref,V}}$ is the effective valve length defined as a multiple β_l of the venous reference radius $r_{\text{ref,V}} = \sqrt{A_{\text{ref,V}}/\pi}$ (Chapter 3). To include valve opening and closing, the effective cross-sectional area is defined to be a function of valve state ζ via the following relation

$$A_{\text{eff}} = (A_{\text{eff,max}} - A_{\text{eff,min}})\,\zeta + A_{\text{eff,min}}, \tag{4.11}$$

where $A_{\text{eff,min}}$ and $A_{\text{eff,max}}$ are the minimal and maximal effective cross-sectional area respectively. Here, maximal effective cross-sectional area $A_{\text{eff,max}} = \beta_A \cdot A_{\text{ref,V}}$ is defined as a multiple β_A of the reference cross-sectional area $A_{\text{ref,V}}$ of the connecting vein. The valve state is defined to vary between zero and one (fully closed: $\zeta = 0$, fully open: $\zeta = 1$). Its value is related via two differential equations for valve opening and closing respectively:

$$\frac{d\zeta}{dt} = \begin{cases} (1-\zeta)\,K_{\text{vo}}\,(\Delta p - dp_{\text{valve,0}})\,, & \text{if } \Delta p > dp_{\text{valve,0}} \\ \zeta K_{\text{vc}}\,(\Delta p - dp_{\text{valve,0}})\,, & \text{if } \Delta p < dp_{\text{valve,0}} \end{cases}, \tag{4.12}$$

where K_{vo} and K_{vc} are coefficients determining the opening and closing speed of the valve. Furthermore, $dp_{\text{valve,0}}$ is the pressure drop above and below which opening and closing is initiated.

0D micro-circulation

To account for the pressure drop over the micro-circulation (in the current study defined to include the arterioles, capillaries and venules) and its storage capacity, the micro-circulation model consists of both resistances and compliances. The micro-circulation is split into an arteriolar and venular part, both consisting of two resistances R_{i} ($i = a, v$) in series and a compliance C_{i} ($i = a, v$) connected to the extravascular pressure, for which the following relations hold (Figure 5.1A).

$$\Delta p = R_{\mathrm{i}} q \qquad \text{and} \qquad \frac{\partial p_{tr}}{\partial t} = \frac{1}{C_{\mathrm{i}}} q. \tag{4.13}$$

Under baseline conditions the total resistance of the two parts is determined by the pressure drop over the micro-circulation Δp_{bl} and the time-avaraged baseline flow $\overline{q_{\mathrm{bl}}}$ according to

$$R_{\mathrm{tot}} = \frac{\Delta p_{\mathrm{bl}}}{\overline{q_{\mathrm{bl}}}} = R_{\mathrm{a}} + R_{\mathrm{v}}, \tag{4.14}$$

where R_{v} is chosen such that the pressure drop over the venules is 400 Pa (Boron and Boulpaep, 2003). Furthermore the baseline total compliance C_{tot} is derived from a typical time-constant τ_{RC} as in a classical single windkessel micro-circulation (Chapter 2). The compliance of the venules is assumed to be much larger than arteriolar compliance (Boron and Boulpaep, 2003). Therefore, the compliances are distributed as follows

$$C_{\mathrm{a}} = 0.3 \cdot C_{\mathrm{tot}} \qquad \text{and} \qquad C_{\mathrm{v}} = 0.7 \cdot C_{\mathrm{tot}}. \tag{4.15}$$

The above equations for resistance and compliance relate to the baseline conditions. However, for the arteriolar part of the micro-circulation the resistance and compliance are regulated by vascular tone as described in the following subsection.

Regulation of vascular tone

Regulation of the vascular tone in muscular tissue is based on the following mechanisms:

- Myogenic regulation: protecting the capillaries against excessive pressures
- Metabolic regulation: matching the blood flow to the oxygen demand
- Baroreflex regulation: aiming to maintain the level of systemic pressure

The regulation model is based on the implementation of cerebral auto-regulation as described by Spronck et al. (2012). In this study, each regulation mechanisms is included individually and represented by a regulatory state. The total regulatory state

is translated to arteriolar wall tension and is subsequently converted to arteriolar radius using Laplace's law. Finally, the arteriolar radius is used to determine the change in peripheral resistance. The myogenic regulation mechanism is included as described by Spronck et al. (2012), but the metabolic mechanism adjusted to induce metabolic activation upon muscle contraction instead of cerebral activity. Furthermore, tissue specific parameters are updated to match muscle tissue. Finally, baroreflex regulation is added to the model based on the study of Ursino (1998). For completeness, the equations describing the activation of the three regulation mechanisms and how they affect a change in resistance and compliance are given in Appendix B.

Boundary conditions

Both the inlet of the 1D arterial and the outlet of the 1D venous part are connected to a three element windkessel model representing the proximal vasculature. Each windkessel element consists of two resistances in series and a compliance connected to the extravascular pressure p_0 (Equation (4.13)). The total windkessel resistance is the sum of the Poiseuille resistances of the proximal vasculature, based on the geometrical parameters of the arterial and venous tree published by Müller and Toro (2014). Similarly, the inlet and outlet compliance is the sum of the compliances of the proximal vasculature based on Equation (4.4) and the derivative of Equation (4.5) times the length respectively. At the inlet and outlet the pressure is set to a time-averaged p_{inlet} and p_{outlet} respectively. When a head up tilt position is simulated the hydrostatic column up to the heart is added to both the inlet and outlet pressure.

The model formulation described above is completed for the current application by defining the form of the muscle contraction.

Simulating muscle contraction

The effect of a muscle contraction is included in the current model both in a mechanical and a metabolic manner. The mechanical effect on the deep veins is expected to be large due to their location, embedded in the muscle tissue, and the low intravascular pressure. Similar to Chapter 2, a muscle contraction is simulated by an increase in extravascular pressure included in the equation for mass balance and the venous constitutive law (Equation (4.1) and (4.5) respectively). The extravascular pressure is defined by the following relation

$$p_{\text{ex}} = p_{\text{ex,max}} \cdot k(t) \cdot m(z), \tag{4.16}$$

where $p_{\text{ex,max}}$ is the maximal extravascular pressure, and $k(t)$ and $m(z)$ are the temporal and spatial course of extravascular pressure, respectively. The latter can be observed in Figure 2.4, and the full equations are give in Appendix A. The influence of the muscle contraction on the superficial veins is assumed to be negligible due to

their location outside the muscle tissue. Furthermore, due to the high arterial pressure the influence of the muscle contraction on the arterial cross-sectional area is also assumed to be negligible. Finally, the mechanical influence on the micro-circulation is also assumed to be negligible due to its viscous character (in Equation (4.13) and (B.1)) (Gray et al., 1967). Although contradicted in some studies (Tschakovsky et al., 1996), few experimental studies hypothesize the decrease in transmural pressure could induce myogenic vasodilation (Tschakovsky and Sheriff, 2004), but implementation of this theory requires more accurate knowledge of the magnitude of extravascular pressure and is therefore neglected.

The increase in metabolism due to a muscle contraction is included in the metabolic mechanism of the regulation of vascular tone via muscle activation A_{mc} (Equation (B.14)). Because the flow increase due to a muscle contraction increases linearly with increasing contraction intensity (Tschakovsky et al., 2004), muscle activation is defined to follow the contraction pattern defined by the extravascular pressure and reaches a maximum of $A_{\text{mc,max}}$ corresponding to the percentage of maximum electromyogram (EMG) activity:

$$A_{\text{mc}} = A_{\text{mc,max}} \cdot k(t). \tag{4.17}$$

Numerical implementation

The model equations were implemented in the finite element package SEPRAN (Ingenieursbureau SEPRA, Leidschendam, the Netherlands) using the computational method described by Kroon et al. (2012). Time discretization was included based on an implicit Euler scheme with a time step of $\Delta t = 1.0$ ms and spatial discretization based on the trapezium rule with element size $\Delta z = 1.0$ cm for arterial and superficial venous segments, and $\Delta z = 0.5$ cm for the deep venous segments, which is necessary to capture the collapse accurately. The model parameters that are not included in the sensitivity analysis are summarized in Table 4.2. Pre- and post-processing was performed using MATLAB R2012b (MathWorks, Natick, MA, USA).

4.2.2 Physiological data

Pressure and flow measurements were performed on twelve healthy subjects (29 ± 3 years, six male, six female, BMI: 23.4 ± 2.3 kg m^{-2}) during muscle contraction in both the supine and 70° head up tilt positions. These experiments were approved by the ethical committee of the Northern Rhine Medical Association, Germany (*Ethikkommission der Ärztekammer Nordrhein*). Subjects were asked to perform a contraction of the left calf muscle corresponding to 30% of maximal electromyography (EMG) activity (Ambu Blue Sensor N, Ballerup, Denmark). Visual feedback of the relative

Table 4.2: Constant model parameters

Symbol	Value	Unit	Description
ρ	1050	kg m^{-3}	Blood mass density (Kenner, 1989)
g	9.81	m s^{-1}	Gravitational acceleration
$p_{\text{ref,A}}$	13	kPa	Arterial reference pressure (Bessems et al., 2007)
ν	0.5	-	Poisson's ratio (Westerhof et al., 1969)
E	1.6	MPa	Arterial Young's modulus (Westerhof et al., 1969)
K_p	425	Pa	Bending stiffness (Müller and Toro, 2014)
A_0^+	1.37	-	Fitting constant (Chapter 2)
p_a^+	-2.53	-	Fitting constant (Chapter 2)
p_b^+	3.02	-	Fitting constant (Chapter 2)
B	0.108	-	Fitting constant (Chapter 2)
A_0^-	1.28	-	Fitting constant (Chapter 2)
p_a^-	-1.49	-	Fitting constant (Chapter 2)
p_b^-	2.03	-	Fitting constant (Chapter 2)
γ	4	-	Fitting constant (Chapter 2)
η	4.5	mPa s	Dynamic blood viscosity (Letcher et al., 1981)
β_l	1.0	-	Effective valve length ratio (Chapter 3)
$A_{\text{eff,min}}$	1.0	10^{-20} m^2	Minimal effective valve cross-sectional area (Mynard et al., 2012)
β_A	0.65	-	Effective valve cross-sectional area ratio (Chapter 3)
K_{vo}	0.3	Pa^{-1}s^{-1}	Valve opening constant (Mynard et al., 2012)
K_{vc}	0.3	Pa^{-1}s^{-1}	Valve closing constant (Mynard et al., 2012)
$dp_{\text{valve,0}}$	0	Pa	Valve opening and closing pressure drop (Chapter 3)

muscle activity was provided to enable the subjects to maintain muscle activity at the prescribed level. During the experiment blood pressure waveforms were measured at the finger using photoplethysmography (Finometer Midi, AD instruments), while maintaining the wrist at heart level. Furthermore, femoral artery blood flow was assessed using a Mylab 25 ultrasound scanner (Esaote, the Netherlands) equipped with a linear array probe and having a center frequency of 10 MHz. The blood flow measurement were performed in pulsed-Doppler mode. Blood flow was estimated from mean blood flow velocity and vessel diameter using the Poiseuille formulation (Leguy et al., 2009).

To use the experimental data for validation of the simulated muscle flow, the *in vivo* flow decay after muscle contraction (10 s $< t <$ 50 s) was captured using the following exponential decay relation and a non-linear least squares fit.

$$q_{\text{fit}}(t) = q_0 + (q_{\text{max}} - q_0)e^{-(t-t_{\text{max}})/\tau}, \tag{4.18}$$

where $t_{\text{max}} = 10$ s, q_0 is the baseline flow, q_{max} is the flow at $t = t_{\text{max}}$ and τ is the time constant of the flow decay. Measurements are excluded from postprocessing when (1) average arterial pressure is below 50 mmHg for a whole experiment, (2) femoral artery flow was only measured successful during part of the experiment and (3) the quality of the flow fit was too low ($R^2_{\text{adj}} < 0.6$). An average of the pressure and

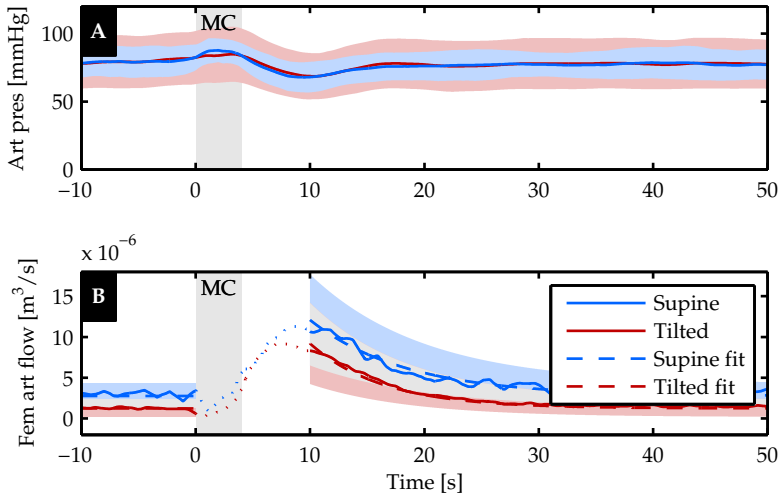

Figure 4.3: Finger pressure **A** and femoral artery flow **B** response to a muscle contraction in supine (red) and head up tilt (blue) position. The gray area indicates the 4-s muscle contraction (MC). Furthermore, the fit (−−) to the flow response is included, where its uncertainty is indicated with the shaded area around (light gray indicates the overlap). The dotted line (··; $0 < t < 10$ *s*) indicates the uncertain part of the flow curve due to measurement difficulties. Fitting parameters and their standard deviation can be found in Table 4.3.

femoral artery flow was derived in the supine and head up tilt positions using the following relation

$$\overline{\overline{x}}(t) = \frac{1}{N_{\text{subj}}} \sum_{\text{i}_{\text{subj}}}^{N_{\text{subj}}} \frac{1}{N_{\text{MC,i}_{\text{subj}}}} \sum_{i_{\text{MC}}}^{N_{\text{MC,i}_{\text{subj}}}} x_{\text{i}_{\text{subj}},\text{i}_{\text{MC}}}(t), \tag{4.19}$$

where N_{subj} is the number of subjects, $N_{\text{MC,i}_{\text{subj}}}$ is the number of muscle contractions performed by subject i_{subj} and $x_{\text{i}_{\text{subj}},\text{i}_{\text{MC}}}(t)$ is the waveform obtained during muscle contraction i_{MC} of subject i_{subj}. The corresponding intersubject standard deviation was derived using the following relation:

$$\sigma^2(t) = \frac{1}{N_{\text{subj}} - 1} \sum_{\text{i}_{\text{subj}}}^{N_{\text{subj}}} \left(\overline{x}_{\text{i}_{\text{subj}}} - \overline{\overline{x}}(t)\right)^2, \tag{4.20}$$

where $\overline{x}_{i_{\text{subj}}}(t)$ is the mean response of subject i_{subj}. The resulting time averaged pressure and femoral artery flow are shown in Figure 4.3A and B respectively, with the supine measurement in red and the head up tilt in blue. The area around the fitted curve represents one standard deviation from the average fit.

Table 4.3: Fitting parameters of the flow decay after muscle contraction using the following equation: $q_{\text{fit}}(t) = q_0 + (q_{\text{max}} - q_0)e^{-(t-t_{\text{max}})/\tau}$

	q_0 [mL/s]	q_{max} [mL/s]	τ [s]
Supine	2.8 ± 1.5	12.1 ± 5.6	8.4 ± 1.6
Head up tilt	1.2 ± 1.1	9.2 ± 5.0	6.4 ± 2.2

4.2.3 Simulations and analysis

The first aim is to match the simulated flow response during a supine muscle contraction to the measured data (Figure 4.3B), to gain insight into the importance of the various regulation mechanisms. An explorative local analysis including variation of x_{init}, $T_{\text{max},0}$, G_{meta} and G_{myo}, identified G_{meta} and G_{myo} as the major determinants. Therefore, G_{meta} and G_{myo} were varied ($-25 < G_{\text{meta}} < -15$; $dG_{\text{meta}} = 1$ and $0.5 < G_{\text{myo}} < 1.5$; $dG_{\text{myo}} = 0.25$) during the fitting procedure, while keeping all other regulation parameters at their baseline values (55 model evaluations). The best three sets of gains are derived based on the least square of the difference between the simulated flow response and the *in vivo* fit.

$$\epsilon = \int_{t=10\ s}^{50\ s} \sqrt{(q_{\text{sim}} - q_{\text{fit}})^2} dt. \tag{4.21}$$

These parameters are then used to repeat the simulation in the head up tilt position. Apart from obtaining a nice fit, the second aim of the first analysis is to determine the relative importance of the regulation mechanisms. Because the regulation mechanisms are included individually their relative importance can be analyzed directly.

In the above mentioned analysis a constant pressure is used as an input for the baroreflex and the inlet boundary condition. However, *in vivo* the systemic pressure shows a small increase during and a decrease after muscle contraction (Figure 4.3). In a second analysis the influence of this pressure fluctuation via the systemic pressure and the baroreflex regulation on the flow response was investigated. For this the best parameter set, derived in the first analysis, was used to repeat the supine and tilted simulations with the following adaptations: (1) *in vivo* pressure is used as an input for the baroreflex and p_{inlet} remains unchanged compared to the previous simulations; (2) *in vivo* pressure is used as an input for the baroreflex as well as for p_{inlet}.

4.2.4 Sensitivity analysis

To investigate the importance of all regulation parameters on the flow response to a muscle contraction and to validate the choice to derive the fit based on only G_{meta} and G_{myo} as described in the previous section, a global sensitivity analysis was per-

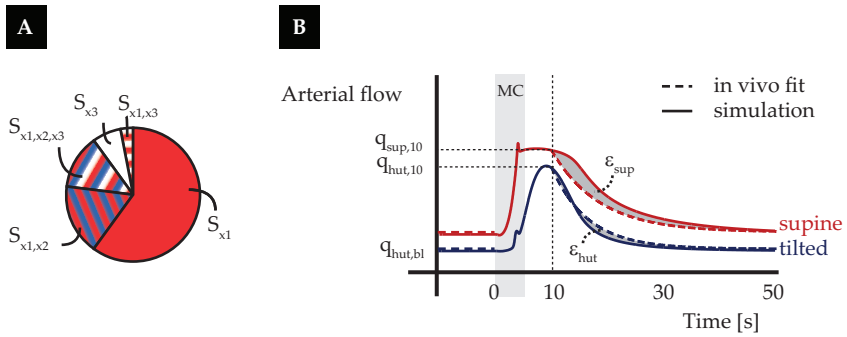

Figure 4.4: Sensitivity analysis **A** Schematic visualisation of the distribution of the output variance over the various input parameter and their interactions. S_i = main sensitivity index, S_{ij} = second order effect, S_{ijk} = third order effect. **B** Output of interest visualized in a plot of the flow response to a muscle contraction in supine and tilted position.

formed. Simultaneous variation of the input parameters within their uncertainty range enables the derivation of the variance in the simulated flow response. Each fraction of this output variance can be allocated to individual parameters or interaction between two or more input parameters (Figure 4.4A). The influence of an individual input parameter is captured by the main sensitivity index S_i, which can be interpreted as the expected reduction in output variance if the true value would have been known. The contribution of interaction between two or more parameters is captured by the higher order effects ($S_{ij}, S_{ijk}, ...$) (Eck et al., 2016).

Output of interest

The following parameters, describing the flow response to a muscle contraction in both supine and tilted position, are used as outputs of interest:

- $q_{\text{sup,max}}$: Flow in supine position $10\ s$ after the onset of muscle contraction.
- $\epsilon_{\text{sup}} = \int_{t=10\ s}^{50\ s} \sqrt{(q_{\text{sim,sup}} - q_{\text{fit,sup}})^2}$: Root mean square of the difference between the simulation and the fit of the flow response to a muscle contraction in the supine position.
- $q_{\text{hut,bl}}$: Baseline flow in the tilted position.
- $q_{\text{hut,max}}$: Flow in the tilted position $10\ s$ after the onset of muscle contraction.
- $\epsilon_{\text{hut}} = \int_{t=10\ s}^{50\ s} \sqrt{(q_{\text{sim,hut}} - q_{\text{fit,hut}})^2}$: Root mean square of the difference between the simulation and the fit of the flow response to a muscle contraction in the tilted position.

Input parameters

The sensitivity analysis was performed while varying all input parameters of the regulation model. A description of these parameters can be found in Table 4.4, along with their baseline value and the range used for the sensitivity analysis. The uncertainty ranges are based on literature values or values resulting in a physiological flow response determined by a local sensitivity analysis (results not shown). From this local sensitivity analysis, it was concluded that r_m and r_t should be fixed, as even small variation resulted in non-physiological responses or decreased model stability.

Table 4.4: Model input parameters included in the sensitivity analysis. Uncertainty range is given in percentages, unless indicated with superscript ABS when the absolute range is given. The uncertainty range is based on literature values and is adapted when the local sensitivity analysis indicated unphysiological outputs or decreasing in model stability.

Symbol	Value	Unit	Description	Range
$\sigma_{e,0}$	1.49	kPa	Parameter for elastic tension model (Laplace) (Ursino and Giammarco, 1991)	-10,7.5
K_σ	4.5	-	Parameter in tension model (Laplace) (Ursino and Giammarco, 1991)	-10,10
$r_{a,0}$	75.0	μ m	Arteriolar radius in unstressed condition (Laplace) (Ursino and Giammarco, 1991)	-10,10
σ_c	5.51	kPa	Stress contribution of collagen fibers (Laplace) (Ursino and Giammarco, 1991)	-10,10
$rh_{a,0}$	0.33	-	Unstressed arteriolar wall thickness relative to radius (Laplace) (Nordborg et al., 1985)	-10,10
η_a	6.37	kPa s	Arteriolar wall viscosity (Laplace) (Ursino and Giammarco, 1991)	-10,10
n_m	1.75	-	Parameter for smooth muscle tension model (Laplace) (Ursino and Giammarco, 1991; Ursino and Lodi, 1998)	-10,7.5
$T_{max,0}$	5.0	Pa	Smooth muscle tension in basal condition (Laplace) (Ursino and Giammarco, 1991; Ursino and Lodi, 1998)	4.0,5.5^{ABS}
x_{init}	-0.5	-	Offset regulation state (Laplace)	-0.6,-0.45^{ABS}
p_n	13.3	kPa	Reference pressure baroreflex model (Baroreflex) (Boron and Boulpaep, 2003)	-10,10
$f_{ab,min}$	2.52	s^{-1}	Minimal afferent firing rate (Baroreflex) (Ursino, 1998; Ursino and Magosso, 2000; van der Hout-van der Jagt et al., 2013)	-30,30
$f_{ab,max}$	47.78	s^{-1}	Maximal afferent firing rate (Baroreflex) (Ursino, 1998; Ursino and Magosso, 2000; van der Hout-van der Jagt et al., 2013)	-30,20

Table 4.4 – continued from previous page

Symbol	Value	Unit	Description	Range
k_{dp}	1.5676	kPa	Parameter defining slope of afferent firing rate (Baroreflex) (Ursino, 1998; Ursino and Magosso, 2000)	-20,30
$f_{\text{sp},\infty}$	2.1	s^{-1}	Sympathetic firing rate at infinite afferent firing rate (Baroreflex) (Ursino, 1998; Ursino and Magosso, 2000; van der Hout-van der Jagt et al., 2013)	-30,30
$f_{\text{sp},0}$	16.11	s^{-1}	Sympathetic firing rate at zero afferent firing rate (Baroreflex) (Ursino, 1998; Ursino and Magosso, 2000; van der Hout-van der Jagt et al., 2013)	-30,30
k_{es}	0.0675	s	Parameter defining the shape of the sympathetic firing rate (Baroreflex) (Ursino, 1998; Ursino and Magosso, 2000; van der Hout-van der Jagt et al., 2013)	-30,20
$f_{\text{sp,max}}$	60	s^{-1}	Maximal sympathetic firing rate (Baroreflex) (Ursino and Magosso, 2000; van der Hout-van der Jagt et al., 2013)	-30,30
G_R	0.33	MPa s m^{-3}	Gain baroreflex (Baroreflex) (Ursino and Magosso, 2000)	-30,15
D_R	2.0	s	Pure time delay sympathetic firing rate (Baroreflex) (Ursino, 1998; Ursino and Magosso, 2000; van der Hout-van der Jagt et al., 2013)	-30,30
$f_{\text{es,min}}$	2.66	s^{-1}	Minimal sympathetic firing rate affecting resistance (Baroreflex) (Ursino, 1998; Ursino and Magosso, 2000)	-30,20
τ_R	6.0	s	Time constant low pass filter baroreflex (Baroreflex) Ursino (1998); Ursino and Magosso (2000); van der Hout-van der Jagt et al. (2013)	-30,30
V	300	mL	Volume estimation of perfused muscle tissue (Metabolic) (Elliott et al., 1997)	-10,10
$C_{\text{a,CO}_2}$	20.65	mol m^{-3}	Arterial CO_2 concentration (Metabolic)	20.0,20.9[ABS]
f_m	75	-	Ratio of metabolism in rest and under maximal activity (Metabolic) (Boron and Boulpaep, 2003)	75,85[ABS]
$A_{\text{mc,max}}$	0.3	–	Percentage of maximum EMG reached during muscle contraction (Metabolic) (Tschakovsky et al., 2004)	-30,15
ρ_m	1055	kg m^{-3}	Muscle density (Metabolic) (Segal et al., 1986)	1040,1070[ABS]
$M_{\text{CO}_2,0,\text{m}}$	12.9	$\mu\text{mol s}^{-1}\ \text{kg}^{-1}$	Basal metabolic CO_2 production per kg muscle tissue (Metabolic) (Boron and Boulpaep, 2003)	9.0,13.5[ABS]
$\alpha_{\text{t,v}}$	0.49	-	Fitting constant venous CO_2 concentration (Metabolic) (Irving et al., 1932)	0.43,0.55[ABS]

Table 4.4 – continued from previous page

Symbol	Value	Unit	Description	Range
$\beta_{t,v}$	11.5	mol m^{-3}	Fitting constant venous CO_2 concentration (Metabolic) (Irving et al., 1932)	9.7,13.3^{ABS}
$C_{v,CO_2,0}$	22.34	mol m^{-3}	Venous CO_2 concentration at rest (Metabolic) (Geers and Gros, 2000)	22.1,23.0^{ABS}
G_{meta}	-15	-	Gain for metabolic mechanism (Metabolic)	-25,-10^{ABS}
τ_{meta}	15.0	s	Time-constant metabolic regulation (Metabolic) (Ursino and Lodi, 1998)	12,18^{ABS}
G_{myo}	0.75	-	Gain for myogenic mechanism (Myogenic)	0.1,5^{ABS}
τ_{meta}	7.0	s	Time-constant myogenic regulation (Myogenic) (Ursino and Lodi, 1998)	4,9^{ABS}

Morris screening and general polynomial chaos expansion

To derive the output variance and the sensitivity indices in a computationally efficient manner, the two-step approach described by Donders et al. (2015) was used. In the first step non-important model parameters are identified by using a Morris screening. In the second step the generalized polynomial chaos expansion method is applied to the reduced input space, resulting in a metamodel from which the sensitivity indices can be calculated straightforwardly (Huberts et al., 2014). The metamodel consists of orthogonal polynomials dependent on the model parameters and with output-specific coefficients, which are derived by a least-square regression of the metamodel and N simulations. The accuracy of the metamodel is determined by the quality of the regression, for which a sufficient number of model evaluations is needed. In the current study a metamodel containing orthogonal polynomials up to the third order is derived based on 13485 model evaluations ($CPU \approx 63\ h$, using 25 cores). The number of model evaluations is based on: $N = \binom{z+k}{z} \cdot q$, where $z = 3$ is the order of the metamodel, $k = 28$ is the number of input parameters of the reduced input space and q is set to 3 to have sufficient simulations to obtain a good regression.

Post sensitivity analysis

To investigate how well the important parameters identified in the sensitivity analysis can fit the *in vivo* response two additional sets of simulations were performed. First, all parameters with $S_T > 0.05$ for at least one output of interest were varied randomly over $k * 500$ simulations, with k the number of parameters. Second, the same process was carried out for all parameters with $S_T > 0.10$. For both sets of simulations it was investigated which simulations were in good agreement with the *in vivo* fit, i.e. within the standard deviation of the *in vivo* fit. A second subset is

defined to include all simulation within half the standard deviation. Finally, it is analysed how the input parameters of these subsets of simulations were distributed over the input space.

4.3 Results

This section first reports how the activation of the regulation mechanisms influences the agreement between the flow response and the *in vivo* data. Secondly, the influence of systemic pressure on the regulation is reported. Finally, the results of the sensitivity analysis are presented.

4.3.1 Baseline simulations

The regulatory response to a muscle contraction in the supine position was simulated while varying the gain of the myogenic and metabolic mechanism. The variation in regulatory responses and arterial flow are indicated by the gray region either side of the curve in Figure 4.5A and C respectively. The period of muscle contraction (MC) is indicated by the shaded region ($0 < t < 4\ s$). The arterial flow responses which best match the *in vivo* measurement ($-\cdot$ plus the standard deviation indicated by the blue area) are visualised in color. These parameters values are used to repeat the simulation in the tilted position, for which the results are shown in Figure 4.5B and D. For the best flow results the regulatory state of the baroreflex ($--$), metabolic ($-\cdot$) and myogenic ($\cdot\cdot$) mechanism are also shown in color.

Before the onset of muscle contraction in the supine position all the regulation states are equal to zero. After muscle contraction ($t > 4\ s$), the metabolic mechanism induces a strong vasodilation, whereas the myogenic mechanism and baroreflex show a mild and small vasoconstriction respectively (Figure 4.5A). Arterial flow shows an increase due to the muscle contraction and a gradual decay starting at $t \approx 10\ s$, which closely matches the *in vivo* response (Figure 4.5C). Most of the remaining flow responses show parallel waveforms, although some simulations cross due to a difference in decay (Figure 4.5C).

In the tilted position, the baroreflex and to a lesser extent the myogenic mechanisms induce a vasoconstriction at baseline ($-10 < t < 0\ s$). After muscle contraction ($t > 4\ s$), the metabolic response induces a vasodilation, slightly inhibited by the vasoconstrictive response of the myogenic mechanism and baroreflex (Figure 4.5B). Finally, arterial flow increases after muscle contraction and decreases back to baseline, matching the *in vivo* response (Figure 4.5D).

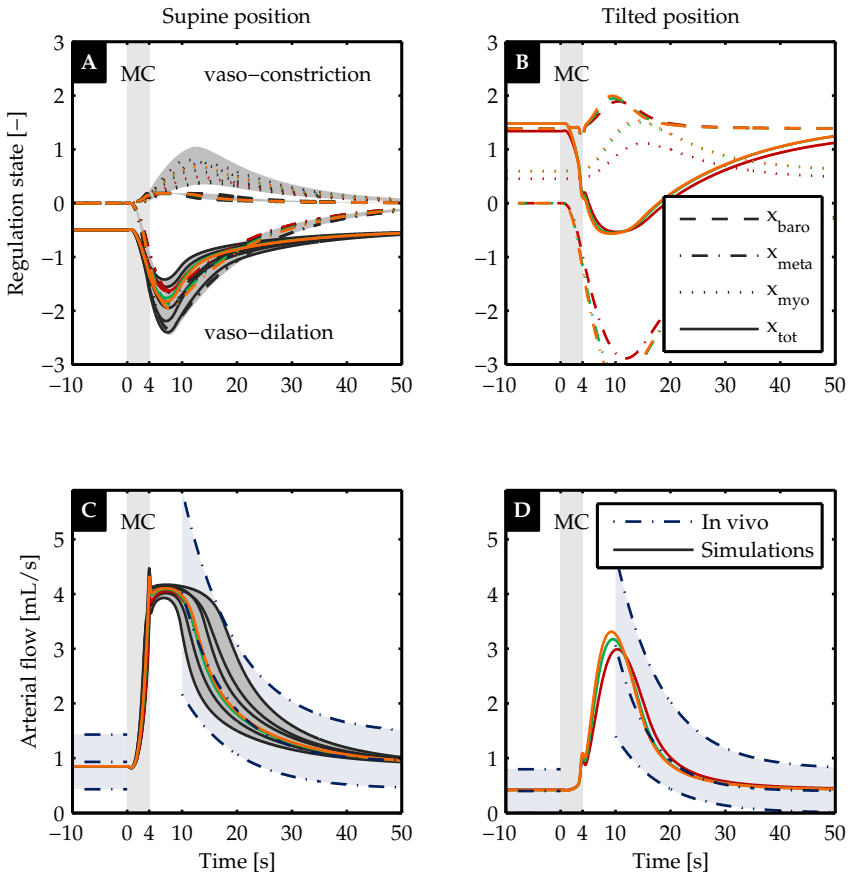

Figure 4.5: Regulatory response to muscle contraction in supine and tilted position, depicted in the left and right column respectively. In plot **A** and **B** the regulation state of the various mechanisms is shown over time: baroreflex (−−), metabolic (−·), myogenic (··) regulation and the sum of the three (−). Here, the negative state corresponds to vasodilation and the positive state to vasodilation. The resulting arterial flow is shown in plot **C** and **D** together with the fit to the *in vivo* response (−·). The simulations best matching the *in vivo* response are depicted in color. The remaining simulations are visualized together with the gray area and some individual responses are plotted in dark gray.

4.3.2 Influence of systemic pressure

The influence of the fluctuation in systemic pressure on the flow response to a muscle contraction is investigated. For this, the best fit found in the previous section is compared to a simulation with the pressure fluctuations included only in terms of the baroreflex regulation and a simulation with the pressure fluctuation applied at the inlet as well as the baroreflex. The regulatory (top) and flow (bottom) response to a muscle contraction in the supine (left) and tilted (right) position are shown in Figure 4.6.

In the supine position the three simulations all start at the same baseline and show a similar decay for $t > 10\ s$ (Figure 4.6C). Peak flow ($5 < t < 10\ s$) is lower once the pressure fluctuation is applied via baroreflex regulation (-). In the case where the pressure fluctuation is also applied as an inlet boundary condition (-) a fast decrease is observed shortly after muscle contraction followed by a plateau. In the tilted position all three simulations start at the same baseline (Figure 4.6D). The flow decay for $t > 10\ s$ is faster for both simulations with the *in vivo* pressure applied compared to the original simulation, but remain close to the fit of the *in vivo* response ($-\cdot$). Furthermore, peak flow is higher and is reached sooner following muscle contraction if the *in vivo* pressure is used.

4.3.3 Sensitivity analysis

Morris screening

From the Morris screening the following parameters were found to be unimportant: n_{m}, $f_{\text{ab,min}}$, k_{es}, D_{R}, $A_{\text{muscle,max}}$ and $M_{\text{CO}_2\text{,0,m}}$. Excluding these six parameters from the polynomial chaos expansion reduces the required number of simulations from 23310 to 13485.

Polynomial chaos expansion

The quality of the derived metamodels, captured by the descriptive error, is shown in Table 4.5. This gives the part of the variance that could not be captured by the metamodel. For the ϵ_{sup} and ϵ_{hut} the descriptive error is relatively large; 0.14 and 0.10 respectively.

The total sensitivity indices for all outputs of interest are shown in Table 4.6. The input parameters are arranged in order of importance and only contributions greater than 1% are shown. The myogenic gain G_{myo} is the most important parameter for all outputs of interest. Furthermore, the metabolic gain G_{meta}, the initial regulation

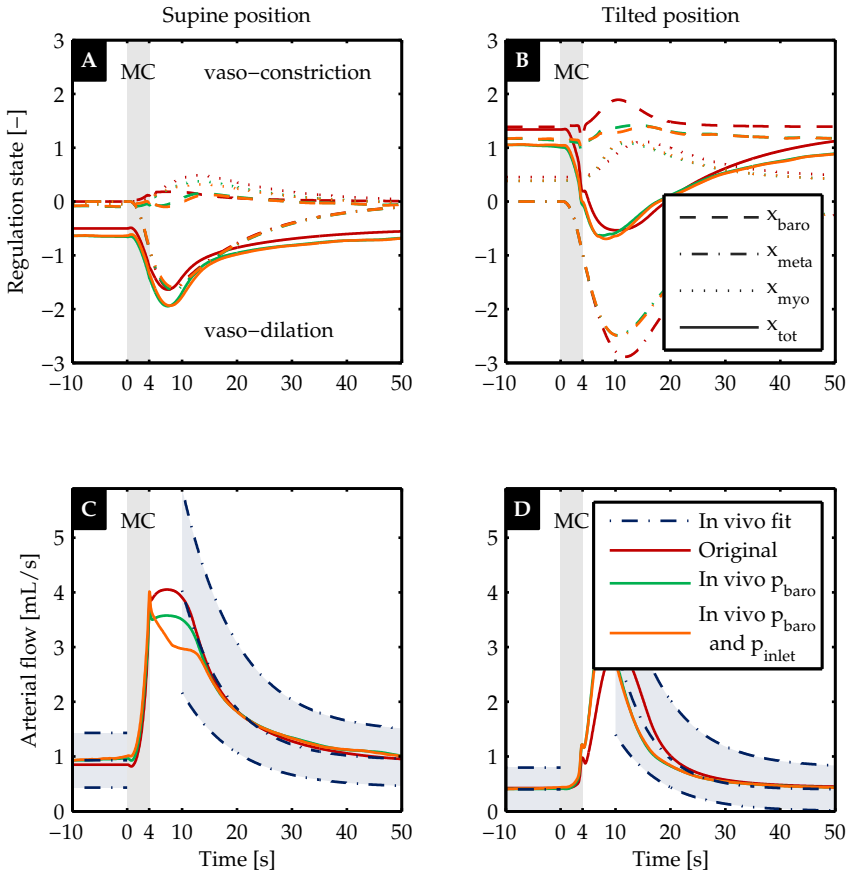

Figure 4.6: Influence of variation in systemic pressure on the regulatory response to muscle contraction in supine and tilted position (left and right column respectively). In plot **A** and **B** the regulation state of the various mechanisms is shown over time: baroreflex (−−), metabolic (··), myogenic (−·) regulation and the sum of the three (−). Here, the negative state corresponds to vasodilation and the positive state to vasodilation. The resulting arterial flow is shown in plot **C** and **D** together with the fit to the *in vivo* response (−·). The various color represent the original simulation (red), *in vivo* pressure applied at the baroreflex (green) and *in vivo* pressure applied to both the baroreflex and the inlet boundary condition (orange).

Table 4.5: Quality of the metamodel for each output of interest: $q_{\text{max,sup}}$, ϵ_{sup}, $q_{\text{bl,hut}}$, $q_{\text{max,hut}}$ and ϵ_{hut}. The error measure $1 - R^2$ can be interpreted as the residual variance that could not be captured by the metamodel.

	$q_{\text{max,sup}}$	ϵ_{sup}	$q_{\text{bl,hut}}$	$q_{\text{max,hut}}$	ϵ_{hut}
$1 - R^2$	0.04	0.14	0.01	0.06	0.10

Table 4.6: Total sensitivity indices of all the outputs of interest: $q_{\text{max,sup}}$, ϵ_{sup}, $q_{\text{bl,hut}}$, $q_{\text{max,hut}}$ and ϵ_{hut}. The input parameters are arranged in order of importance and only contributions starting at 1% are shown.

	$q_{\text{max,sup}}$	ϵ_{sup}	$q_{\text{bl,hut}}$	$q_{\text{max,hut}}$	ϵ_{hut}
G_{myo}	0.79	0.72	0.55	0.64	0.47
G_{meta}	0.08	0.17		0.18	0.30
x_{init}		0.02	0.38	0.04	0.11
τ_{meta}		0.16		0.02	0.09
$C_{\text{v,CO}_2,0}$	0.02	0.06		0.05	0.09
$C_{\text{a,CO}_2}$	0.02	0.06		0.05	0.09
r_0	0.06	0.06	0.02	0.01	0.02
$T_{\text{max,0}}$	0.03	0.03	0.01	0.03	0.05
τ_{myo}		0.08			0.03
$f_{\text{ab,max}}$		0.01	0.02	0.02	0.05
f_{m}	0.02	0.05		0.01	0.02
G_{R}		0.02	0.02	0.02	0.04
p_{n}	0.01	0.02	0.04	0.01	0.02
k_{dp}		0.01	0.01	0.02	0.03
K_σ	0.03	0.03			
$f_{\text{es,min}}$		0.02		0.01	0.03
$f_{\text{sp,}\infty}$		0.01		0.01	0.03
$f_{\text{sp,0}}$		0.02			0.01
σ_{e0}		0.02			
rh_0		0.02			
V		0.02			
α_{tv}		0.02			
σ_c		0.01			
η_a		0.01			
$f_{\text{sp,max}}$		0.01			
τ_{R}		0.01			
ρ_{m}		0.01			
β_{tv}		0.01			

state x_{init} and the metabolic time constant τ_{meta} all contribute more than 10% to the variance for at least one output of interest. This is in line with the first local analysis where a fit was derived based on G_{myo} and G_{meta}. Four other parameters have a contribution larger than 5%: $C_{\text{v,CO}_2,0}$, $C_{\text{a,CO}_2}$, r_0 and τ_{myo}. All other parameters have a smaller contribution, but they do all contribute to the variance of the output.

The main sensitivity indices and higher order interactions are shown in Figure 4.7, where the main sensitivity indices S_i are shown as ellipsoids, the second order interactions are indicated by an arrow and the third order interactions by a shaded area. The myogenic gain contributes most to the output variance; it has the highest main sensitivity index for all outputs of interest and is present in all of the main interactions. Furthermore, the metabolic gain G_{meta}, the initial regulation state x_{init} and the metabolic time constant τ_{meta} all have a main sensitivity index and/or inter-

action larger than 0.05 for at least one output of interest. The sums of the sensitivity indices (bottom of each subfigure) show that most of the variance is captured by individual contributions (S_i). However, for ϵ_{sup} and ϵ_{hut} a significant contribution to the variance comes from interactions between parameters. The contribution of the parameters varies for each regulation mechanism. The influence of the metabolic parameters is mainly observed in the maximum flow and ϵ outputs. The baroreflex parameters, on the other hand, are of more importance for the variance in baseline flow in the tilted position and the ϵ in tilted position. The parameters describing the myogenic mechanism and Laplace law are present in all outputs of interest.

Post sensitivity analysis

The important parameters identified though the sensitivity analysis were used to perform two sets of simulations: (1) varying all parameters with $S_T > 0.05$ ($k = 8$) and (2) varying all parameters with $S_T > 0.10$ ($k = 4$). The flow response in both the supine and tilted positions together with the distribution of the input parameters is shown in Figure 4.8. Both sets of simulations are divided into four subsets: (1) the simulations that converged (light gray) (2) the simulations that had a flow response within the standard deviation of the *in vivo* fit (middle gray) (3) the simulation that had a flow response within half a standard deviation (dark gray) and (4) the 10 simulations which best matched the mean *in vivo* response (colors).

For the first set of 4000 simulations ($S_T > 0.05$) 1610 of the 3880 (41%) converged simulations had a flow response within one standard deviation of the *in vivo* response (mid gray in Figure 4.8AC). Taking only half the standard deviation into account only 385 (10%) simulations remained (dark gray). In Figure 4.8E it can be observed that all values of the input parameters can result in a flow response within the *in vivo* uncertainty, because the light gray area covers the whole input space. However, some combinations never occur; e.g. G_{myo} and G_{meta} never have their maximum value simultaneously. When considering the simulations within half a standard deviation, a decrease in the input range of G_{myo} is observed (Figure 4.8E). The ten best simulations closely match the mean *in vivo* response in both positions (Figure 4.8AC). The distribution of the input parameters is more spread over the input domain once the importance of the parameter decreases (parameter importance decreases from left to right). Whereas the most important parameter G_{myo} has relative values between 0.10 and 0.27, values of the less important parameters, $C_{\text{v,CO}_2,0}$, $C_{\text{a,CO}_2,0}$ and τ_{myo}, cover the full input domain.

In the second set of 2000 simulations ($S_T > 0.10$) 1104 out of 1961 (56%) converged simulations showed a flow response within the *in vivo* uncertainty (mid gray in Figure 4.8BD). Considering only half a standard deviation results in only 277 (14%) simulations. Similar to the larger set of simulations, the input parameters of the

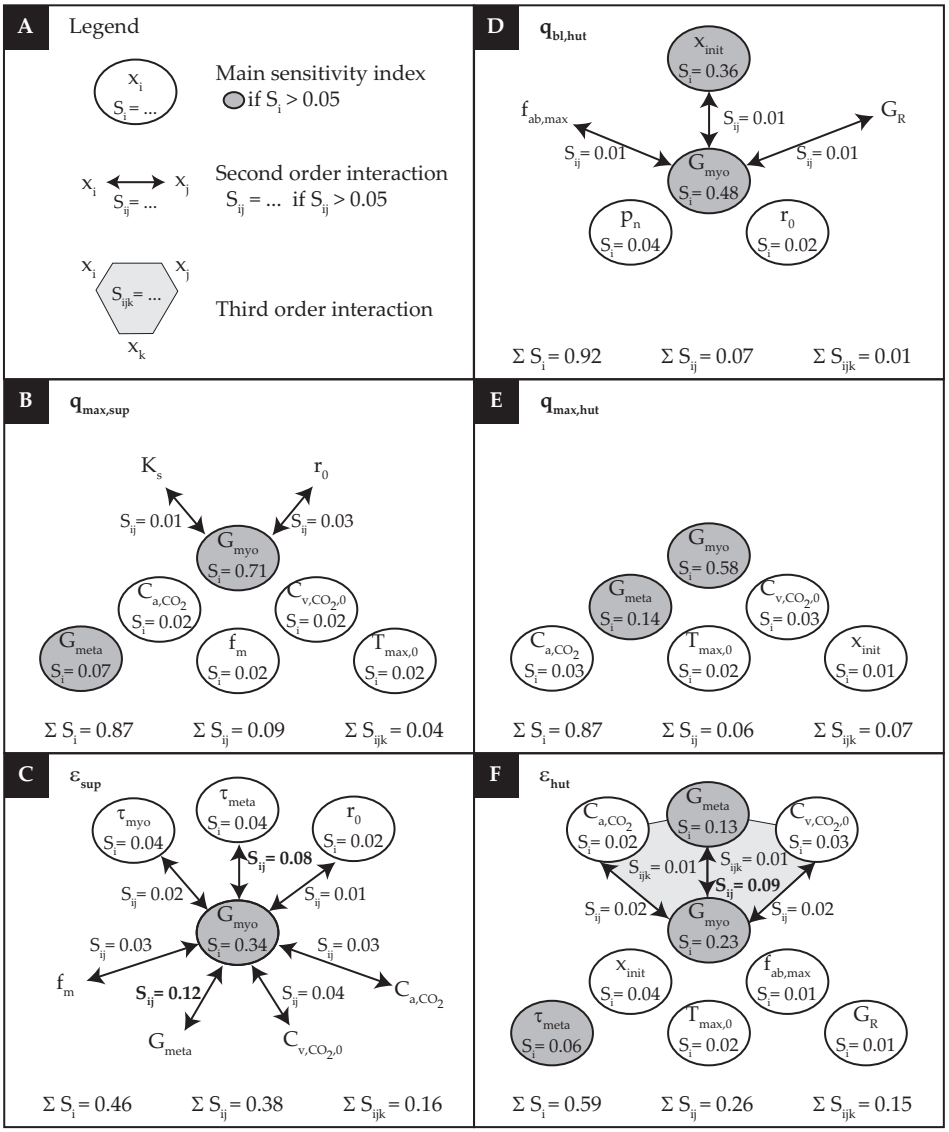

Figure 4.7: Results of the sensitivity analysis for all the outputs of interest: **B** $q_{\text{max,sup}}$, **C** $rmsq_{\text{sup}}$, **D** $q_{\text{bl,hut}}$, **E** $q_{\text{max,hut}}$ and **F** $rmsq_{\text{hut}}$. The main sensitivity index is visualised in a circle, the second order interaction with an arrow and the third order interaction with an area. For clarity only the contributions larger than 1% are shown. The most important parameters and interactions (with a contribution more than 5%) are highlighted with a gray background or bold font respectively. The sum of the main sensitivity indices, the sum of the second order interactions and the sum of the third order interactions are shown at the bottom of each subfigure.

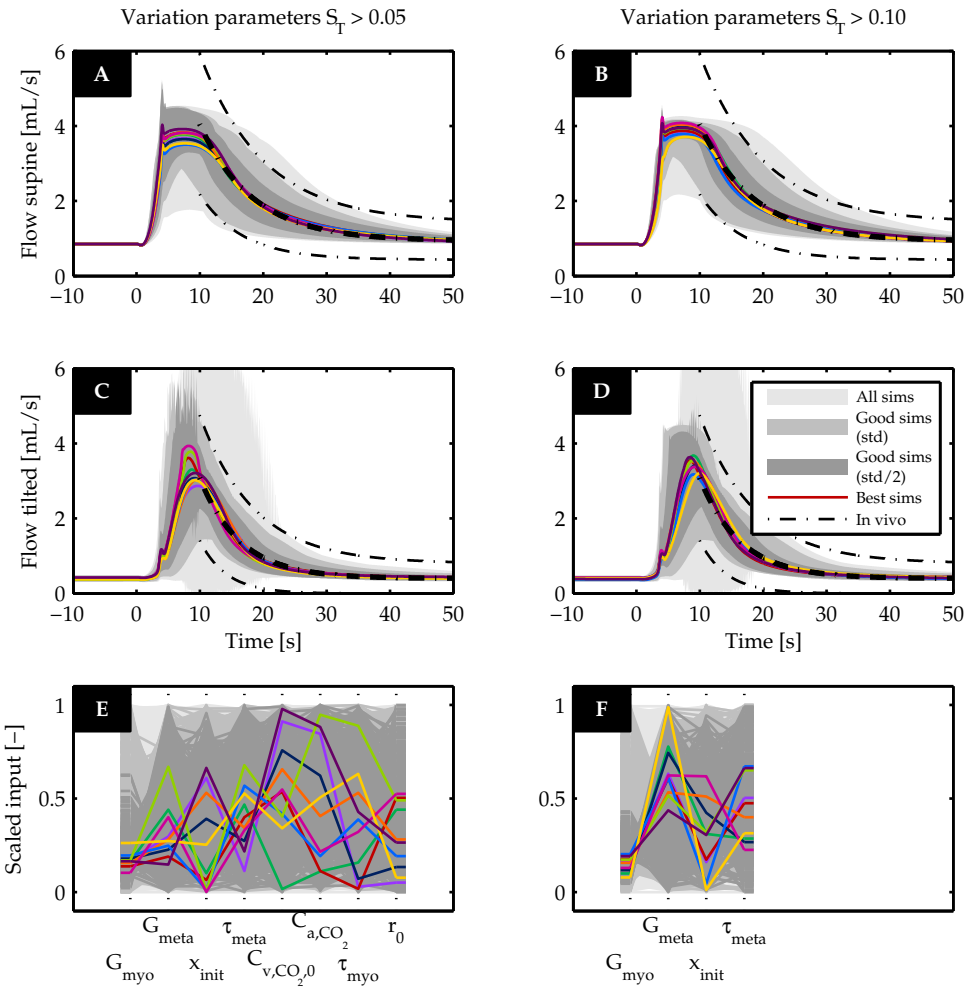

Figure 4.8: Post sensitivity analysis. The flow response of additional simulations varying the input parameters with $S_T > 0.05$ (left column) and $S_T > 0.10$ (right column) in both supine (**AB**) and tilted position (**CD**). For both sets the good simulations (present within one standard deviation and half the standard deviation) are presented in dark gray and the best 10 simulations in color. In the bottom plots (**EF**) the distribution of the corresponding input parameter is shown.

good simulations (within one standard deviation) had values within their whole uncertainty range (mid gray Figure 4.8F). Again, not all combinations were present, especially at the lower and upper limits of the domains. For the subset within half a standard deviation a decrease in input range of G_{myo} is observed as for the first set of simulations. Although the value of ϵ_{sup} and ϵ_{hut} slightly increased (same order of magnitude), the 10 best simulations still closely matched the *in vivo* fit. However, now the values of G_{meta} show a stronger correlation with the values of G_{myo}, which is in line with the high values found in the sensitivity analysis for the interaction between G_{myo} and G_{meta}. Furthermore, the range of G_{meta} has shifted to the upper part of the domain, which indicates G_{meta} could be fixed within this range to obtain a good fit.

4.4 Discussion

The flow augmentation observed at the onset of exercise is hypothesized to be a result of the muscle pump effect, the regulation of vascular tone or a combination of both. In Chapter 2, we showed that the muscle pump effect alone cannot induce the flow increase observed *in vivo*. Therefore, in the current study the importance of the major mechanisms regulating blood flow during the different phases of a muscle contraction has been investigated in both the supine and tilted position. To investigate these effects the arterio-venous 1D pulse wave propagation model of Chapter 2 has been extended with a regulation model accounting for baroreflex, metabolic and myogenic regulation. Model parameters were either taken from literature or determined by fitting the simulated arterial flow response to the measured *in vivo* response to a muscle contraction in the supine position. The model was then validated by comparing simulated results with the *in vivo* measurements in the tilted position without changing the parameter values obtained from the fit in the supine position. Furthermore, a sensitivity analysis has been performed to quantify the importance of the input parameters in the regulation model.

The model was able to capture the *in vivo* response in the supine position when only optimizing the values of the myogenic and metabolic gain (Figure 4.5C). When the same parameters were used to simulate a muscle contraction in the tilted position, again good agreement was found (Figure 4.5D). The model response replicates two of the main features of flow variation. Firstly, it matches the flow decay back to baseline after the vasodilation is initiated following muscle contraction. Secondly, the model captures the decreased baseline flow in the tilted position observed *in vivo*. Examining the activation of the various regulation mechanisms, the metabolic mechanism is the main vasodilator after muscle contraction in both the supine and tilted position, which is in line with *in vivo* studies (Nådland et al., 2009; Tschakovsky and

Sheriff, 2004). Furthermore, these simulations support the hypothesis of Nådland et al. (2009) that the decrease in baseline flow in the tilted position is a result of the global baroreflex and local myogenic activation. The latter is a result of the decreased carotid pressure and increased arteriolar pressure respectively.

The influence of the variation in systemic pressure via the baroreflex mechanism and the boundary conditions of the model is assessed and is most clearly observed within the first $10\ s$ after the onset of muscle contraction (Figure 4.6). The lack of reliable *in vivo* data shortly after muscle contraction, does not allow any conclusions to be drawn on which implementation is closest to physiology. The relatively small effect during the remaining part of the response ($t > 10$s) can be explained by the fact that most of the variation in systemic pressure is present shortly after muscle contraction. In the *in vivo* study of Nådland et al. (2009) it was stated that the systemic pressure reduction was too small to have an effect on femoral artery flow. However, based on the combination of the current model results and *in vivo* measurements this statement can neither be confirmed nor rejected. Because the current study focusses on the flow decay after muscle contraction and the baseline flow, which are both hardly affected, the systemic pressure variation is not expected to have a large influence on the results.

Based on the sensitivity analysis, the spread in myogenic gain G_{myo} is clearly the most important parameter (both individually and through interactions) of the regulation model for variance in the simulated flow response to muscle contraction (Figure 4.7). The uncertainty in metabolic gain G_{meta} also has a significant contribution to the output variance. The importance of both gains was expected, because they determine the magnitude of vasodilation. Furthermore, it confirms the choice to vary G_{myo} and G_{meta} in the first analysis. The fact that G_{myo} is more important than G_{meta} may be a result of the sigmoid function (Equation (B.7)) that is applied to the total regulation state. Even a small myogenic activation (i.e. vasoconstriction) will shift the total regulation towards the more sensitive part of the regulation curve. A third important parameter is x_{init}, which is the offset of the regulation state. A change in x_{init} can shift the regulatory response to a less or more sensitive region of the regulation curve. This explains the large importance of x_{init} for $q_{\text{bl,hut}}$. The fourth important parameter is the metabolic time-constant τ_{meta}, which is logically important for both ϵ outputs. The fact that the metabolic parameters dominate the ϵ output is logical, because the metabolic activation was concluded to be the main vasodilator after muscle contraction. The baroreflex is almost inactive in the supine position, which is confirmed by the fact that the baroreflex parameters are not present for the supine outputs. Whilst the current model may seem complex, the large contribution of the higher order terms (S_{ij} and S_{ijk} in Figure 4.7) indicates the need of all parameter interactions in capturing the complex physiology of the system and thereby that the

model is not too complex.

In the post sensitivity analysis it was concluded that even when only varying the 4 most important parameters (contributing more than 10%), it was still possible to find simulations that strongly resemble the *in vivo* response. The small range found for G_{myo} for the 10 best fits confirms the importance of G_{myo}. Furthermore, the interaction between G_{myo} and G_{meta} was also confirmed, because high values of the two parameters never occur simultaneously. Examining the relation between G_{myo} and G_{meta} for the 10 best fits, even suggests defining a relation between the two. The large spread of input parameters observed for the subset of simulations within the measurement uncertainty, could indicate that the whole input space is not covered. However, analysing the simulations with a flow response within half a standard deviation indicates that if one could reduce the measurement uncertainty, the input space of the most important parameter G_{myo} could be decreased.

To model the regulation of vascular tone a general approach is taken using the mean arteriolar radius as a measure for the regulatory state, because the explicit representation of individual arterioles was not of interest in the current study. Metabolic regulation was included based on a single metabolite, whereas many metabolites are known to act as vasodilator and no single metabolite has been shown to account for the full vasodilatory response (Joyner and Casey, 2015). However, the current implementation is in good agreement with the *in vivo* response, which indicates that the tissue CO_2-concentration is a good surrogate for the general metabolic response. For a correct myogenic activation an accurate pressure level is necessary. As only the calf circulation is included in the 1D part, the hydrostatic column applied to the pressure boundary condition might be overestimated, especially on the venous side. This could be overcome if the proximal vasculature would also be included in the 1D part of the model. However, as the current model is able to accurately match the *in vivo* response, it is concluded that the current model contains sufficient detail to capture the flow response after muscle contraction.

For validation of the developed model, *in vivo* ultrasound measurements were performed capturing the flow response to a calf muscle contraction in both the supine and tilted positions (Figure 4.3B). Measured baseline flow in the supine position was observed to be 2.3 times higher than in the 70° head up tilt position (Table 4.3), which is in line with the flow decrease observed by Nådland et al. (2009) in the 30° head up tilt position. Flow changes observed following muscle contraction reach peak flow within $10\ s$ followed by a decay back to baseline within a further minute. This is in accordance with the changes observed by Tschakovsky et al. (1996) following a single forearm contraction and those observed by Wesche (1986) following quadriceps contraction. Although the general flow response is in accordance with previous *in vivo* studies, the first $10\ s$ after the onset of muscle contraction are excluded from the

validation, because this part of the measurement is less accurate due to measurement difficulties during and shortly after muscle contraction. Improved measurements are necessary for validation of the simulated flow response in the first $10\ s$ after muscle contraction, which could possible be obtained by fixing the ultrasound probe to the subject.

The quality of the metamodel, captured in the coefficient of determination ($1 - R^2$), was observed to be lower for the outputs ϵ_{sup} and ϵ_{hut}. Because both outputs cover a time range of $40\ s$, they include more information, which is more likely to be hard to capture in a metamodel. Furthermore, these results could be due to the fact that the importance of the parameters excluded by the Morris screening was underestimated. However, the post sensitivity analysis shows that even when varying only the four most important parameters the model is capable to capture the flow response to a muscle contraction. Another more likely reason is that the variance that could not be captured by the metamodel is a result of the high frequency vibrations present in some simulations, because the ϵ outputs are affected most by these instabilities. Further research is needed to improve model stability. However, the values of the coefficient of determination are still acceptable and are not expected to influence the results.

This study has described how the developed model can be used to study the regulation of vascular tone in healthy individuals under muscle contraction. However, this model has potential application in the study of chronic venous disease. Extending the current model with regurgitating valves (Mynard et al., 2012) or valve prolapse (Pant et al., 2015), would allow examination of valve dynamics and hemodynamics in the presence of disease. Furthermore, the model could be used to simulate the effect of multiple contractions, as studied by Simakov et al. (2013), or even exercise. For the latter application, an extension of the model to the full circulation (Müller and Toro, 2014; Mynard and Smolich, 2015) is needed to account for venous return and baroreflex regulation of heart rate and heart contractility. This would also improve the model with a better representation of the full hydrostatic column.

4.5 Conclusion

A 1D pulse wave propagation model was developed including the baroreflex, metabolic and myogenic regulation, which enables the simulation of the flow response to a muscle contraction. In addition to the model presented in Chapter 2, which considered only the mechanical effect of a muscle contraction (muscle pump), we added a regulation model and now the simulated flow response accurately mimicks the *in vivo* measurements in both the supine and tilted positions. This confirms the hypothesis that regulation of peripheral resistance is an important mechanism inducing the

flow increase at the onset of exercise. From the activation of the regulatory mechanisms it is concluded that (1) metabolic activation is the main vasodilator after muscle contraction and (2) baroreflex and myogenic activation are responsible for the decrease in baseline flow in the tilted position. The sensitivity analysis confirmed G_{myo} as the most important parameter.

Chapter 5

Full circulation

A manuscript based on this chapter is being prepared.

5.1 Introduction

Orthostatic intolerance is often observed in patients with spinal chord injury (Claydon et al., 2006), post-flight in astronauts (Buckey et al., 1996) and is related to aging (Rutan et al., 1992). People suffering from orthostatic intolerance are unable to compensate for gravity-induced blood pooling in the lower extremity in the upright position, which may result in critical events, such as syncope. In healthy subjects activation of the calf muscle pump and the baroreflex are two important compensatory mechanisms. The muscle pump induces an increase in venous return by squeezing the deep veins under muscle contraction. The baroreflex aims for maintaining mean arterial pressure by increasing heart rate, contractility and peripheral resistance. However, many mechanistic questions remain on the contribution of the individual mechanisms and their interactions. Increased insight in these mechanisms and their interactions can improve the understanding of orthostatic intolerance.

Mathematical models of the cardiovascular system based on physical laws and physiological principles can be used to quantitatively predict hemodynamics. In the past, these mathematical models have already proven to be able to aid understanding of cardiovascular physiology (Boileau et al., 2015; van de Vosse and Stergiopulos, 2011). Studies developing mathematical models to investigate the hemodynamic response to orthostatic stress are scarce and are often based on 0D lumped parameter models. The simplicity of this type of models makes them ideal to include the full circulation and examine global effects. Therefore, 0D models are often used to investigate the baroreflex response under head up tilt (Heldt et al., 2002; Lim et al., 2013; Olufsen et al., 2005). However, studying more local mechanisms such as the muscle pump effect and the venous valve dynamics, requires more spatial details to enable inclusion of venous valves and a continuous gravitational force. Therefore, a 1D pulse wave propagation model might be more appropriate. In the previous chapters, a 1D pulse wave propagation model of the calf circulation was presented to examine the local hemodynamic response to a muscle contraction. However, to assess global blood volume shifts in response to orthostatic stress an extension to the full circulation is needed. Although the 1D pulse wave propagation model is often applied to study the arterial hemodynamics, only few studies exist that model the hemodynamics in the full circulation (Müller and Toro, 2014; Mynard and Smolich, 2015). However, to our knowledge, no 1D model of the full circulation exists that includes gravitational acceleration, although it is needed when modeling the volume shifts in the upright position.

Apart from the inclusion of gravitational acceleration, it is also essential to model the correct distribution of blood volume when studying blood volume shifts. In the human body, most of the volume is present in the smaller vessels ($r < 1$ mm) (Boron and Boulpaep, 2003). Vessels with this caliber are often lumped in a 0D model of the

whole micro-circulation (i.e. arterioles, capillaries and venules) and then coupled to a 1D pulse wave propagation model of the large arteries. The micro-circulation is then represented by a combination of resistances, compliances and eventually inertances. These parameters are often chosen such that (1) the correct mean arterial flow is obtained (by matching total resistance); (2) high frequency reflections are minimized at the transition from the 1D to 0D segments (characteristic impedance connecting vessel); and (3) the pressure wave has physiologic time decay characteristics (set compliance to obtain a correct RC-time). However, these restrictions do not define the volume distribution over the various micro-circulations and also not within the micro-circulation itself (i.e. arteriolar, capillary and venular level). For the current application a micro-circulation model is required that allows to distribute the volume over the various tissues and to distribute the volume within the tissue over the three components: arteriolar, capillary and venular.

Moreover, such a compartmental approach allows future inclusion of regulation of vascular tone and filtration at the capillary level. In response to orthostatic stress the baroreflex will induce vasoconstriction of the arterioles in order to maintain mean arterial pressure. Furthermore, filtration will take place at the capillary level, which becomes important during prolonged orthostatic stress.

In this study, we aim to develop a full circulation pulse wave propagation model coupled to a three compartment micro-circulation model, that allows for analysing the blood volume shifts under head up tilt. For this, the arterial and venous 1D pulse wave propagation model presented in Chapter 2 is extended to the full circulation and heart dynamics and the pulmonary circulation are added based on Bovendeerd et al. (2006) and Cox et al. (2009) respectively. Furthermore, a new micro-circulation model is presented enabling to define the blood volume distribution, while maintaining the capacity to obtain the correct flow distribution and minimize high frequency reflections at both the arterial and venous transition to the micro-circulation. Furthermore, the micro-circulation will be split into three compartments to also capture the volume distribution over the arterioles, capillaries and venules. Although it is not the aim of the current study, this three-compartments structure also facilitates future inclusion of e.g. arteriolar vasoconstriction or capillary filtration.

5.2 Methods

5.2.1 Model

To study the blood volume shift under head up tilt, a mathematical model of the full circulation is built (Figure 5.1). The model includes a 0D single fiber heart model (Arts et al., 1991), 0D versatile heart valves (Mynard et al., 2012), a 1D pulse

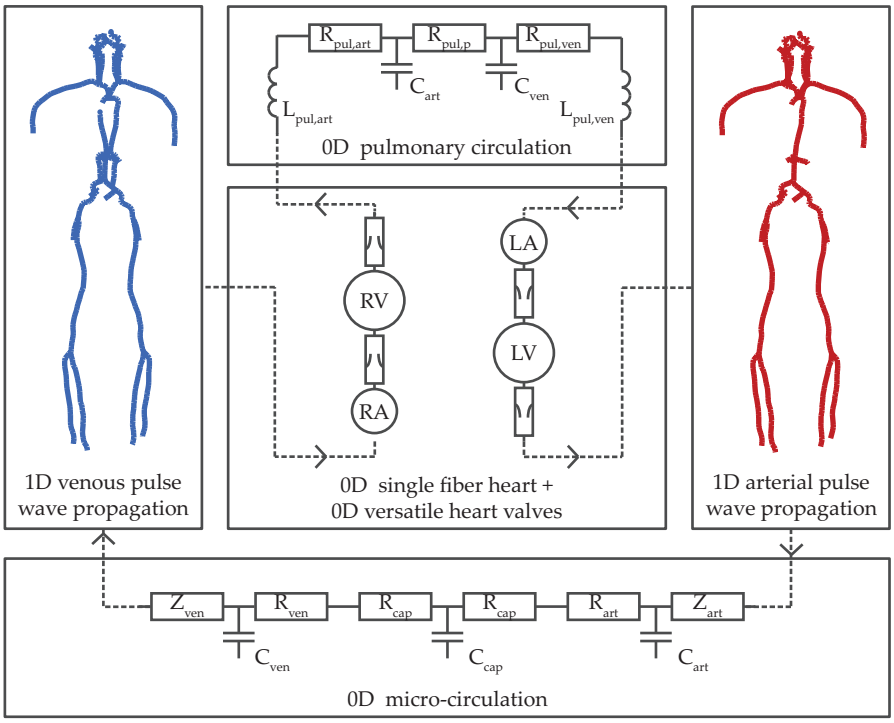

Figure 5.1: Schematic model configuration including: 0D single fiber heart model, 0D versatile heart valves, 1D arterial and venous pulse wave propagation model, 0D micro-circulation and 0D pulmonary circulation. The shown 0D micro-circulation model represents the triple windkessel model. A description of the different model parameters is given in Table 5.1.

wave propagation model for the large systemic arteries and veins (Chapter 2), a 0D pulmonary circulation (Cox et al., 2009) and a 0D model for the systemic micro-circulation. For the systemic micro-circulation two types are presented: the traditional single windkessel and the new three-compartment windkessel specifically designed for our application. In the following sections, the governing equations of the various model parts are described and the model parameters are given in Table 5.1.

Table 5.1: Model parameters: baseline value and description are given.

Symbol	Value	Unit	Description
σ_{a0}	155	kPa	Sarcomere stress in reference state
$l_{s,a0}$	1.5	μm	Sarcomere length below which active stress is zero (Bovendeerd et al., 2006)
$l_{s,ar}$	2.0	μm	Sarcomere length in reference state (Bovendeerd et al., 2006)
τ_r	150	ms	Reference rise time constant (van der Hout-van der Jagt et al., 2012)

Table 5.1 – continued from previous page

Symbol	Value	Unit	Description
τ_{d}	250	ms	Reference decay time constant (van der Hout-van der Jagt et al., 2012)
a_{r}	100	s/mm	Constant defining sarcomere length dependency of time rise constant (van der Hout-van der Jagt et al., 2012)
a_{d}	400	s/mm	Constant defining sarcomere length dependency of time decay constant (van der Hout-van der Jagt et al., 2012)
v_0	10	μm s^{-1}	Unloaded sarcomere shortening velocity (Bovendeerd et al., 2006)
σ_{f0}	900	Pa	Passive stress in fiber direction at zero stretch (Bovendeerd et al., 2006)
σ_{r0}	200	Pa	Passive stress in radial direction at zero stretch (Bovendeerd et al., 2006)
c_{f}	12	-	Constant defining shape of passive stress, stretch relation in fiber direction (Bovendeerd et al., 2006)
c_{r}	9	-	Constant defining shape of passive stress, stretch relation in radial direction (Bovendeerd et al., 2006)
ρ	1050	kg m^{-3}	Blood density (Kenner, 1989)
g	9.81	m s^{-2}	Magnitude of gravitational acceleration on earth
$p_{\mathrm{ref,A}}$	12.7	kPa	Reference pressure arterial constitutive law
A_0^+	1.37	-	Fitting constant (Chapter 2)
p_a^+	-2.53	-	Fitting constant (Chapter 2)
p_b^+	3.02	-	Fitting constant (Chapter 2)
B	0.108	-	Fitting constant (Chapter 2)
A_0^-	1.28	-	Fitting constant (Chapter 2)
p_a^-	-1.49	-	Fitting constant (Chapter 2)
p_b^-	2.03	-	Fitting constant (Chapter 2)
γ	4	-	Fitting constant (Chapter 2)
$K_{\mathrm{p,min}}$	0.5	kPa	Minimal bending stiffness
$K_{\mathrm{p,max}}$	2.0	kPa	Maximal bending stiffness
η	4.5	mPa s	Dynamic blood viscosity (Letcher et al., 1981)
$A_{\mathrm{eff,min}}$	$1{\cdot}10^{-20}$	m^2	Minimal valve opening area
$dp_{\mathrm{valve,0}}$	0	Pa	Valvular pressure drop at which opening/closing is initiated (Mynard and Smolich, 2015)
β_{art}	0.6875	-	Part of pressure drop within arterioles (Boron and Boulpaep, 2003)
β_{cap}	0.1875	-	Part of pressure drop within capillaries (Boron and Boulpaep, 2003)
β_{ven}	0.1250	-	Part of pressure drop within venules (Boron and Boulpaep, 2003)
γ_{art}	0.133	-	Part of volume within arterioles (Boron and Boulpaep, 2003)
γ_{cap}	0.1	-	Part of volume within capillaries (Boron and Boulpaep, 2003)
γ_{ven}	0.767	-	Part of volume within venules (Boron and Boulpaep, 2003)
V_{tot}	3.0	L	Total amount of blood volume within the systemic micro-circulation (Boron and Boulpaep, 2003)
$R_{\mathrm{pul,a}}$	2.5	MPa s/m^{-3}	Arterial pulmonary resistance (Cox et al., 2009)

Table 5.1 – continued from previous page

Symbol	Value	Unit	Description
$L_{\text{pul,a}}$	12	kPa s^2/m^{-3}	Arterial pulmonary inertia (Cox et al., 2009)
$C_{\text{pul,a}}$	65	mm^{-3}/Pa	Arterial pulmonary compliance (Cox et al., 2009)
$R_{\text{pul,p}}$	14	MPa s/m^{-3}	Peripheral pulmonary resistance(Cox et al., 2009)
$R_{\text{pul,v}}$	2.5	MPa s/m^{-3}	Venous pulmonary resistance(Cox et al., 2009)
$L_{\text{pul,v}}$	12	kPa s^2/m^{-3}	Venous pulmonary inertance(Cox et al., 2009)
$C_{\text{pul,v}}$	310	mm^{-3}/Pa	Venous pulmonary compliance(Cox et al., 2009)

0D Single fiber model: heart

To include the pumping function of the heart, the wall mechanics of all cardiac cavities is captured using the single fiber model as developed by Arts et al. (1991) and Bovendeerd et al. (2006). This model relates the local sarcomere stresses and stretches to the global cavity pressure p_{cav} and volume V_{cav}.

$$p_{\text{cav}} = \frac{1}{3}(\sigma_{\text{f}} - 2\sigma_{\text{r,p}}) \ln\left(1 + \frac{V_{\text{cav,W}}}{V_{\text{cav}}}\right), \tag{5.1}$$

where $V_{\text{cav,W}}$ is the wall volume of the cavity, $\sigma_{\text{p,r}}$ is the passive stress in radial direction and $\sigma_{\text{f}} = \sigma_{\text{f,a}} + \sigma_{\text{f,p}}$ is the fiber stress, which is the sum of an active $\sigma_{\text{f,a}}$ and a passive $\sigma_{\text{f,p}}$ component. The active fiber stress is modeled to depend on contractility c, sarcomere length l_{s}, time elapsed since activation t_{a} and sarcomere shortening velocity $v_{\text{s}}(= -\dot{l_{\text{s}}})$ based on Bovendeerd et al. (2006) and van der Hout-van der Jagt et al. (2012):

$$\sigma_{\text{f,a}} = \sigma_{\text{ar}} \cdot c \cdot f(l_{\text{s}}) \cdot g(l_{\text{s}}, t_{\text{a}}) \cdot h(v_{\text{s}}) \tag{5.2}$$

where $f(l_{\text{s}})$ depends on sarcomere length l_{s} via:

$$f(l_{\text{s}}) = \begin{cases} 0 & l_{\text{s}} \leq l_{\text{s,a0}} \\ \frac{l_{\text{s}} - l_{\text{s,a0}}}{l_{\text{s,ar}} - l_{\text{s,a0}}} & l_{\text{s}} > l_{\text{s,a0}} \end{cases}, \tag{5.3}$$

where $l_{\text{s,a0}}$ is the sarcomere length below which active stress equals zero, $l_{\text{s,ar}}$ is the sarcomere length in the reference state with corresponding reference stress σ_{ar}. Secondly, $g(l_{\text{s}}, t_{\text{a}})$ is defined to depend on l_{s} and t_{a}:

$$g(l_{\text{s}}, t_{\text{a}}) = \begin{cases} 0 & t_{\text{a}} < 0 \\ \sin(\frac{\pi t_{\text{a}}}{2\tau_{\text{r}}}) & 0 \leq t_{\text{a}} < \tau_{\text{r}} \\ 1 - \sin(\frac{\pi(t_{\text{a}} - \tau_{\text{r}})}{2\tau_{\text{d}}}) & \tau_{\text{r}} \leq t_{\text{a}} < \tau_{\text{r}} + \tau_{\text{d}} \\ 0 & t_{\text{a}} \geq \tau_{\text{r}} + \tau_{\text{d}} \end{cases}, \tag{5.4}$$

where rise τ_{r} and decay τ_{d} time constants are defined according to van der Hout-van der Jagt et al. (2012):

$$\tau_{\text{r}} = \tau_{\text{r1}} + a_{\text{r}}(l_{\text{s}} - l_{\text{s,0}}) \qquad \text{and} \qquad \tau_{\text{d}} = \tau_{\text{d1}} + a_{\text{d}}(l_{\text{s}} - l_{\text{s,0}}) \tag{5.5}$$

Table 5.2: Parameters single fiber heart model.

		LA	LV	RA	RV
$V_{\text{cav,W}}$	mL	10	230	10	80
$V_{\text{cav,0}}$	mL	35	50	35	60
c	-	0.7	1.0	0.7	0.5

where τ_{r1} and τ_{d1} are the reference rise and decay time constants respectively. a_{r} and a_{d} define the length dependency. Finally, the dependency on v_{s} is captured with $h(v_{\text{s}})$ as follows:

$$h(v_{\text{s}}) = 1 - v_{\text{s}}/v_0, \tag{5.6}$$

where v_0 is the unloaded sarcomere shortening velocity. Passive stress in fiber and radial direction are defined with the following relations:

$$\sigma_{\text{f,p}}(\lambda_{\text{f}}) = \begin{cases} \sigma_{\text{f0}}(e^{c_{\text{f}}(\lambda_{\text{f}}-1)} - 1) & \lambda_{\text{f}} \geq 0 \\ 0 & \lambda_{\text{f}} < 0 \end{cases}, \tag{5.7}$$

$$\sigma_{\text{r,p}}(\lambda_{\text{r}}) = \begin{cases} \sigma_{\text{r0}}(e^{c_{\text{r}}(\lambda_{\text{r}}-1)} - 1) & \lambda_{\text{r}} \geq 0 \\ 0 & \lambda_{\text{r}} < 0 \end{cases}, \tag{5.8}$$

where σ_{f0} and σ_{r0} are the passive stress at zero stretch in fiber and radial direction, and c_{f} and c_{r} are constants defining the shape of the relation. The stretch in fiber λ_{f} and radial λ_{r} direction are defined to depend on cavity volume according to:

$$\lambda_{\text{f}} = \left(\frac{V_{\text{cav}} + \frac{1}{3}V_{\text{cav,W}}}{V_{\text{cav,0}} + \frac{1}{3}V_{\text{cav,W}}} \right)^{\frac{1}{3}} \qquad \text{and} \qquad \lambda_{\text{r}} = \lambda_{\text{f}}^{-2}, \tag{5.9}$$

where $V_{\text{cav,0}}$ is the cavity volume at zero transmural pressure. To differentiate between the various cavities, wall volume $V_{\text{cav,W}}$ and zero pressure volume $V_{\text{cav,0}}$ are defined per cavity (Table 5.2). Furthermore, contractility c is adapted to account for the less efficient contraction of the atria and right ventricle relative to the left ventricle (Table 5.2).

1D Pulse wave propagation: arteries and veins

The hemodynamics in the large arteries and veins are captured using the 1D equation of mass and momentum balance. To account for the hydrostatic pressure arising upon a head up tilt, gravitational acceleration is included in the momentum balance:

$$C\frac{\partial p_{tr}}{\partial t} + \frac{\partial q}{\partial z} = 0, \tag{5.10}$$

$$\frac{\partial q}{\partial t} + \frac{\partial A\overline{v_z^2}}{\partial z} + \frac{A}{\rho}\frac{\partial p}{\partial z} = \frac{2\pi a}{\rho}\tau_w + Ag_z, \tag{5.11}$$

where C is the compliance per unit length, $p_{\text{tr}} = p - p_{\text{ex}}$ is the transmural pressure, with p and p_{ex} the intra- and extravascular pressure respectively, t is the time, q is the flow and z is the axial coordinate. Furthermore, A is the cross-sectional area, $\overline{v}_z$ is the axial velocity averaged over the cross-sectional area, ρ is the density of blood, a is the radius and τ_{w} is the wall shear stress. Finally, $g_z = g\ \mathbf{e_g} \cdot \mathbf{e_z}$ is the contribution of gravity in axial direction, with g the magnitude of gravitational acceleration on earth, $\mathbf{e_g}$ the unit vector in the direction of gravity and $\mathbf{e_z}$ the unit vector in axial direction.

An estimate of the advection $\frac{\partial A\overline{v_z^2}}{\partial z}$ and wall shear stress τ_w term is derived based on the approximate velocity profile (Bessems et al., 2007). This profile assumes the inertia forces to be in balance with the pressure gradient and gravitational forces in the central core. In the viscous boundary layer, viscous forces are assumed to balance the pressure gradient and gravitational forces. At the transition from the central core to the viscous boundary layer, all forces are assumed to be in balance (for details see Bessems et al. (2007)).

To complete the system of equations a constitutive law is needed to describe the pressure area relation. Similar to the previous chapters, the small changes in arterial cross-sectional area are captured with a linear relation. The nonlinear response of the venous wall is included using the fit of the tube law of Shapiro (1977) as presented in Chapter 2. Based on *in vivo* observations (Bassez et al., 2001) and the radius-dependency described by Müller and Toro (2014), the bending stiffness K_p throughout the venous tree is defined by the following relation:

$$K_p = K_{\text{p,max}} - (K_{\text{p,max}} - K_{\text{p,min}})\frac{r - r_{\text{min}}}{r_{\text{max}} - r_{\text{min}}} \tag{5.12}$$

where r_{min} and r_{max} are the minimal and maximal radius in the venous tree, respectively, and $K_{\text{p,min}}$ and $K_{\text{p,max}}$ are the minimal and maximal values for bending stiffness.

The geometrical data of the systemic arteries and veins included in the 1D pulse wave propagation model is given in Table 5.3.

Table 5.3: Overview of the geometrical parameters of the large systemic arteries and veins included using the 1D pulse wave propagation model: l length, r_1, r_2 radii, h_1, h_2 wall thicknesss and E Young's modulus.

Vessel	l [mm]	r_1 [mm]	r_2 [mm]	h_1 [mm]	h_2 [mm]	E [MPa]
Ascending aorta	31.1	14.7	14.4	1.8	1.8	0.4
Aortic arch A	1.2	12.6	12.0	1.6	1.6	0.4
Innominate artery	42.5	10.1	9.0	1.3	1.1	0.4
R subclavian artery A	30.6	5.5	4.3	0.7	0.5	0.4
R carotid artery	100.8	6	3	0.8	0.4	0.8
R vertebral artery	230.6	1.9	1.4	0.2	0.2	0.8

Table 5.3 – continued from previous page

Vessel	l [mm]	r_1 [mm]	r_2 [mm]	h_1 [mm]	h_2 [mm]	E [MPa]
R subclavian artery B	301.6	4.1	2.4	0.5	0.3	0.4
R internal carotid artery	120.8	2.4	1.5	0.3	0.2	0.8
R external carotid artery	50.3	2.7	2.1	0.3	0.3	0.8
Aortic arch B	10.5	10.7	10.4	1.3	1.3	0.4
L common carotid artery	130.8	6.8	3.5	0.8	0.4	0.8
L internal carotid artery	140.4	2.5	1.5	0.3	0.2	0.8
L external carotid artery	60.8	2.9	2.2	0.4	0.3	0.8
Thoracic aorta A	230.4	10	6	1.3	0.8	0.4
L subclavian artery A	50.8	5.8	4.6	0.7	0.6	0.4
L vertebral artery	230.5	1.9	1.4	0.2	0.3	0.8
L subclavian artery B	321.6	4.2	2.4	0.5	0.3	0.4
Abdominal aorta B	12.1	5.9	5.9	0.7	0.7	0.4
Superior mesenteric artery	20.4	4.0	3.6	0.5	0.4	0.4
L renal artery	51.0	2.6	2.6	0.3	0.3	0.4
R renal artery	60.8	2.6	2.6	0.3	0.3	0.4
Abdominal aorta D	0.8	5.8	5.6	0.7	0.7	0.4
Inferior mesenteric artery	21.0	2.4	1.6	0.3	0.2	0.4
Abdominal aorta E	82.6	5.2	5.2	0.7	0.7	0.4
L common iliac artery	51.0	4.0	3.5	0.5	0.4	0.4
L external iliac artery	161.0	3.2	3.1	0.4	0.4	0.8
L internal iliac artery	41.0	2.0	2.0	0.3	0.3	1.6
L femoral artery	490.9	2.6	1.9	0.3	0.2	0.8
L deep femoral artery	81.0	2.0	1.9	0.3	0.2	0.8
L posterior tibial artery	351.0	1.6	1.4	0.2	0.2	1.6
L anterior tibial artery	321.0	1.3	1.2	0.2	0.1	1.6
R common iliac artery	61.0	4.0	3.5	0.5	0.4	0.4
R external iliac artery	161.0	3.2	3.1	0.4	0.4	0.8
R internal iliac artery	51.0	2.0	2.0	0.3	0.3	1.6
R femoral artery	500.9	2.6	1.9	0.3	0.2	0.8
R deep femoral artery	81.0	2.0	1.9	0.3	0.2	0.8
R posterior tibial artery	371.0	1.6	1.4	0.2	0.2	1.6
R anterior tibial artery	331.0	1.3	1.2	0.2	0.1	1.6
Superior vena cava	31.1	8.0	8.0			
Inferior vena cava	237.0	7.6	7.6			
R Brachiocephalic vein	42.5	5.6	5.6			
L subclavian vein I	21.2	5.4	5.4			
R subclavian vein I	30.6	5.6	5.6			
L subclavian vein II	331.6	5.2	5.2			
R subclavian vein II	301.6	5.2	5.2			
L vertebral vein	225.2	1.6	1.4			
R vertebral vein	231.6	1.6	1.4			
L internal jugular vein	132.2	5.4	5.6			
R internal jugular vein	96.5	7.1	3.8			
L venous sigmoid sinus	140.4	3.9	2.2			
R venous sigmoid sinus	120.8	2.5	1.9			
L external jugular vein	60.8	1.7	1.4			
R external jugular vein	50.3	1.7	1.4			
Superior mesenteric vein	20.4	4.9	4.9			
R renal vein	60.8	2.5	2.5			
L renal vein	51.0	2.5	2.5			

Table 5.3 – continued from previous page

Vessel	l [mm]	r_1 [mm]	r_2 [mm]	h_1 [mm]	h_2 [mm]	E [MPa]
Inferior mesenteric vein	21.0	4.5	4.5			
R common iliac vein	61.0	5.8	5.8			
L common iliac vein	51.0	5.8	5.8			
R internal iliac vein	51.0	1.5	1.5			
L internal iliac vein	41.0	1.5	1.5			
R external iliac vein	161.0	5.0	5.0			
L external iliac vein	161.0	5.0	5.0			
R deep femoral vein	81.0	3.5	3.5			
L deep femoral vein	81.0	3.5	3.5			
R femoral vein	501.0	3.5	3.4			
L femoral vein	490.9	3.5	3.4			
R anterior tibial vein	351.0	1.5	1.5			
L anterior tibial vein	321.0	1.5	1.5			
R posterior tibial vein	371.0	1.5	1.5			
L posterior tibial vein	341.0	1.5	1.5			
Azygos vein	255.3	4.3	4.3			
Hemazygos vein	121.6	4.3	2.8			
Ascending lumbar vein	131.5	2.8	2.0			

0D Versatile heart valves

The hemodynamics of the heart valves are described using versatile valve model of Mynard et al. (2012). The valvular pressure drop is defined to depend on the flow via the following relation:

$$\Delta p = Bq|q| + L\frac{\partial q}{\partial t}, \tag{5.13}$$

where the Bernouilli resistance B and the inertia L are defined by the following relations:

$$B = \frac{\rho}{2A_{\text{eff}}^2} \qquad \text{and} \qquad L = \frac{\rho l_{\text{eff}}}{A_{\text{eff}}}, \tag{5.14}$$

where l_{eff} is the effective valve length. To include the valve dynamics the effective cross-sectional area A_{eff} is defined as a function of valve state ζ:

$$A_{\text{eff}} = (A_{\text{eff,max}} - A_{\text{eff,min}})\,\zeta + A_{\text{eff,min}}, \tag{5.15}$$

with $A_{\text{eff,max}}$ and $A_{\text{eff,min}}$ the maximal and minimal cross-sectional area respectively. Valve state ζ can vary between zero (=fully closed) and one (fully open), and opening and closing is defined to depend on the pressure drop over the valve via the following relations:

$$\frac{d\zeta}{dt} = \begin{cases} (1-\zeta)\,K_{\text{vo}}\,(\Delta p - dp_{\text{valve,0}})\,, & \text{for } \Delta p > dp_{\text{valve,0}} \\ \zeta K_{\text{vc}}\,(\Delta p - dp_{\text{valve,0}})\,, & \text{for } \Delta p < dp_{\text{valve,0}} \end{cases}, \tag{5.16}$$

where K_{vo} and K_{vc} are constant defining the opening and closing rate of the valve. Furthermore, $dp_{\text{valve,0}}$ is the pressure drop over the valve above and below which

Table 5.4: Heart valve parameters for the mitral valve (MV), the aortic valve (AV), the tricuspid valve (TV) and the pulmonary valve (PV) (Mynard and Smolich, 2015).

		MV	AV	TV	PV
$A_{\text{eff,max}}$	mm^2	510	490	600	570
l_{eff}	cm	2.0	1.0	2.0	1.5
K_{vo}	m s kg^{-1}	0.2	0.2	0.3	0.2
K_{vc}	m s kg^{-1}	0.2	0.2	0.4	0.4

opening and closing is initiated respectively. To capture the different dynamics of the various valves, the parameters $A_{\text{eff,max}}$, l_{eff}, K_{vo} and K_{vc} are defined per valve based on Mynard et al. (2012) (Table 5.4).

0D Pulmonary circulation

To capture the hemodynamics of the pulmonary circulation a lumped parameter model is used. Although the pulmonary hemodynamics are known to be affected by gravitational acceleration, it is not included in the current study. Similar to the study of Cox et al. (2009), arteries and veins are built up from segments including a resistance $R_{\text{pul,i}}$ and inertance $L_{\text{pul,i}}$ in series, and a compliance $C_{\text{pul,i}}$ connected to the extravascular pressure (Figure 5.1). For these elements, the following pressure flow relations hold:

$$\Delta p = R_{\text{pul,i}} q, \qquad C_{\text{pul,i}} \frac{\partial p_{\text{tr}}}{\partial t} = q \qquad \text{and} \qquad \Delta p = L_{\text{pul,i}} \frac{\partial q}{\partial t}, \tag{5.17}$$

with $i = a$ for the arterial segment and $i = v$ for the venous segment. The arterial segment is connected to a resistance $R_{\text{pul,p}}$, which represents the resistance of the pulmonary micro-circulation. The outlet of this resistance is connected to a venous segment.

0D Micro-circulation: traditional single windkessel

To capture the pressure drop over the micro-circulation and include the compliance of the peripheral vascular bed, the traditional windkessels is used as a reference model (Westerhof et al., 1969). This single windkessel model contains of two resistances in series and a compliance connected to the extravascular pressure. The sum of the resistances is chosen such that the flow through the peripheral bed i equals the mean systemic pressure drop Δp_{sys} divided by the local flow q_{i}:

$$R_{\text{tot,i}} = \frac{\Delta p_{\text{sys}}}{q_{\text{i}}}. \tag{5.18}$$

The local mean flow q_{i} is based on the distribution of the flow over the various body parts (Table 5.5) and within a body part scaled with the radius of the supplying artery

Table 5.5: Flow distribution over the various body parts (Nichols and O'Rourke, 1997).

	α_{p}
Arms	0.146
Cerebral	0.135
Splanchnic	0.250
Renal	0.198
Legs	0.271

using the following equation:

$$q_{\text{i}} = \alpha_{\text{p}} \cdot \frac{r_i^3}{\frac{1}{N_{\text{p}}} \sum_{j=1}^{N_{\text{p}}} r_j^3} \cdot q_{\text{sys}} \tag{5.19}$$

where α_{p} is the percentage of flow attributed to part p, r_i the radius of the connecting artery, N_p the number of micro-circulations within part p and q_{sys} the cardiac output. To minimize reflections at the transition from the 1D arterial to the 0D micro-circulation the first resistance is defined such to match the characteristic impedance Z_{wk} of the connecting artery. The second resistance R_{wk} contains the remaining part of the resistance.

$$R_{\text{tot,i}} = Z_{\text{wk}} + R_{\text{wk}}. \tag{5.20}$$

The compliance C_{wk} is derived based on a typical time constant τ_{RC}

$$C_{\text{wk}} = \frac{\tau_{\text{RC}}}{R_{\text{wk}}}. \tag{5.21}$$

0D Micro-circulation: three-compartment model

To capture both the blood volume present within the micro-circulation, next to the pressure drop over the micro-circulation, the traditional single windkessel model is extended to a three-compartments model including three windkessel segements. First, the micro-circulation is split into three parts: an arteriolar, a capillary and a venular part. Each part is modeled with a three-element windkessel model consisting of two resistances and a compliance connected to the extravascular pressure. The sum of the resistances is chosen such that it matches the flow through the peripheral bed as described for the traditional windkessel model. The distribution of the resistance over the three windkessels is based on the physiologically expected distribution of the pressure drop (Boron and Boulpaep, 2003). For the arteriolar part and the venular part, the resistance connected to the 1D vessels is set to match its characteristic impedance, whereas the remaining resistance is captured by R_{art} and R_{ven} respectively. The total resistance of the capillary part is equally distributed over the two resistances R_{cap}. This is summarized by the following equations:

$$\beta_{\text{art}} R_{\text{tot,i}} = Z_{\text{art}} + R_{\text{art}}, \quad \beta_{\text{cap}} R_{\text{tot,i}} = 2R_{\text{cap}}, \quad \text{and} \quad \beta_{\text{ven}} R_{\text{tot,i}} = R_{\text{ven}} + Z_{\text{ven}}, \tag{5.22}$$

where β_{art}, β_{cap} and β_{ven} are the expected fraction of the pressure drop over the arterial, capillary and venular part respectively (Boron and Boulpaep, 2003).

The compliance is derived based on the physiologically expected distribution of the volume (Nichols and O'Rourke, 1997). To determine the volume for a certain micro-circulation element, first the volume is distributed over the various body parts based on the flow distribution (Table 5.5). Second, within each bodypart volume is distributed based on the radius of the connecting vessel.

$$V_{\text{i}} = \alpha_{\text{p}} \cdot \frac{r_i^3}{\frac{1}{N_{\text{p}}} \sum_{j=1}^{N_{\text{p}}} r_j^3} \cdot V_{\text{tot}}, \tag{5.23}$$

where V_{tot} is the total volume within the micro-circulation. Within the micro-circulation, the stressed volume (i.e. 30% of total (Gelman, 2008)) is distributed over the arteriolar, capillary and venular windkessel based on literature (Boron and Boulpaep, 2003). Finally, the compliance is computed based on the pressure in the center node of the windkessel

$$C_{\text{art}} = \frac{0.3\gamma_{\text{art}} V_{\text{tot,i}}}{p_{\text{art,c}}}, \quad C_{\text{cap}} = \frac{0.3\gamma_{\text{cap}} V_{\text{tot,i}}}{p_{\text{cap,c}}}, \quad \text{and} \quad C_{\text{ven}} = \frac{0.3\gamma_{\text{ven}} V_{\text{tot,i}}}{p_{\text{ven,c}}}. \tag{5.24}$$

Automatic filling

To reach physiological pressures, additional blood volume needs to be added to the circulation model. To avoid collapse at the onset of the simulation, the initial pressure is set to 1.0 kPa throughout the whole circulation. Subsequently, $dV_{\text{fill}} = 0.1$ mL blood volume is added at every time step in the left and right ventricle, i.e. filling speed is 200 mL/s. For numerical stability, additional filling is included in the atria for the first 5 s ($dV_{\text{fill}} = 0.05$ mL). This is done without active heart contraction (i.e. $c = 0$) until the vena cava pressure reaches 1.5 kPa. Once this threshold is exceeded the heart is activated and additional volume is either removed or added every time the vena cava pressure has stabilized. The initial value of added volume is $dV_{\text{fill}} = 30$ mL for positive and $dV_{\text{fill}} = 2.5$ mL for negative filling, which is halved each time filling switches from adding to removing. This automatic filling process is continued until the vena cava pressure has stabilized to a value between 600 and 750 Pa for a period of 20 heart beats (Boron and Boulpaep, 2003).

Numerical Implementation

The model equations as described above were implemented in the finite element package SEPRAN (Ingenieursbureau SEPRA, Leidschendam, the Netherlands) based on the computational method of Kroon et al. (2012). The model of the heart and heart valves are implemented as a function. To connect the heart model to the circulation model, the flow into the atria and over the semilunar valves is prescribed as a

boundary condition in the model of the systemic and pulmonary circulation. Time discretization was implemented using the second order backward difference scheme with $\Delta t = 1$ ms and spatial discretization was implemented based on the trapezium rule with element length $\Delta z = 1$ cm. Pre- and post-processing was performed using MATLAB R2012b (MathWorks, Natick, MA, USA).

5.2.2 Simulations and analysis

To examine the blood volume shift due to orthostatic stress, two version of a full circulation model were developed: (1) including the micro-circulation based on the traditional windkessel model, and (2) including the micro-circulation based on the new three-compartment model. For both models the following hemodynamics are examined and compared to literature:

- Pressure and flow wave propagation in the systemic arteries and veins under baseline conditions (i.e. supine) and the pressures in the heart cavities and flows over the heart valves.
- Spatial pressure distribution in the systemic arteries and veins in both the supine and 70° tilted position.
- Flow and volume distribution over the various parts of the body including: cerebral, thoracic, splanchnic, renal and pulmonary circulation, and within the arms, legs and heart. The distribution is assessed in both the supine and 70° tilted position.

5.3 Results

5.3.1 Traditional single windkessel

Baseline hemodynamics

The general hemodynamics in the supine position simulated using 1D pulse wave propagation model coupled to the traditional single windkessel model can be observed in Figure 5.2. Pressure and flow waveforms are given at three venous and arterial locations as indicated in the vascular trees in the center. Furthermore, the pressure in the heart and the flow over the heart valves are given in the bottom plots.

Arterial waveforms within the large arteries show a physiological pattern where one can recognise the systolic pressure (maximum), the dicrotic notch and the di-

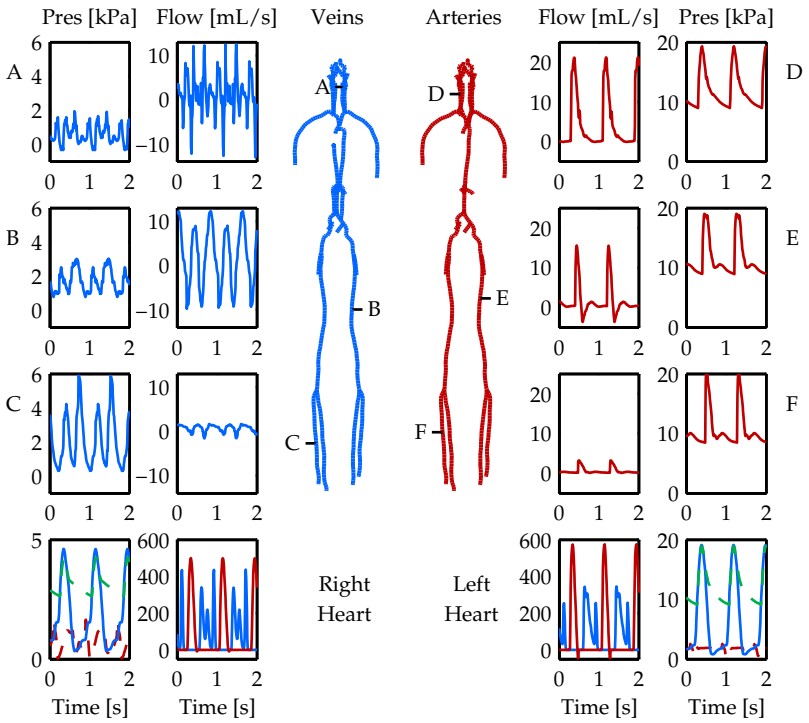

Figure 5.2: General hemodynamics obtained using the traditional single windkessel model to represent the micro-circulation. Pressure and flow waveforms are presented at three location in both the venous and arterial tree as indicated in the vasuclar trees in the center. The plot at the bottom show the pressures in the right and left heart together with the flow over the various heart valves.

astolic pressure (minimum), with a pulse pressure increasing towards the periphery. Venous wave propagation shows a biphasic pattern with physiologically relatively large pulsatility. Mean aortic pressure is equal to 12.2 kPa and systolic and diastolic pressure are 18.9 kPa and 9.1 kPa, respectively. Mean pressure in the left atrium is 1.6 kPa and 0.7 kPa in the right atrium. Mean pressure in the pulmonary artery is 3.2 kPa. Mean flow over the aortic valve is 79 mL/s and minimal and maximal flow are equal to -52 mL/s and 575 mL/s respectively. Both pulmonary and aortic valve flow show a single peak ejection with a small backflow just before valve closure. The tricuspid and mitral valve show a three-peak pattern, where the first peaks occur during passive filling of the ventricles and the last peak is a result of atrial contraction.

Spatial pressure distribution

The spatial arterial and venous pressure distribution can be observed in Figure 5.3 for both the supine (light) and tilted position (dark). Here the z-coordinate increases from the feet towards the head. In the supine position pressure is generally equal to the heart pressure (dashed line), but slightly decreased in the distal arteries and slightly increased in the distal veins. In the tilted position pressure follows the hydrostatic pressure gradient. Now, only a slight deviation is observed at the distal arteries and almost none in the veins. Although no regulation is included, pressure at the heart level remains almost equal on both the arterial and venous side of the circulation ($\Delta p_{\text{art}} = 0.4$ kPa and $\Delta p_{\text{ven}} = 0.1$ kPa).

Volume and flow distribution

The blood volume and flow distribution is presented in Figure 5.4A and B respectively. In the supine position the total of 2197 mL blood is distributed over the various parts as follows: 6% cerebral, 9% thorax, 7% arms, 8% splanchnic, 6% renal, 14% legs, 15% heart and 35% pulmonary circulation. Upon tilt the cerebral blood volume decreases by 7% (9 mL) and an increase of 15% (48 mL) is observed in the legs. The total cardiac output of 79 mL/s is distributed over the systemic circulation as follows: 15% cerebral, 15% arms, 25% splanchnic, 20% renal and 25% legs. Upon tilt cerebral blood flow decreases with 4% (0.5 mL/s) and an increase of 6% (1.1 mL/s) is observed in the legs. Although no regulation is included, only small changes in flow and volume distribution are observed.

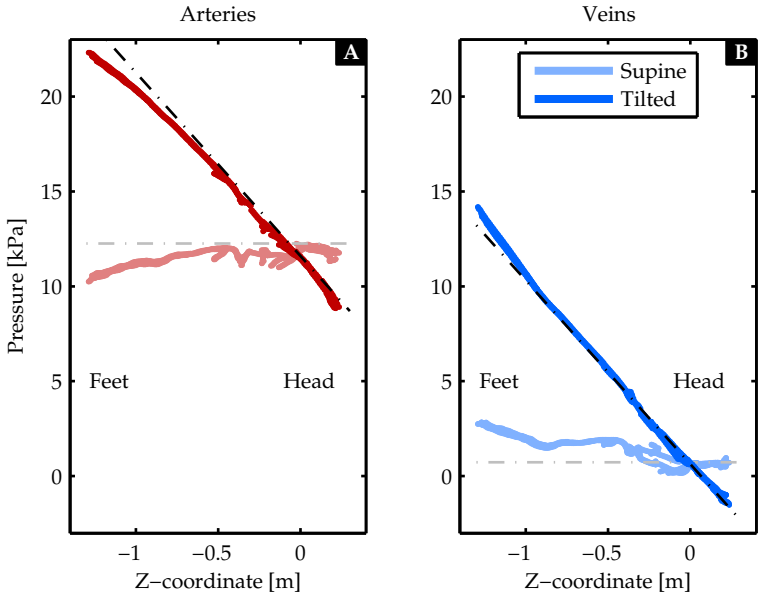

Figure 5.3: Pressure as a function of z-coordinate in the supine and tilted position, with **A** the arterial and **B** the venous systemic circulation. The horizontal dashed line represents the pressure at the heart level and the decreasing dashed line equals heart pressure plus the hydrostatic pressure. Results are obtained using the traditional single windkessel model to represent the micro-circulation.

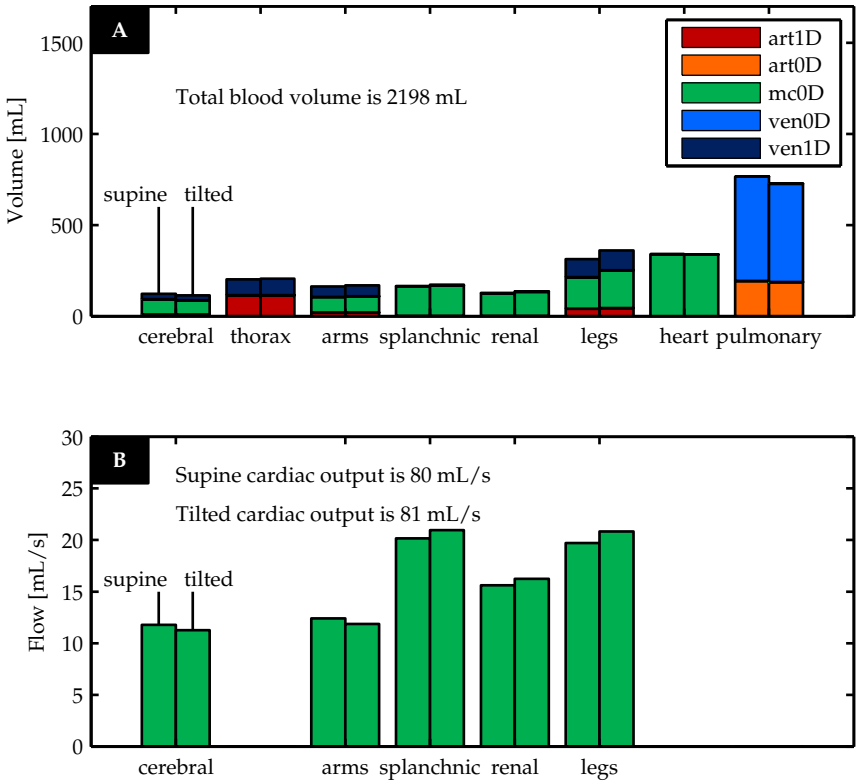

Figure 5.4: Distribution of **A** volume and **B** flow distribution in supine and tilted position using original single windkessel model to represent the micro-circulation.

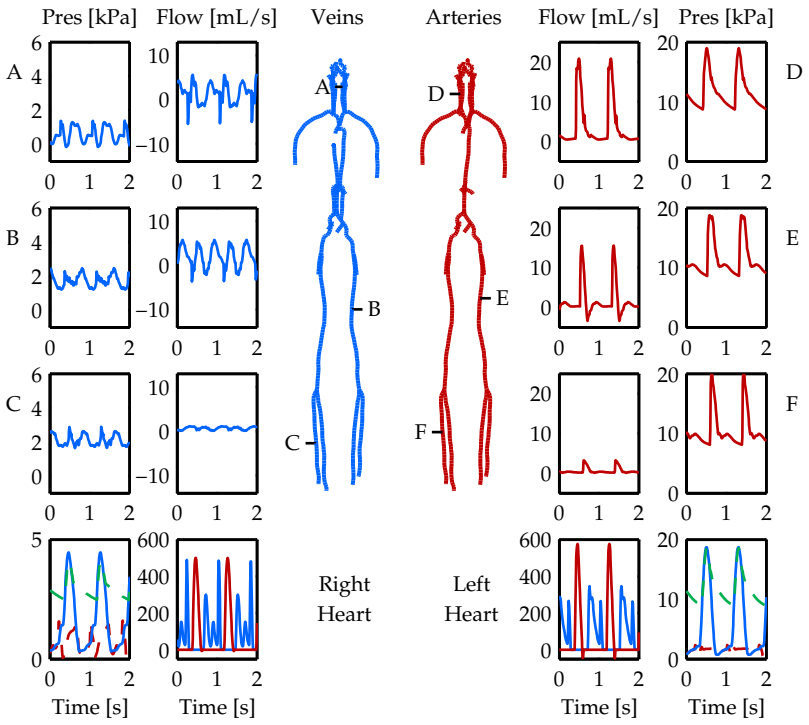

Figure 5.5: General hemodynamics obtained using the three-compartment model to represent the micro-circulation. Pressure and flow waves are presented at three location in both the venous and arterial tree as indicated in the vasuclar trees in the center. The plot at the bottom show the pressures in the right and left heart together with the flow over the various heart valves.

5.3.2 Three-compartment model

Baseline hemodynamics

The general hemodynamics in the supine position simulated using the three-compartment model to represent the micro-circulation are shown in Figure 5.5. Pressure and flow waves are given at the same three locations as presented for the single windkessel model. Furthermore, the pressures in the heart cavities and the flow over the heart valves are again given in the bottom plots.

The same typical arterial pressure and flow waveforms are observed compared to the single windkessel implementation. Venous wave propagation shows again the biphasic pattern, but the amplitude has decreased significantly. Mean arterial pressure is equal to 12.1 kPa and systolic and diastolic pressure is equal to 18.6 kPa and

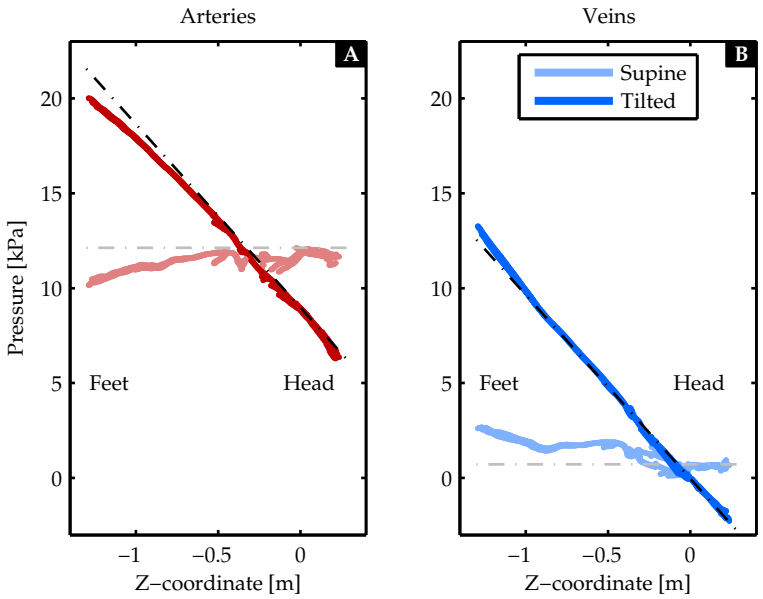

Figure 5.6: Pressure as a function of z-coordinate in the supine and tilted position, with **A** the arterial and **B** the venous systemic circulation. The horizontal dashed line represents the pressure at the heart level and the decreasing dashed line equals heart pressure plus the hydrostatic pressure. Results are obtained using the three-compartment model to represent the micro-circulation.

8.9 kPa respectively. Mean left atrial pressure have a value of 1.5 kPa and 0.7 kPa, respectively. Mean pressure in the pulmonary artery is equal to 3.0 kPa. The mean flow over the aortic valve is equal to 79 mL/s and has a maximum value of 576 mL/s and a minimal value of and −51 mL/s. Flow patterns of the heart valves are similar to those observed in the single windkessel configuration.

Spatial pressure distribution

The spatial arterial and venous pressure distribution including the three-compartment model can be observed in Figure 5.6 for both the supine (light) and tilted position (dark). The z-coordinate increases from the feet towards the head. Similar to the single windkessel, mean pressure varies hardly in the supine position both in the arteries and the veins. Furthermore, arterial and venous pressure follow the hydrostatic pressure gradient in tilted position. In contrast to the single windkessel implementation, now a large pressure drop is observed at the level of the heart: 2.9 kPa and 0.6 kPa on the arterial and venous side respectively.

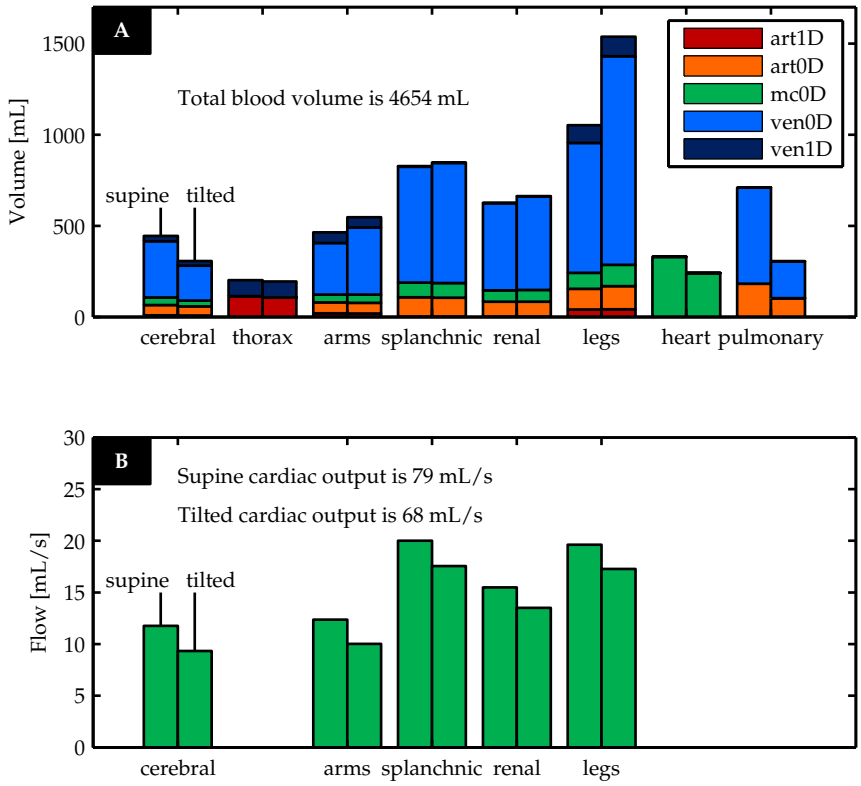

Figure 5.7: Distribution of **A** volume and **B** flow in supine and tilted position using the three-compartment model to represent the micro-circulation.

Volume and flow distribution

The volume and flow distribution obtained from the simulations including the three-compartment windkessel model to represent the micro-circulation are shown in Figure 5.4A and B respectively. In the supine position the total blood volume of 4654 mL is distributed is as follows: 10% cerebral, 4% thorax, 10% arms, 18% splanchnic, 13% renal, 23% legs, 7% heart and 15% pulmonary circulation. Cerebral blood volume decreases by 31% (138.5 mL/s) upon head up tilt and leg blood volume increases by 46% (485 mL). The flow distribution in the supine position is as follows: 15% cerebral, 15% arms, 25% splanchnic, 20% renal and 25 legs. The cerebral perfusion decreases by 21% (9.3 mL/s) and the perfusion of the legs decreases only by 12% (2.3 mL/s). Total cardiac output decreases by 15% (11.5 mL/s).

5.4 Discussion

A 1D pulse wave propagation model of the full circulation that includes a new micro-circulation element has been developed to simulate the effects of orthostatic stress (gravitational stress in the upright position). The new micro-circulation element allowed to improve the volume distribution without affecting the flow distribution and the arterial wave propagation.

Arterial pressure and flow waveforms (Figure 5.2 and 5.5) shows similar patterns compared to numerical studies only modeling the systemic arteries, i.e. increased pressure pulsatility and flow reversal towards the periphery (Kroon et al., 2012; Reymond et al., 2009). Venous wave propagation shows the typical biphasic pattern (Fung, 1997), but large pulsatility are observed while using the single windkessel model in comparison to the new three-compartment implementation. This can be explained by the characteristic venous impedance implemented in the three-compartment model to minimize high frequency reflections. The latter could be confirmed while analysing the forward and backward running waves (Parker, 2009). The general pressures and flows in the heart are in the physiological range (Boron and Boulpaep, 2003; Hall, 2010). Summarizing, the newly developed three-compartment model for the micro-circulation does not affect the arterial wave propagation, but does seem to minimize the reflections on the venous side of the system as expected.

The obtained pressure gradient (Figure 5.6 and 5.3) in the supine position shows for both micro-circulation implementations a decrease towards the periphery, which can be explained by the increasing contribution of friction. In tilted position both models follow the hydrostatic pressure gradient as expected. However, a large difference is observed in the pressure at the heart level in tilted position. In a healthy subject, the baroreflex maintains the systemic pressure. However, as the baroreflex is not included in the current model, a drop in pressure is expected in the tilted position as is observed using the new three-compartment implementation. On the other hand in the single windkessel, pressure at the heart level is hardly affected and, in contrast to what is known from experimental physiology, regulation does not seem to be necessary.

Where the flow distribution is not affected by the three-compartment implementation, the volume distribution changes significantly (Figure 5.4 and 5.7). Even when considering the large variation in volume distribution known from literature (Heldt et al., 2002; Lim et al., 2013), the new implementation (compliance based on the flow distribution) is closer to physiology than the single windkessel (compliance based on a typical time constant). Upon tilt hardly any change in flow and volume distribution is observed using the traditional windkessel model, whereas more physiological responses are observed with the three-compartment model: cerebral blood flow and

volume decrease and leg volume increases.

The large amount of volume present in the 0D representations of the models might suggest a total lumped model (i.e. also lumping the large systemic vessels) is more appropriate for studying the blood volume shift under head up tilt. However, physiological mechanisms reducing the gravity induced blood volume shift, such as venous valves and the muscle pump effect, ask for a 1D representation of the large vessels. Numerical studies of Marchandise and Flaud (2010) and Fullana and Zaleski (2008) present numerical models capturing the hemodynamics of the muscle pump effect. However, the included vascular network is restricted to the calf circulation, not allowing to investigate the influence of the muscle pump effect on the venous return. The current model enables to investigate the global effect of the muscle pump effect.

The splanchnic region is believed to contain up to $15 - 20\%$ of the total blood volume and has thereby potentially an important role in volume regulation. However, in the current implementation the splanchnic region shows only a small increase in volume upon tilt. Some studies hypothesize an active venoconstriction may make more blood volume available for the rest of the circulation (Rothe, 2006a,b). Another hypothesis states that arteriolar vasoconstriction (as induced upon tilt by the baroreflex) will result in a decreased pressure in the venules and thereby shift a large amount of blood volume out of the splanchnic circulation (Jarvis et al., 2010; Rowell, 1993). The current model has the potential to test these hypotheses once extended with baroreflex regulation and venoconstriction (Ursino, 1998).

The newly developed distributed windkessel model has the advantage it defines the compliance while accounting for the correct volume distribution. Furthermore, the division of the micro-circulation into an arteriolar, capillary and venular level allows the inclusion of level-specific mechanisms. For example, changes in vascular tone could now easily be included while only affecting the arteriolar part of the resistance, or the venular part in case of venoconstriction. Also, filtration, occurring during prolonged orthostatic stress, could be included only at the level of the capillaries.

5.5 Conclusion

A 1D pulse wave propagation model has been developed, which accounts for gravitational acceleration in the systemic circulation. Furthermore, a new micro-circulation element is included, which in contrast to the traditional single windkessel model, accounts for the volume distribution, without affecting the arterial pressure and flow wave propagation and the flow distribution over the body parts. Additionally, the distribution of the resistance and compliance over an arteriolar, capillary and venu-

lar part allows easy future inclusion of relevant physiological mechanisms, such as vasoconstriction and filtration. Finally, the observed pressure drop upon head up tilt endorses the need for inclusion of regulation mechanisms such as the muscle pump effect and venous valves.

Chapter 6

General discussion

6.1 Motivation, aim and methodology

The main function of the cardiovascular system is to transport oxygenated blood to the tissue and deoxygenated blood back to the heart and lungs. To supply the tissue with sufficient oxygen the cardiovascular system can regulate blood flow upon a change in oxygen demand or in response to external stress factors. Orthostatic stress, i.e. gravitational stress in the upright position, will induce a blood volume shift from the head towards the feet. This large blood volume shift stresses the cardiovascular system significantly, because it will increase transmural pressure in the lower extremity and increase oxidative stress in the cerebral tissue. In order to minimize the gravity-induced stresses, a complex system of protection mechanisms is activated. This includes amongst others (1) the presence of venous valves, ensuring unidirectional flow in the veins, (2) the calf muscle pump effect, squeezing the embedded veins upon muscle contraction and thereby increasing venous return, and (3) the baroreflex, aiming to maintain systemic arterial pressure by affecting heart rate, contractility and peripheral resistance. Although many experimental studies have tried to unravel the mechanisms behind the hemodynamic response to orthostatic stress, still many questions remain unanswered. Specifically, experimental studies provide many correlations, but often lack mechanistic insight.

In the past, mathematical models that are based on physical laws and physiological mechanisms have aided understanding of cardiovascular (patho-)physiology (Boileau et al., 2015; van de Vosse and Stergiopulos, 2011). Mathematical models can often provide much more detailed insight compared to experimental studies, due to the fact that the implemented physiological relations are clearly defined and the influence of individual model parameter variation and their interactions can easily be examined and quantified. Therefore, we believe that mathematical models can provide the missing mechanistic insight into the hemodynamic response to orthostatic stress.

In this PhD project, mathematical models have been developed that enable examination of three major mechanisms that minimize the blood volume shift in response to orthostatic stress, including: the muscle pump effect (Chapter 2), venous valve dynamics under tilt (Chapter 3), and the regulation of vascular tone in response to muscle contraction (Chapter 4). An approach is used in which the model is extended with physiological aspects step-by-step to reveal their individual contribution. Finally, in Chapter 5 a full circulation model is presented that allows inclusion of the total blood volume using a new micro-circulation element. The full circulation model serves as a backbone for future model development in which all phenomena are integrated. Such a model allows the examination of the global response to local phenomena and their mutual interactions.

In the subsequent part of the general discussion first the main scientific achievements are presented, followed by the limitations, future perspectives and concluding remarks.

6.2 Scientific achievements

6.2.1 Numerical contributions

First, an existing and validated 1D pulse wave propagation model (Kroon et al., 2012) able to simulate pressure and flow waveforms throughout the arterial system was adapted and extended so that it captures the dynamics of the calf muscle pump effect. This extension includes venous collapsibility, venous valves and gravity and thereby the model captures the following characteristics: (1) venous collapsibility was included by using a fit of the experimentally derived relation between venous cross-sectional area and transmural pressure (Shapiro, 1977). (2) Venous valves were included to ensure unidirectional flow in the veins. In contrast to the few studies that include venous valves (Fullana et al., 2003; Müller and Toro, 2014), this study also examined their opening state during the muscle pump effect. And (3) gravity was added to the momentum balance. Although most numerical studies neglect gravity to simplify the model (Boileau et al., 2015; van de Vosse and Stergiopulos, 2011), it is required here to account for the hydrostatic pressure arising upon tilt.

Second, a detailed study of a venous valve model was presented in Chapter 3. The versatile heart valve model of Mynard et al. (2012) was used to allow detailed study of valve dynamics, also providing potential for future study of pathologies such as valve regurgitation and valve prolapse. The inclusion of a continuous valve opening state is in strong contrast to previous studies, where the dynamics of the venous valves are often captured by a simple diode, which defines only the fully open and the fully closed state of the valve. A sensitivity analysis was performed to gain more insight into the relative importance of model parameters. From the sensitivity analysis it was concluded that *in vivo* ultrasound measurements of the venous radius can be used to reduce the model uncertainty. More detailed models (e.g. fluid structure interaction) could be used to inform the valve model on model parameters which are hard to assess *in vivo*, such as the pressure drop at which valve opening and closing is initiated.

Third, to capture the vasodilatory response to a muscle contraction, the calf circulation model presented in Chapter 2 was extended to include regulation of vascular tone based on the cerebral auto-regulation model of Spronck et al. (2012) and the baroreflex model of Ursino (1998). Although the individual models are not new, the combination is novel. After adapting the model parameters to the muscles of the

lower limb and tuning the myogenic and metabolic gain, the simulated arterial flow response was in good agreement with *in vivo* measurements. To validate the choice of the fitting parameters and to gain more insight in the influence of the model parameter variance on the variance in flow response, a global sensitivity analysis was performed. The sensitivity analysis did not give surprising results, but provided a quantification of the empirically expected importance of model parameters. Because a global approach was taken in the sensitivity analysis, the importance of the interactions between model parameters was also derived and these showed to be of significant importance. This implied the model complexity was not too large.

Fourth, in the final chapter a full circulation model was presented to assess blood volume shifts under head up tilt. Although many numerical studies focussing on orthostatic stress use 0D models of the full circulation (Heldt et al., 2002; Olufsen et al., 2005), we chose to include the systemic arteries and veins using a 1D pulse wave propagation model, because this also allows future implementation of venous valves and the muscle pump effect. Furthermore, gravity is included in the 1D pulse wave propagation model, which makes it, as far as we know, the first 1D full circulation model with gravity included. However, the most novel aspect is the inclusion of a newly developed micro-circulation model to take into account the total blood volume and its distribution over the circulation. This is in strong contrast to previously developed micro-circulation models used in combination with 1D pulse wave propagation model, because their parameters are tuned to obtain physiological pressure and flow waves, without considering the blood volume (Müller and Toro, 2014; Mynard and Smolich, 2015).

6.2.2 Physiological contributions

The analyses in Chapter 2 revealed that the venous valves significantly increased the efficiency of the muscle pump, because once valves were included the increase in venous return could not reflux to refill the vein during muscle relaxation. The step from the supine to the upright position again emphasized the importance of the venous valves. When upright muscle perfusion increased due to the shielding function of the venous valves. In a final step the superficial venous system was added to the geometry, which reduced the refilling time of the vein after muscle contraction. In contrast to experimental studies, the comparison of several model configurations allowed us to confirm the importance of venous valves and the superficial veins, as was hypothesized experimentally.

The arterial flow increase simulated in Chapter 2 was relatively small in comparison to *in vivo* measurements. This implied that the muscle pump effect was not the sole mechanism responsible for the flow increase. It was concluded that there was still

some physiological mechanism missing in the model and therefore the calf circulation model was extended with regulation of vascular tone, as presented in Chapter 4. The regulation model included myogenic, metabolic and baroreflex regulation. Based on the good agreement between simulated and *in vivo* arterial flow response, it was concluded that the presented model included all dominating physiological mechanisms influencing the hemodynamic response to a muscle contraction. From the activation pattern it was confirmed that the metabolic mechanism was the main vasodilator inducing the flow increase after muscle contraction. The change in baseline flow in the tilted position, was attributed to the activation of the baroreflex and the myogenic mechanism. Both conclusions were in line with hypotheses stated in experimental studies (Nådland et al., 2009). Additionally, the numerical step-by-step approach revealed the importance of individual regulation mechanisms and model parameters.

6.3 Limitations

Although the developed mathematical models have resulted in new physiological insight, some essential improvements and validation steps necessary to obtain a model that can describe the full hemodynamic response to orthostatic stress are described in the subsequent section.

To obtain a clear distinction between the contraction and relaxation phase of the muscle pump effect (Chapter 2), changes in muscular pressure were defined relatively slowly compared to what is observed *in vivo*. However, early numerical studies on collapsible tubes already demonstrated that capturing fast changes in hemodynamics involved with venous collapse, valve closure and large volume shifts can reduce the numerical stability of the mathematical model (Brook and Pedley, 2002; Brook et al., 1999). Although the current thesis focussed more on the physiological examination of the simulated hemodynamics, future research into the numerical stability of the developed models is needed to examine faster changes.

In the current study, the constitutive behaviour of the venous wall is included based on the tube law of Shapiro (1977). This non-linear cross-sectional area pressure relation includes collapse under negative transmural pressure, e.g. due to the influence of gravity (Chapter 3 and 5) or increasing extravascular pressure under muscle contraction (Chapter 2 and 4). The exact shape of the relation, and thereby the rate of collapse, depends on the bending stiffness K_p, which in the current implementation is related to the radius of the corresponding vessel. Early analytical studies suggest to derive the bending stiffness from the mechanical properties of the vessel wall such as the Young's modulus (Brook et al., 1999; Fung, 1997). This approach result in $\mathcal{O}(10^{-2})$. Later, the bending stiffness was suggested to be based on the expected

wave speed derived via the radius of the veins (Müller and Toro, 2014). This resulted in a significant increase in K_p $\mathcal{O}(10^2)$. However, both approaches do not consider the support of the surrounding tissue as demonstrated by Bassez et al. (2001) in *in vitro* measurements. Bassez et al. (2001) showed that an increase in stiffness of the surrounding tissue reduces the rate of collapse in the constitutive law. Preliminary *in vivo* results of Bassez et al. (2001) confirmed the relation of K_p and the support of the surrounding tissue, but a full validation is still missing. Summarizing, there is a strong need for *in vivo* studies to define the constitutive behaviour of the venous wall throughout the whole venous tree, as for example examined within the lower limb by Bassez et al. (2001) and Chauveau et al. (2006). An improved representation of the venous constitutive law is expected to increase the certainty of the volume shift observed under muscle contraction and head up tilt.

The versatile valve model examined in Chapter 3 can provide a strong tool to examine the valve dynamics in chronic venous disease. Although the presented sensitivity analysis showed the importance of accurately assessing the venous radius and the pressure drop over the valve on opening, a validation based on *in vivo* measurements is essential for future patient specific applications. This should include a validation of the valve dynamics, i.e. time course of valve opening and closing, as well as the hemodynamics, i.e. the varying pressure-flow relation depending on the valve state. For this, ultrasound measurements could be performed to track the flow and valve dynamics, and *in vivo* pressure could be obtained from a guided pressure-wire. However, as inserting sensors is invasive and might influence the dynamics, one could also consider to use 3D fluid structure interactions simulations for validation.

In Chapter 5 it was concluded that the traditional windkessel model was not capable of capturing the total blood volume and therefore a new micro-circulation model was presented. However, the preceding chapters included the micro-circulation based on the traditional windkessel model. Although it is not expected to change the general conclusions, the large compliance present close to the 1D veins could affect the hemodynamics under examination. For example the importance of the valve might increase even more, as leaking towards the tissue under muscle contraction would be facilitated due to increased compliance. However, further research is needed to confirm this.

6.4 Future perspectives

An obvious next step in modeling the hemodynamic response to orthostatic stress, is to combine the local models presented in the first three chapters with the full circulation model of Chapter 5. This would allow investigation of the impact of the

full hydrostatic column and blood pulsatility on the local mechanisms. This step would also allow investigation of the global effect of the local mechanisms, such as the influence of the muscle pump effect on venous return.

Additional model extensions which improve the simulated blood volume shift in response to orthostatic stress are the incorporation of the baroreflex and capillary filtration. Incorporation of the baroreflex (Olufsen et al., 2006; Ursino, 1998) induces an increase in heart rate, contractility and peripheral resistance to maintain systemic arterial pressure in the tilted position. Including the effect of capillary filtration would especially influence the orthostatic tolerance during prolonged orthostatic stress or while simulating higher gravitational loads as experienced during centrifuge.

Furthermore, the developed models could be used to validate hypotheses arising from experimental studies. An example could be the debate on the mechanisms of regulation of the splanchnic blood volume. Where some studies hypothesize that active venoconstriction is the main factor moving blood out of the splanchnic circulation (Rothe, 2006a,b), others believe that arteriolar vasoconstriction will reduce venular pressure and thereby induce a passive shift out of the splanchnic circulation (Jarvis et al., 2010; Rowell, 1993). After extending the full circulation model as presented in Chapter 5 with baroreflex regulation and venoconstriction, both hypothesis could be examined.

Apart from studying the hemodynamic response to orthostatic stress, the developed models could also be used in other applications, for example to study exercise. Once the developed models of the local calf circulation are included in the full circulation model, a series of muscle contractions alternating in the left and right leg could be used to simulate running. If trying to simulate heavy exercise, one might consider also including a model of the oxygen distribution (van der Hout-van der Jagt et al., 2012).

In contrast to the arterial system, the anatomy of the venous tree is highly variable and complex (Meissner, 2005). The developed mathematical models could be used to examine the influence of the variation in venous geometry and valve distribution on the hemodynamics. This is also of interest while examining chronic venous disease, where the hemodynamics are expected to be affected by valve regurgitation and valve prolapse.

6.5 Concluding remarks

Mathematical models are indispensable to increase the understanding of the cardiovascular physiology. This thesis reports an important step towards full understand-

ing of the hemodynamic response to orthostatic stress.

In the current thesis mathematical models have been developed to investigate three major mechanisms that minimize the gravity-induced blood volume shift due to orthostatic stress: the muscle pump effect, venous valves and regulation of vascular tone. A step-by-step approach has allowed to distinguish the importance of the various physiological aspects. The venous valves are concluded to be of significant importance for increasing venous return during muscle pump activation and shielding the hydrostatic pressure in tilted position. Furthermore, the superficial system reduces venous refilling time. Second, a global sensitivity analysis of the venous valve dynamics is performed to gain insight in the importance of the various model parameters and their interactions. From this, it is concluded that improved assessment of venous radius and pressure drop at valve opening can reduce model uncertainty. Third, upon inclusion of regulation of vascular tone, the model was able to fit the simulated arterial flow response after a muscle contraction to *in vivo* measurements. Due to the individual representation of the regulation mechanisms, the metabolic activation could be identified as the main vasodilator after muscle contraction. Furthermore, the baroreflex and myogenic responses were identified as the most important mechanisms for decreasing the baseline flow in tilted position.

In addition, a 1D full circulation model has been presented that accounts for the blood volume and its distribution. This full circulation model can serve as a backbone for future models in which all local models can be integrated. Such a model would allow examination of the global response to these local phenomena and their mutual interactions.

In summary, this thesis has demonstrated that reduced order models provide a strong tool to increase the understanding of the hemodynamic response to orthostatic stress. As discussed above, the developed models provide many opportunities to answer further research questions regarding the hemodynamic response to orthostatic stress.

References

M. M. Abu-Yousef, M. Mufid, K. T. Woods, B. P. Brown, and T. J. Barloon. Normal Lower Limb Venous Doppler Flow Phasicity: Is It Cardiac or Respiratory? *AJR Am J Roentgenol*, 169:1721–1725, 1997.

T. Arts, P. H. Bovendeerd, F. W. Prinzen, and R. S. Reneman. Relation between left ventricular cavity pressure and volume and systolic fiber stress and strain in the wall. *Biophys J*, 59(1):93–102, 1991.

S. Bassez, P. Flaud, and M. Chauveau. Modeling of the deformation of flexible tubes using a single law: Application to veins of the lower limb in man. *J Biomech Eng*, 123(1):58–65, 2001.

J. J. Bergan, G. W. Schmid-Schönbein, P. D. Coleredge Smith, A. N. Nicolaides, M. R. Boisseau, and B. Eklof. Chronic venous disease. *N Engl J Med*, 355(5):488–498, 2006.

D. Bessems, M. Rutten, and F. Van De Vosse. A wave propagation model of blood flow in large vessels using an approximate velocity profile function. *J Fluid Mech*, 580:145–168, 2007.

A. S. Bode, W. Huberts, E. M. H. Bosboom, W. Kroon, W. P. M. van der Linden, R. N. Planken, F. N. van de Vosse, and J. H. M. Tordoir. Patient-specific computational modeling of upper extremity arteriovenous fistula creation: its feasibility to support clinical decision-making. *PLoS one*, 7(4):e34491, 2012.

E. Boileau, P. Nithiarasu, P. J. Blanco, L. O. Mueller, F. E. Fossan, L. R. Hellevik, W. P. Donders, W. Huberts, M. Willemet, and J. Alastruey. A benchmark study of

numerical schemes for one-dimensional arterial blood flow modelling. *Int J Numer Method Biomed Eng*, 31(10):e02732, 2015.

W. F. Boron and E. L. Boulpaep. *Medical Physiology: Updated Edition*. Elsevier Health Sciences, 2003.

P. H. M. Bovendeerd, P. Borsje, T. Arts, and F. N. van De Vosse. Dependence of intramyocardial pressure and coronary flow on ventricular loading and contractility: a model study. *Ann Biomed Eng*, 34(12):1833–1845, 2006.

B. S. Brook and T. J. Pedley. A model for time-dependent flow in (giraffe jugular) veins: uniform tube properties. *J Biomech*, 35(1):95–107, 2002.

B. S. Brook, S. A. E. G. Falle, and T. J. Pedley. Numerical solutions for unsteady gravity-driven flows in collapsible tubes: evolution and roll-wave instability of a steady state. *J Fluid Mech*, 396(1999):223–256, 1999.

J. C. Buckey, L. D. Lane, B. D. Levine, S. J. Watenpaugh, S. J. Wright, W. E. Moore, F. A. Gaffney, and C. G. Blomqvist. Orthostatic intolerance after spaceflight. *J Appl Physiol*, 81:7–18, 1996.

G. C. Butler, H. Xing, D. R. Northey, and R. L. Hughson. Reduced orthostatic tolerance following 4 h head-down tilt. *Eur J Appl Physiol Occup Physiol*, 62:26–30, 1991.

C. Cancelli and J. Pedley. A separated-flow model for collapsible tube oscillations. *J Biomech*, 157:375–404, 1985.

A. Caroli, S. Manini, L. Antiga, K. Passera, B. Ene-Iordache, S. Rota, G. Remuzzi, A. Bode, J. Leermakers, F. N. van de Vosse, R. Vanholder, M. Malovrh, J. Tordoir, and A. Remuzzi. Validation of a patient-specific hemodynamic computational model for surgical planning of vascular access in hemodialysis patients. *Kidney Int*, 84(6):1237–1245, 2013.

M. Chauveau, S. Bassez, S. Tra, and B. Scherrer. Area-pressure relationship of lower limb main veins in man. *VASA*, 35(2):59–66, 2006.

G. B. Chavhan, D. A. Parra, A. Mann, and O. M. Navarro. Normal Doppler Spectral Waveforms of Major Pediatric Vessels: Specific Patterns. *RadioGraphics*, 28(3):691–706, 2008.

V. E. Claydon, J. D. Steeves, and A. Krassioukov. Orthostatic hypotension following spinal cord injury: understanding clinical pathophysiology. *Spinal Cord*, 44(6): 341–351, 2006.

G. Clément and A. Pavy-Le Traon. Centrifugation as a countermeasure during actual and simulated microgravity: a review. *Eur J Appl Physiol*, 92(3):235–248, 2004.

P. Coleridge-Smith, N. Labropoulos, H. Partsch, K. Myers, A. Nicolaides, and A. Cavezzi. Duplex Ultrasound Investigation of the Veins in Chronic Venous Disease of the Lower Limbs - UIP Consensus Document. Part I. Basic Principles. *Eur J Vasc Endovasc Surg*, 31:83–92, 2006.

L. G. E. Cox, S. Loerakker, M. C. M. Rutten, B. A. J. M. de Mol, and F. N. van de Vosse. A mathematical model to evaluate control strategies for mechanical circulatory support. *Artif Organs*, 33(8):593–603, 2009.

E. Criado, M. A. Farber, W. A. Marston, P. F. Daniel, C. B. Burnham, and B. A. Keagy. The role of air plethysmography in the diagnosis of chronic venous insufficiency. *J Vasc Surg*, 27(4):660–670, 1998.

R. S. S. Crisóstomo, M. S. Candeias, and P. A. S. Armada-da Siva. The use of ultrasound in the evaluation of the efficacy of calf muscle pump function in primary chronic venous disease. *Phlebology*, 29:247–256, 2014.

W. P. Donders, W. Huberts, F. N. van de Vosse, and T. Delhaas. Personalization of models with many model parameters: an efficient sensitivity analysis approach. *Int J Numer Method Biomed Eng*, 31(10):e02727, 2015.

R. T. Eberhardt and J. D. Raffetto. Chronic Venous Insufficiency. *Circulation*, 111: 2398–2409, 2005.

V. G. Eck, W. P. Donders, J. Sturdy, J. Feinberg, T. Delhaas, L. R. Hellevik, and W. Huberts. A guide to uncertainty quantification and sensitivity analysis for cardiovascular applications. *Int J Numer Method Biomed Eng*, 32(8):e02755, 2016.

M. A. Elliott, G. A. Walter, H. Gulish, A. S. Sadi, D. D. Lawson, W. Jaffe, E. K. Insko, J. S. Leigh, and K. Vandenborne. Volumetric measurement of human calf muscle from magnetic resonance imaging. *MAGMA*, 5(2):93–98, 1997.

C. J. Evans, F. G. R. Fowkes, C. V. Ruckley, and A. J. Lee. Prevalence of varicose veins and chronic venous insufficiency in men and women in the general population: Edinburgh Vein Study. *J Epidemiol Community Health*, 53(3):149–153, 1999.

J. E. Flaherty, J. B. Keller, and S. I. Rubinow. Post buckling behavior of elastic tubes and ring with opposite sides in contact. *J Appl Math*, 23(4):446–455, 1972.

R. H. Fox. *The venous system in health and disease*. IOS Press, 2001.

R. Freeman, V. Lirofonis, W. B. Farquhar, and M. Risk. Limb venous compliance in patients with idiopathic orthostatic intolerance and postural tachycardia. *J Appl Physiol*, 93(2):636–644, 2002.

R. Freeman, W. Wieling, F. B. Axelrod, D. G. Benditt, E. Benarroch, I. Biaggioni, W. P. Cheshire, T. Chelimsky, P. Cortelli, C. H. Gibbons, D. S. Goldstein, R. Hainsworth, M. J. Hilz, G. Jacob, H. Kaufmann, J. Jordan, L. A. Lipsitz, B. D. Levine, P. A. Low, C. Mathias, S. R. Raj, D. Robertson, P. Sandroni, I. Schatz, R. Schondorff, J. M. Stewart, and J. G. Van Dijk. Consensus statement on the definition of orthostatic hypotension, neurally mediated syncope and the postural tachycardia syndrome. *Clin Auton Res*, 21(2):69–72, 2011.

J. M. Fritsch, J. B. Charles, B. S. Bennett, M. M. Jones, and D. L. Eckberg. Short-duration spaceflight impairs human carotid baroreceptor-cardiac reflex responses. *J Appl Physiol*, 73(2):664–671, 1992.

J.-M. Fullana and S. Zaleski. A branched one-dimensional model of vessel networks. *J Fluid Mech*, 621:183–204, 2008.

J.-M. Fullana, F. Cros, P. Flaud, and S. Zaleski. Filling a collapsible tube. *J Fluid Mech*, 494:285–296, 2003.

Y. Fung. *Biomechanics: mechanical properties of living tissues*. Springer New York, 1993.

Y. Fung. *Biomechanics: circulation*. Springer, 1997.

C. Geers and G. Gros. Carbon dioxide transport and carbonic anhydrase in blood and muscle. *Physiol Rev*, 80(2):681–715, 2000.

S. Gelman. Venous Function and Central Venous Pressure - A physiologic story. *Anesthesiology*, 108(4):735–748, 2008.

S. D. Gray, C. Staub, D. Sarah, E. Carlsson, and N. C. Staub. Site of increased vascular resistance during isometric muscle contraction. *Am J Physiol*, 213(3):683–689, 1967.

J. E. Hall. *Guyton and Hall Textbook of Medical Physiology*. Elsevier Health Sciences, 2010.

T. Heldt, E. B. Shim, R. D. Kamm, and R. G. Mark. Computational modeling of cardiovascular response to orthostatic stress. *J Appl Physiol*, 92(3):1239–1254, 2002.

W. Huberts, W. P. Donders, T. Delhaas, and F. N. van de Vosse. Applicability of the polynomial chaos expansion method for personalization of a cardiovascular pulse wave propagation model. *Int J Numer Method Biomed Eng*, 30:1679–1704, 2014.

J. R. Hughes and J. Lubliner. On the One-Dimensional Theory of Blood Flow in the Larger Vessels. *Math Biosci*, 18:161–170, 1973.

L. Irving, H. C. Foster, and J. K. W. Ferguson. The carbon dioxide dissociation curve of living mammalian muscle. *J Biol Chem*, 95(1):95–113, 1932.

S. S. Jarvis, J. P. Florian, M. J. Curren, and J. A Pawelczyk. Sex differences in vasoconstrictor reserve during 70 deg head-up tilt. *Exp Physiol*, 95(1):184–193, 2010.

W. T. Jellema, B. P. M. Imholz, H. Oosting, K. H. Wesseling, and J. J. Van Lieshout. Estimation of beat-to-beat changes in stroke volume from arterial pressure: a comparison of two pressure wave analysis techniques during head-up tilt testing in young, healthy men. *Clin Auton Res*, 9:185–192, 1999.

M. J. Joyner and D. P. Casey. Regulation of increased blood flow (hyperemia) to muscles during exercise: a hierarchy of competing physiological needs. *Physiol Rev*, 95:549–601, 2015.

M. L. Katz, A. J. Comerota, and R. Kerr. Air plethysmography (APG): a new technique to evaluate patients with chronic venous insufficiency. *J Vasc Tech*, 15(1): 23–27, 1991.

T. Kenner. The measurement of blood density and its meaning. *Basic Res Cardiol*, 84 (2):111–124, 1989.

T. Korakianitis and Y. Shi. Numerical simulation of cardiovascular dynamics with healthy and diseased heart valves. *J Biomech*, 39(11):1964–1982, 2006.

E. Kresch and A. Noordergraaf. Cross-sectional shape of collapsible tubes. *Biophys J*, 12(3):274–294, 1972.

W. Kroon, W. Huberts, M. Bosboom, and F. van de Vosse. A numerical method of reduced complexity for simulating vascular hemodynamics using coupled 0D lumped and 1D wave propagation models. *Comput Math Methods Med*, 2012: 156094, 2012.

N. Labropoulos, J. Tiongson, L. Pryor, A. K. Tassiopoulos, S. S. Kang, M. A. Mansour, and W. H. Baker. Definition of venous reflux in lower-extremity veins. *J Vasc Surg*, 38:793–798, 2003.

M. H. Laughlin. Skeletal muscle blood flow capacity: role of muscle pump in exercise hyperemia. *Am J Physiol*, 253:H993–H1004, 1987.

C. Leguy, J. Keijsers, W. Huberts, A. Narracott, J. Rittweger, and F. van de Vosse. Including gravitational stress in a blood pressure wave propagation model for cardiovascular space physiology. In *Comp Math Biomed Eng Proc*, number December, pages 397–400, 2013.

C. A. D. Leguy, E. M. H. Bosboom, A. P. G. Hoeks, and F. N. van de Vosse. Model-based assessment of dynamic arterial blood volume flow from ultrasound measurements. *Med Biol Eng Comput*, 47:641–648, 2009.

C. A. D. Leguy, E. M. H. Bosboom, H. Gelderblom, A. P. G. Hoeks, and F. N. Van De Vosse. Estimation of distributed arterial mechanical properties using a wave propagation model in a reverse way. *Med Eng Phys*, 32(9):957–967, 2010.

R. L. Letcher, S. Chien, T. G. Pickering, J. E. Sealey, and J. H. Laragh. Direct relationship between blood pressure and blood viscosity in normal and hypertensive subjects: role of fibrinogen and concentration. *Am J Med*, 70(6):11951202, 1981.

E. Lim, G. S. H. Chan, So. Dokos, S. C. Ng, L. A. Latif, S. Vandenberghe, M. Karunanithi, and N. H. Lovell. A Cardiovascular Mathematical Model of Graded Head- Up Tilt. *PLoS One*, 8(10):e77357, 2013.

F. Lurie, R. L. Kistner, B. Eklof, and D. Kessler. Mechanism of venous valve closure and role of the valve in circulation: A new concept. *J Vasc Surg*, 38(5):955–961, 2003.

E. Marchandise and P. Flaud. Accurate modelling of unsteady flows in collapsible tubes. *Comput Methods Biomech Biomed Engin*, 13(2):279–290, 2010.

E. Marchandise, M. Willemet, and V. Lacroix. A numerical hemodynamic tool for predictive vascular surgery. *Med Eng Phys*, 31:131–144, 2009.

B. Maton, G. Thiney, and A. Ouche. Intramuscular pressure and surface EMG in voluntary ankle dorsal flexion: Influence of elastic compressive stockings. *J Electromyogr Kinesiol*, 16(3):291–302, 2006.

J. J. McCaughan, D. B. Walsh, L. P. Edgcomb, and H. E. Garrett. In vitro observations of greater saphenous vein valves during pulsatile and nonpulsatile flow and following lysis. *J Vasc Surg*, 1(2):356–361, 1984.

M. E. McClurken, I. Kececioglu, R. D. Kamm, and A. H. Shapiro. Steady supercritical flow in collapsible tubes. Part 2. Theoretical studies. *J Fluid Mech*, 109:391–415, 1981.

M. H. Meissner. Lower extremity venous anatomy. *Semin Intervent Radiol*, 22(3): 147–156, 2005.

F. M. Melchior, R. S. Srinivasan, and J. B. Charles. Mathematical modeling of human cardiovascular system for simulation of orthostatic response. *Am. J. Physiol. Hear. Circ. Physiol.*, 262(31):H1920–H1933, 1992.

G. L. Moneta, G. Bedford, K. Beach, and D. E. Strandness. Duplex ultrasound assessment of venous diameters, peak velocities, and flow patterns. *J Vasc Surg*, 8(3): 286–291, 1988.

L. O. Müller and E. F. Toro. A global multiscale mathematical model for the human circulation with emphasis on the venous system. *Int J Numer Method Biomed Eng*, 30(7):681–725, 2014.

J. P. Mynard and J. J. Smolich. One-Dimensional Haemodynamic Modeling and Wave Dynamics in the Entire Adult Circulation. *Ann Biomed Eng*, 43(6):1443–1460, 2015.

J. P. Mynard, M. R. Davidson, D. J. Penny, and J. J. Smolich. A simple, versatile valve model for use in lumped parameter and one-dimensional cardiovascular models. *Int J Numer Method Biomed Eng*, 28:626–641, 2012.

I. H. Nådland, L. Walløe, and K. Toska. Effect of the leg muscle pump on the rise in muscle perfusion during muscle work in humans. *Eur J Appl Physiol*, 105(6): 829–841, 2009.

A. J. Narracott, J. M. T. Keijsers, C. A. D. Leguy, W. Huberts, and F. N. van de Vosse. Fluid-structure interaction analysis of venous valve haemodynamics. In P Nithiarasu and E. Budyn, editors, *Comp Math Biomed Eng Proc*, pages 31–34, July 2015.

W. Nichols and M. F. O'Rourke. *McDonald's Blood Flow in Arteries: Theoretic, Experimental and Clinical Principles*. CRC Press, 1997.

A. N. Nicolaides and A. J. Zukowski. The value of dynamic venous pressure measurements. *World J Surg*, 10:919–924, 1986.

A.N. Nicolaides. Investigation of Chronic Venous Insufficiency A Consensus Statement. *Circulation*, 102:e126–e163, 2000.

C. Nordborg, K. Fredriksson, and B. B. Johansson. The Morphometry of Consecutive Segments in Cerebral Arteries of Normotensive and Spontaneously Hypertensive Rats. *Stroke*, 16(2):313–320, 1985.

M. S. Olufsen, A. Nadim, and L. A. Lipsitz. Dynamics of cerebral blood flow regulation explained using a lumped parameter model. *Am J Physiol Regul Integr Comput Physiol*, 282:R611–R622, 2002.

M. S. Olufsen, J. T. Ottesen, H. T. Tran, L. M. Ellwein, L. Lipsitz, and V. Novak. Blood pressure and blood flow variation during postural change from sitting to standing: model development and validation. *J Appl Physiol*, 99:1523–1537, 2005.

M. S. Olufsen, H. T. Tran, J. T. Ottesen, Research Experiences for Undergraduates Program, L. A. Lipsitz, and V. Novak. Modeling baroreflex regulation of heart rate during orthostatic stress. *Am J Physiol Regul Integr Comp Physiol*, 291:R1355–R1368, 2006.

S. Pant, C. Corsini, C. Baker, T. Y. Hsia, G. Pennati, and I. E. Vignon-Clementel. Data assimilation and modelling of patient-specific single-ventricle physiology with and without valve regurgitation. *J Biomech*, pages 1–12, 2015.

K. H. Parker. An introduction to wave intensity analysis. *Med Biol Eng Comput*, 47 (2):175–188, 2009.

T. J. Pedley. *The fluid mechanics of large blood vessels*. Cambridge University Press, 2008.

A. A. Pollack and E. H. Wood. Venous Pressure in the Saphenous Vein at the Ankle in Man during Exercise and Changes in Posture. *J Appl Physiol*, 1:649–662, 1949.

J. M. Porter, G. L. Moneta, and An International Consensus Committee on Chronic Venous Disease. Reporting standards in venous disease: An update. *J Vasc Surg*, 21(4):635–645, 1995.

S. Quicken, W. P. Donders, E. M. J. Disseldorp, K. Gashi, B. M. E. Mees, F. N. van de Vosse, R. G. P. Lopata, T. Delhaas, and W. Huberts. Application of an adaptive polynomial chaos expansion on computationally expensive three-dimensional cardiovascular models for uncertainty quantification and sensitivity analysis. *J Biomech Eng*, 2016.

M. L. Raghavan, D. A. Vorp, M. P. Federle, M. S. Makaroun, and M. W. Webster. Wall stress distribution on three-dimensionally reconstructed models of human abdominal aortic aneurysm. *J Vasc Surg*, 31(4):760–769, 2000.

S. Raju, A. B. Green, R. K. Fredericks, P. N. Neglen, H. C. Alexander, and K. Koenig. Tube Collapse and Valve Closure in Ambulatory Venous Pressure Regulation: Studies With a Mechanical Model. *J Endovasc Surg*, 5:42–51, 1998.

P. Reymond, F. Merenda, F. Perren, D. Rüfenacht, and N. Stergiopulos. Validation of a one-dimensional model of the systemic arterial tree. *Am J Physiol Heart Circ Physiol*, 297(1):H208–H222, 2009.

C. F. Rothe. Point:Counterpoint: Active venoconstriction is/is not important in maintaining or raising end-diastolic volume and stroke volume during exercise and orthostasis. *J Appl Physiol*, 101(5):1262–1266, 2006a.

C. F. Rothe. Last Word: Point:Counterpoint author responds to commentaries on "Active venoconstriction is/is not important in main- taining or raising end-diastolic volume and stroke volume during exercise and orthostasis". *J Appl Physiol*, 101:1270, 2006b.

L. B. Rowell. *Human Cardiovascular Control*. Oxford University Press, 1993.

G. H. Rutan, B. Hermanson, D. E. Bild, S. J. Kittner, F. Labaw, and G. S. Tell. Orthostatic Hypotension in Older Adults. *Hypertension*, 19:508–519, 1992.

A. Saltelli, M. Ratto, F. Campolong, J Cariboni, D Gatelli, M Saisana, and S. Tarantola. *Global Sensitivity Analysis. The Primer*. John Wiley & Sons, LtD, 2008.

B. Saltin, G. Radegran, M. D. Koskolou, and R. C. Roach. Skeletal muscle blood flow in humans and its regulation during exercise. *Acta Physiol Scand*, 162:421–436, 1998.

J. M. Scott, D. E. R. Warburton, D. Williams, S. Whelan, and A. Krassioukov. Challenges, concerns and common problems: physiological consequences of spinal cord injury and microgravity. *Spinal cord*, 49(1):4–16, 2011.

S. S. Segal, T. P. White, and J. A. Faulkner. Architecture, composition, and contractile properties of rat soleus muscle grafts. *Am J Physiol*, 250(19):C474–C479, 1986.

A. H. Shapiro. Steady flow in collapsible tubes. *J Biomech Eng*, 99(3):126–147, 1977.

M. K. Sharp, J. J. Batzel, and J.-P. Montani. Space physiology IV: mathematical modeling of the cardiovascular system in space exploration. *Eur J Appl Physiol*, 113(8): 1919–1937, 2013.

Y. Shi, P. Lawford, and R. Hose. Review of zero-D and 1-D models of blood flow in the cardiovascular system. *Biomed Eng Online*, 10:33, 2011.

S. Simakov, T. Gamilov, and Y. N. Soe. Computational study of blood flow in lower extremities under intense physical load. *Russ J Numer Anal M*, 28(5):485–503, 2013.

M. F. Snyder and V. C. Rideout. Computer simulation studies of the venous circulation. *IEEE Trans Biomed Eng*, 16(4):325–334, 1969.

F. Sotiropoulos, T. B. Le, and A. Gilmanov. Fluid Mechanics of Heart Valves and Their Replacements. *Annu Rev Fluid Mech*, 48(1):259–283, 2016.

B. Spronck, E. G. H. J. Martens, E. D. Gommer, and F. N. van de Vosse. A lumped parameter model of cerebral blood flow control combining cerebral autoregulation and neurovascular coupling. *Am J Physiol Heart Circ Physiol*, 303:H1143–H1153, 2012.

M. E. Tschakovsky and D. D. Sheriff. Immediate exercise hyperemia: contributions of the muscle pump vs. rapid vasodilation. *J Appl Physiol*, 97(2):739–747, 2004.

M. E. Tschakovsky, J. K. Shoemaker, and R. L. Hughson. Vasodilation and muscle pump contribution to immediate exercise hyperemia. *Am J Physiol*, 271(4):H1697–H1701, 1996.

M. E. Tschakovsky, A. M. Rogers, K. E. Pyke, N. R. Saunders, N. Glenn, S. J. Lee, T. Weissgerber, and E. M. Dwyer. Immediate exercise hyperemia in humans is contraction intensity dependent: evidence for rapid vasodilation. *J Appl Physiol*, 96(2):639–644, 2004.

M. Ursino. A mathematical study of human intracranial hydrodynamics part 1 - the cerebrospinal fluid pulse pressure. *Ann Biomed Eng*, 16(4):379–401, 1988.

M. Ursino. Interaction between carotid baroregulation and the pulsating heart: a mathematical model. *Am J Physiol*, 275(44):H1733–H1747, 1998.

M. Ursino and P. D. Giammarco. A Mathematical Model of the Relationship Between Cerebral Blood Volume and Intracraniai Pressure Changes: The Generation of Plateau Waves. *Ann Biomed Eng*, 19(1):15–42, 1991.

M. Ursino and C. A. Lodi. Interaction among auto-regulation, CO2 reactivity, and intracranial pressure: a mathematical model. *Am J Physiol*, 274(43):H1715–H1728, 1998.

M. Ursino and E. Magosso. Acute cardiovascular response to isocapnic hypoxia. I. A mathematical model. *Am J Physiol Heart Circ Physiol*, 279:H149–H165, 2000.

M. Ursino and E. Magosso. Role of short-term cardiovascular regulation in heart period variability: a modeling study. *Am J Physiol Heart Circ Physiol*, 284:H1479–H1493, 2003.

F. N. van de Vosse and N. Stergiopulos. Pulse Wave Propagation in the Arterial Tree. *Annual Review of Fluid Mechanics*, 43(1):467–499, 2011.

M. B. van der Hout-van der Jagt, S. G. Oei, and P. H. M. Bovendeerd. A mathematical model for simulation of early decelerations in the cardiotocogram during labor. *Med Eng Phys*, 34(5):579–589, 2012.

M. B. van der Hout-van der Jagt, S. G. Oei, and P. H. M. Bovendeerd. Simulation of reflex late decelerations in labor with a mathematical model. *Early Hum Dev*, 89: 7–19, 2013.

J. Werner, D. Böhringer, and M. Hexamer. Simulation and Prediction of Cardiotherapeutical Phenomena From a Pulsatile Model Coupled to the Guyton Circulatory Model. *IEEE Trans Biomed Eng*, 49(5):430–439, 2002.

J. Wesche. The time course and magnitude of blood flow changes in the human quadriceps muscles following isometric contraction. *J Physiol*, 377:445–462, 1986.

N. Westerhof and G. Elzinga. Normalized input impedance and arterial decay time over heart period are independent of animal size. *Am J Physiol*, 261(30):R126–R133, 1991.

N. Westerhof, F. Bosman, C. J. de Vries, and A. Noordergraaf. Analog studies of the human systemic arterial tree. *J Biomech*, 2:121–143, 1969.

D. Williams, A. Kuipers, C. Mukai, and R. Thirsk. Review Acclimation during space flight: effects on human physiology. *CMAJ*, 180(13):1317–1323, 2009.

D. F. Young and F. Y. Tsai. Flow characteristics in models of arterial stenosis - I. Steady flow. *J Biomech*, 6:395–410, 1973a.

D. F. Young and F. Y. Tsai. Flow characteristics in models of arterial stenosis - II. Unsteady flow. *J Biomech*, 6(1955):547–559, 1973b.

M. Zacek and E. Krause. Numerical simulation of the blood flow in the human cardiovascular system. *J Biomech*, 29(1):13–20, 1996.

C. Zervides, A. J. Narracott, P. V. Lawford, and D. R. Hose. The role of venous valves in pressure shielding. *Biomed Eng Online*, 7:8, 2008.

Appendix A

Extravascular pressure

The temporal course of the extra vascular pressure is defined by

$$k(t) = \begin{cases} 0 & \text{if} \quad t < T_0 \\ \frac{1}{2}\left(1 + \sin(\frac{\pi(t-T_0)}{T_r} - \frac{\pi}{2})\right) & \text{if} \quad T_0 < t < T_0 + T_r \\ 1 & \text{if} \quad T_0 + T_r < t < T_0 + T_r + T_c \\ \frac{1}{2}\left(1 + \sin(\frac{\pi(t-T_0-T_r-T_c)}{T_f} + \frac{\pi}{2})\right) & \text{if} \quad T_0 + T_r + T_c < t < T_0 + T_r + T_c + T_f \\ 0 & \text{if} \quad t > T_0 + T_r + T_c + T_f \end{cases} \tag{A.1}$$

where $T_0 = 1\ s$ is the starting time of the compression, $T_r = 1\ s$ and $T_f = 1\ s$ are the times for the extravascular pressure to rise and fall respectively and $T_c = 1\ s$ is the time for the extravascular pressure to remain constant. The spatial course of the extravascular pressure is defined by

$$m(z) = \begin{cases} 0 & \text{if} \quad z < l_0 \\ \frac{1}{2}\left(1 + \sin(\frac{\pi(z-l_0)}{l_r} - \frac{\pi}{2})\right) & \text{if} \quad l_0 < z < l_0 + l_r \\ 1 & \text{if} \quad l_0 + l_r < z < l_{\text{end}} - l_f \\ \frac{1}{2}\left(1 + \sin(\frac{\pi(z-l_{\text{end}})}{l_f} + \frac{\pi}{2})\right) & \text{if} \quad l_{\text{end}} - l_f < z < l_{\text{end}} \\ 0 & \text{if} \quad z > l_{\text{end}} \end{cases} \tag{A.2}$$

where $l_0 = 0.07\ m$ and $l_{\text{end}} = 0.27\ m$ are the coordinates below and above which no extravascular pressure is applied and $l_r = 0.10\ m$ and $l_f = 0.10\ m$ are the lengths

over which the extravascular pressure rises and falls. The z-coordinate is defined to be zero at the distal side of the vein and increases to $z = 0.34\,m$ at the proximal side.

Appendix B

Regulation model

The regulation of vascular tone is based on three regulation mechanisms: myogenic regulation, metabolic regulation and the baroreflex. The activation of the different mechanisms and how they result in a change in resistance and compliance is explained in detail in the following sections.

B.1 Laplace's law

The arteriolar wall tension T_{tot} is the parameter determining vascular tone and is related to the arteriolar radius r_a via the Laplace law Fung (1993).

$$T_{\text{tot}} = p_a r_a - p_{ex}(r_a + h_a), \tag{B.1}$$

where p_a is the arteriolar pressure and h_a is the arteriolar wall thickness. The total tension is divided into three components: $T_{\text{tot}} = T_e + T_v + T_m$, where T_e, T_v and T_m are the elastic, viscous and active smooth muscle tension respectively. The passive elastic tension is based on experimental studies and is defined by the exponential function Ursino and Giammarco (1991)

$$T_e = h_a \sigma_e = h_a \left(\sigma_{e,0} \left(e^{K_\sigma \cdot \frac{r_a - r_{a,0}}{r_{a,0}}} - 1 \right) - \sigma_c \right), \tag{B.2}$$

where $\sigma_{e,0}$ and K_σ are parameters defining the shape of the function, $r_{a,0}$ is the vessel radius in the unstressed condition and σ_c is the stress contribution of the collagen fibers. Furthermore, the arteriolar wall thickness h_a is defined by assuming no longitudinal stretch and conservation of mass:

$$h_a = \sqrt{r_a^2 + 2r_{a,0}h_{a,0} + h_{a,0}^2} - r_a, \tag{B.3}$$

where $h_{a,0}$ is the unstressed arteriolar wall thickness.

The second component of the passive tension is the viscous tension T_v, which is in accordance with the viscous component of the Voigt model Ursino and Giammarco (1991)

$$T_v = \sigma_v h_a = \frac{\eta_a}{r_{a,0}} \frac{dr_a}{dt} h_a, \tag{B.4}$$

where η_a is the arteriolar wall viscosity.

The active smooth muscle tension T_m is known to decrease for very small and very large arteriolar radius and is therefore based on the following bell-type curve Ursino and Giammarco (1991)

$$T_m = T_{\text{max}} \cdot e^{-\left|\frac{r_a - r_m}{r_t - r_m}\right|^{n_m}}, \tag{B.5}$$

where r_m is the radius at which the smooth muscle cell exerts maximal tension, and r_t and n_m are constants. Furthermore, the maximal active tension T_{max} is defined by

$$T_{\text{max}} = T_{\text{max,0}}(1 + M_s), \tag{B.6}$$

where $T_{\text{max,0}}$ is the maximal tension at baseline, i.e. when the regulatory state M_s is equal to zero. The latter is defined by the following relation

$$M_s = \frac{e^{2M_{s,1}} - 1}{e^{2M_{s,1}} + 1}, \tag{B.7}$$

where

$$M_{s,1} = G_{\text{myo}} x_{\text{myo}} + G_{\text{meta}} x_{\text{meta}} + x_{\text{baro}} + x_{\text{init}}, \tag{B.8}$$

where x_i and G_i are the state and gain of the regulation mechanism i and x_{init} is the regulatory state at baseline. The state equations for x_i are described later on. Summarizing, the Laplace law is used to translate a change in regulatory state to a change in arteriolar radius. Actual changes in resistance and compliance of the micro-circulation are derived by coupling the arteriolar radius r_a to the arteriolar resistance R_a and volume C_a via

$$R_a = \frac{K_{a,R}}{r_a^4} \tag{B.9}$$

and

$$C_a = \frac{K_{a,C} r_a^2}{p_a}, \tag{B.10}$$

where

- $K_{a,R}$ is chosen such that the baseline arteriolar radius r_a and pressure p_a result in baseline flow q_a. Where baseline means the supine position and $M_{s,1} = x_{\text{init}}$.
- $K_{a,C}$ is chosen such that it corresponds with a total RC-time of 2.0 $[s]$ under baseline conditions.

Summarizing, the arteriolar resistance and compliance are regulated based on the arteriolar radius r_a. The latter is derived from the arteriolar wall tension based on the Laplace law. The muscular tension T_m is the part of the tension affected by the state of the regulation mechanisms x_i. In the following sections the state equations for the three regulation mechanisms are explained.

B.2 Myogenic regulation mechanism

Myogenic regulation protects the micro-vasculature against high pressures by increasing vascular tone upon increasing circumferential stresses and strains. Myogenic activation A_{myo} is therefore based on the current arteriolar tension T_{tot} Spronck et al. (2012)

$$A_{\text{myo}} = \frac{T_{\text{tot}} - T_{\text{myo,0}}}{T_{\text{myo,s}}}, \tag{B.11}$$

where $T_{\text{myo,0}}$ is the tension at baseline pressure for $M_{s,1} = x_{\text{init}}$ and $T_{\text{myo,s}} = 0.2T_{\text{max,0}}$ is a normalization tension. The myogenic regulation state x_{myo} is defined by

$$\frac{dx_{\text{myo}}}{dt} = \frac{A_{\text{myo}} - x_{\text{myo}}}{\tau_{\text{myo}}}, \tag{B.12}$$

where τ_{myo} is the myogenic time constant.

B.3 Metabolic regulation mechanism

Metabolic regulation can be initiated via different metabolites, such as potassium ions, adenosine, lactate and CO_2. These metabolites are generated during a muscle contraction and are washed out by the blood flow. In the current model CO_2 is chosen to be the determining metabolite for the regulation of blood flow during muscle contraction. First, the tissue CO_2-concentration C_{t,CO_2} is defined as the balance between metabolic rate and muscle perfusion q_d

$$\frac{dC_{t,CO_2}}{dt} = \frac{1}{V}\left(M_{CO_2} - q_d\left(C_{v,CO_2} - C_{a,CO_2}\right)\right), \tag{B.13}$$

where V is an estimate of the perfused muscle tissue volume, C_{v,CO_2} and C_{a,CO_2} are the venous and arterial CO_2-concentration respectively, of which the latter is fixed Spronck et al. (2012). The metabolic rate M_{CO_2} is related to muscle activity as follows:

$$M_{CO_2} = M_{CO_2,0}\left(1 + A_{\text{mc}}\left(f_m - 1\right)\right), \tag{B.14}$$

where f_m is the ratio of metabolic rate at rest and maximal activity and A_{mc} is muscle activity, which is defined to follow the contraction pattern (see Section 4.2.1 for the full definition). Furthermore, $M_{CO_2,0}$ is the basal metabolic production of CO_2 by a tissue of volume V

$$M_{CO_2,0} = M_{CO_2,0,m}\rho_m V, \tag{B.15}$$

where ρ_m is the muscle density and $M_{CO_2,0,m}$ is the basal metabolic CO_2-production per kg tissue. Muscle perfusion q_d in Equation (B.13) is the flow leaving the tissue, which is calculated using

$$q_d = \frac{p_2 - p_3}{R_a/2}, \tag{B.16}$$

where p_2 and p_3 are the pressure at node n_2 and n_3 respectively (Figure 5.1). Furthermore, C_{v,CO_2} is the venous CO_2-concentration and is determined by the following relation (Irving et al., 1932)

$$C_{v,CO_2} = \alpha_{t,v} C_{t,CO_2} + \beta_{t,v}, \tag{B.17}$$

where $\alpha_{t,v}$ and $\beta_{t,v}$ are fitting constants. The metabolic activation A_{meta} is determined by the CO_2-concentration in the tissue using

$$A_{\text{meta}} = \frac{C_{\text{t,CO}_2} - C_{\text{t,CO}_2,0}}{C_{\text{t,CO}_2,\text{s}}}, \tag{B.18}$$

where $C_{\text{t,CO}_2,0}$ is the steady state solution of Equation (B.13) and $C_{\text{t,CO}_2,\text{s}} = C_{\text{v,CO}_2,0} - C_{\text{a,CO}_2}$ is a scaling term. Finally, the metabolic regulation state x_{meta} is defined by

$$\frac{dx_{\text{meta}}}{dt} = \frac{A_{\text{meta}} - x_{\text{meta}}}{\tau_{\text{meta}}}, \tag{B.19}$$

where τ_{meta} is the time constant governing metabolic regulation.

B.4 Baroreflex regulation

The baroreflex is a global regulation mechanism which aims to maintain systemic pressure by affecting the heart rate, heart contractility, venous unstressed volume and peripheral resistance. In this study, only the effect of the baroreflex on the peripheral resistance is included, which is based on the model of Ursino (1998) (also implemented in other studies (Lim et al., 2013; van der Hout-van der Jagt et al.,

2013)). The carotid pressure p_{carotid} is used as an input parameter and is defined as mean systemic pressure (see Section 4.2.3 for details) plus a hydrostatic column of 20 cm in tilted position. First, carotid pressure is compared to a reference pressure p_{n}, which is defined as the baseline pressure in the supine position

$$\Delta p_{\text{baro}} = p_{\text{carotid}} - p_{\text{n}}. \tag{B.20}$$

This pressure difference Δp_{baro} is converted to an afferent baroreflex firing f_{ab} rate via a sigmoidal transfer function

$$f_{\text{ab}} = \frac{f_{\text{ab,min}} + f_{\text{ab,max}} \cdot e^{\left(\frac{\Delta p_{\text{baro}}}{k_{\text{dp}}}\right)}}{1 + e^{\left(\frac{\Delta p_{\text{baro}}}{k_{dp}}\right)}}, \tag{B.21}$$

where $f_{\text{ab,min}}$ and $f_{\text{ab,max}}$ are the firing rates reached for minimal and maximal Δp_{baro} and k_{dp} is a constant determining the slope of the afferent firing rate. The firing rate for the sympathetic innervation of the peripheral micro-circulation f_{sp} is calculated via the following relation:

$$f_{\text{sp}} = \begin{cases} f_{\text{sp},\infty} + \left(f_{\text{sp},0} - f_{\text{sp},\infty}\right) \cdot e^{-k_{\text{es}}\, f_{\text{ab}}} & \text{for } f_{\text{sp}} < f_{\text{sp,max}} \\ f_{\text{sp,max}} & \text{for } f_{\text{sp}} \geq f_{\text{sp,max}} \end{cases}, \tag{B.22}$$

where k_{es} is a parameter defining the shape of the sympathetic firing rate. The parameters $f_{\text{sp},0}$ and $f_{\text{sp},\infty}$ are the firing rates at zero and infinite afferent firing rate, and $f_{\text{sp,max}}$ is the maximal sympathetic firing rate. The sympathetic innervation is converted to an unfiltered change in resistance ΔR^*

$$\Delta R^* = \begin{cases} G_{\text{R}} \cdot \ln\left(f_{\text{sp}}(t - D_R) - f_{\text{sp,min}} + 1\right) & \text{for } f_{\text{sp}} \geq f_{\text{sp,min}} \\ 0 & \text{for } f_{\text{sp}} < f_{\text{sp,min}} \end{cases}, \tag{B.23}$$

where G_{R} is a constant gain, D_R is a pure time delay and $f_{\text{sp,min}}$ is the minimal sympathetic firing rate affecting the resistance. The actual change in resistance ΔR is calculated based on ΔR^* using a low pass filter

$$\frac{d\Delta R}{dt} = \frac{1}{\tau_R} \cdot \left(\Delta R^* - \Delta R\right), \tag{B.24}$$

where τ_R is the time constant of the low pass filter. Finally, the relative change in resistance c_{baro} is calculated using the following relation

$$c_{\text{baro}} = \frac{\Delta R - R_{\text{ref}}}{R_{\text{ref,Ursino}}} + 1 = \frac{R_{\text{baro}}}{R_{\text{ref}}}, \tag{B.25}$$

where R_{ref} is the resistance in baseline conditions in supine position and $R_{\text{ref,Ursino}}$ is the baseline resistance in the model of Ursino (1998). To combine the baroreflex

with the local auto-regulation mechanisms, the resistance is converted into a regulation state x_{baro} similar to the regulation state of the other mechanisms. Firstly, the resistance is converted to arteriolar radius using Equation (B.9)

$$a_{\text{baro}} = \left(\frac{K_R}{R_{\text{baro}}} \right)^{1/4}. \tag{B.26}$$

Using Laplace's law (Equation (B.1)) the arteriolar radius is converted into a change in muscular tension due to the baroreflex

$$T_{\text{m,baro}} = p_{\text{a}} a_{\text{baro}} - T_{\text{e,baro}} - T_{\text{v,baro}}, \tag{B.27}$$

where $T_{\text{e,baro}}$ and $T_{\text{v,baro}}$ are calculated using $r_a = a_{\text{baro}}$ (Equation (B.2) and (B.4) respectively). From the muscular tension the total regulation state $M_{\text{s,baro}}$ is derived using Equation (B.5) and (B.6)

$$M_{\text{s,baro}} = \frac{T_{\text{m,baro}}}{T_{\text{max,0}} \cdot e^{-\left(\frac{a_{\text{baro}} - a_{\text{m}}}{a_{\text{t}} - a_{\text{m}}} \right)^n}} - 1. \tag{B.28}$$

Finally, the total regulation state is converted to the regulation state via Equation (B.7) and (B.8)

$$x_{\text{baro}} = M_{\text{s,1,baro}} - x_{\text{init}} = \tanh^{-1}\left(M_{\text{s,baro}}\right) - x_{\text{init}} = \frac{1}{2} \ln \left(\frac{1 + M_{\text{s,baro}}}{1 - M_{\text{s,baro}}} \right) - x_{\text{init}}. \tag{B.29}$$